An application of quantum metrology: enhanced correlated interferometry

Doctoral Dissertation

Doctoral Program in Metrology (31^{st} Cycle),

An Application of Quantum Metrology: Enhanced Correlated Interferometry

A thesis submitted in partial fulfilment of the requirements for the degree of Doctor of Philosophy
by

Siva Pradyumna Tekuru

Politecnico di Torino, Italy
under supervision of

Professor Marco Genovese

Doctoral Examination Committee:
Professor Matteo Paris, University of Milano
Professor Paolo Olivero, University of Torino
Professor Lorenzo Maccone, University of Pavia
Professor Francesco Raffa, Politecnico di Torino
Dr. Paola Tiberto, Primo Ricercatore, INRIM

I hereby declare that, the contents and organisation of this dissertation constitute my own original work and does not compromise in any way the rights of third parties, including those relating to the security of personal data.

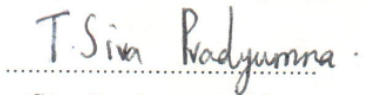

Siva Pradyumna Tekuru

ABSTRACT

Quantum metrology is a research field that deals with enhancing the resolution or sensing capabilities of a system which is otherwise constrained by classical limits. Improvements in measurements have historically led to new scientific discoveries, the recent example being the gravitational wave detection. Thus, quantum metrology could be an avenue for enabling scientific breakthroughs. In the present thesis, I have reported a first feasibility test of quantum enhanced correlated phase interferometry. A result that, on one other hand, paves the way for developing a new field of quantum metrology and on the other hand, could be applied to the detection of fundamental stochastic noises such as Holographic noise, gravitational wave background or traces of primordial black holes. The experiment was performed injecting two types of quantum states, namely the squeezed states and a twin-beam like state, in a system consisting of two co-located power recycled Michelson interferometers. When two independent squeezed states were injected, we were able in detecting a faint test correlated phase signal with an amplitude several orders of magnitude below the shot noise limited sensitivity of a single interferometer. The joint sensitivity obtained for the double interferometric system with squeezed states injected was $(3.21 \pm 0.16) \times 10^{-17} \frac{m}{\sqrt{Hz}}$ around 13.5 MHz, in a few seconds of measurement time. The second phase of the experiment involved the injection of a bipartite quantum correlated state in the two interferometers. In this case, we have demonstrated a quantum advantage in detecting uncorrelated noise or difference in the two interferometers' signals enabled by the reduction of the noise in the output photo-current subtraction.

PREFACE

The technological exploitation of quantum mechanics' principles can offer an improved performance over the classical framework[1][2]. Some of the principles on which these quantum technologies are built include uncertainty principle, superposition, entanglement etc. These quantum technologies are the foundation of the so called "second quantum revolution"[1][2]. If the first quantum revolution enabled inventions such as the laser and semiconductor and transistor, which behaviour has been understood through quantum mechanics, the use of the aforementioned non trivial quantum mechanical effects often involving the control and manipulation the single particle degree of freedoms is the main feature of the second quantum revolution. Among these technologies, one can mention quantum communication[3][4], quantum metrology[5][6][7], quantum computation[8][9] and quantum imaging [10][11]. Quantum metrology provides a route to overcome the classical limits in resolution or sensitivity of measurements, by exploiting the properties of quantum states [12],[6]. One of the examples, is the use of squeezed states of light, where fluctuations in one quadrature are suppressed at the expense of the other. The applications of squeezed states in metrology vary from gravitational wave detectors[13], magnetometry[14] and application to imaging of biological systems [5][15]. Another prominent example is exploiting entangled states, where the correlation level among particles exceeds the one allowed by classical physics. In general, there are wide range of applications of entanglement, such as spectroscopy[16], lithography[17], interferometry[18]. In particular, a special role in quantum metrology is played by non-classically correlated beam pairs, namely twin beam states which can produce maximally entangled states in photon number. Indeed, this kind of state in principle could be generated by interfering two squeezed states on a beam splitter. The recent demonstration of enhancement in sensitivity using two mode squeezing for detection of uncorrelated noises in a single interferometer is one of the example[19] for its application for quantum metrology.

Optical interferometry, represents one of the best sensing tool for detection of faint phase noises. A prime example is the recent detection of gravitational waves[20]. The large scale gravitational wave detectors employ a power recycled Michelson interferometer scheme with its arms having linear Fabry-Pérot cavities with a length around 4km. The typical strain sensitivity reported of the large scale gravitational wave interferometers are

$10^{-22}\sqrt{Hz^{-1}}$ around 150Hz frequency [20]. Since, the interferometer sensitivities are constrained by the shot noise one could increase the power in order to enhance the sensitivity. However, further increasing of power would lead to increase of radiation pressure noise from the mirrors, thermal effects, scattering etc. Hence, there is an interest for application of quantum technology in the interferometric systems to further enhance the sensing capabilities that could help unveil fundamental properties of nature. In particular, the use of squeezed light in large scale interferometers for detection of gravitational waves has already been implemented in LIGO and GEO600[13][21] where they have reported around 2.15dB and 2dB of quantum enhancement respectively.

There are fundamental sources of noises such as holographic noise[22] or gravitational wave background [23][24] that could produce correlated phase fluctuations in two separated interferometers, which have an increased chance to be detected by exploiting quantum enhanced interferometry with respect to other sources of noises. In particular, holographic noise would arise due to non-commutative property of the fundamental geometrical variables conjectured in some Planck scale phenomenological models, which are associated with uncertainty in measuring relative positions or rotation [25][13]. It has been argued that light, meanwhile propagating in the arms of an interferometer, would sum up incremental displacement at each discrete Planck interval step, leading to a measurable effect. Long-range (space-like) quantum-like correlation among these variables, and the consequent reduction of the effective numbers of independent degrees of freedom, would allow also to account for the holographic principle. The range of this correlation is expected to be only bounded by causality, namely the two interferometers should occupy the same space time volume. This noise is expected to be present in the frequencies upto MHz range.

For this purpose, a double interferometer system namely *Holometer*, consisting of pair of 40m long power recycled Michelson interferometers placed close to each other (without arm cavities), has been built at the Fermilab [26],[27]. However, at this moment, the holometer is being operated using classical light only. The results of the first measurements were reported in [27] where they have reported a strain sensitivity of $10^{-21}\sqrt{Hz^{-1}}$.

The present thesis discusses a first proof-of-principle experiment for demonstrating the possibility of overcoming the classical limits in correlated phase detection sensitivity by exploiting the properties of quantum states of light in this double interferometric system. This has been motivated by the results of earlier theoretical works [28][29]. In the present experiment, each interferometer was operated in a power recycling Michelson configuration without the arm cavities, thus emulating the configuration of Fermilab Holometer. The experiment was performed with two types of quantum states injected: a) Two independent squeezed light states injected into each interferometer b) Twin beam like state which is similar in properties to the two mode squeezing, where correlation in one of the quadrature is used.

The future outlook of this experiment is two fold. Firstly to use the quantum light in the present large scale interferometers at the Fermilab Holometer to enhance the sen-

sitivity for detection of possible planck scale effects. Secondly to compact the large scale double Michelson interferometers on a table-top setup and inject the quantum light into them.

Initially, the experiment was started at INRIM, where I had set up the interferometers and characterized them in the classical regime. In a second part, when squeezed light injection was required, the experiment was moved at the Danmarks Tekniske Universitet (DTU) in Lyngby, under the collaboration with the QPIT group. They provided the squeezed light sources for the experiment and support for concluding the experiment. During my PhD, I spent in Denmark for 18 months working on the experiment.

Structure of Thesis

The thesis consists in six chapters, each of them provided with an introduction, a main development, and conclusions. In the first chapter, I give an overview of some types of quantum states and their properties, and I discuss in depth, the theoretical framework for the correlated phase interferometery and its applications. In the second Chapter, I describe the properties of Fabry-Pérot and Michelson interferometers, and locking techniques used for stabilizing them. On the basis of the fundamental principles of these two kind of interferometers, then I discuss the properties of a power recycled Michelson interferometer which embeds the two technologies.

In the third chapter, I provide a detail description of experimental setup of the double interferometer and the squeezed light sources. The experimental characterization of the system is also presented in this chapter. In the fourth chapter, I deal with the shot noise calibration and measurements discussing the techniques used to evaluate the sensitivity. In the fifth chapter I present the results of enhancement in correlated phase detection sensitivity, when two independent squeezed states are injected. In the sixth chapter, I present the results of sub-shot noise reduction in the subtraction of photocurrents, when each mode of twin beam like state is injected in each interferometer.

In the Appendix electronic schemes for the PI controllers and photodetectors are presented. The methodology using Transfer function measurements and open loop measurements to optimize the interferometer system with design of appropriate PI controllers have been discussed.

ACKNOWLEDGEMENTS

Firstly, I would like to thank my parents, starting with my dad, who always created scientific temper by investing his time and energy in teaching science with practical approaches. To my mom, who is an Assistant Professor in chemistry, used to help me in other subjects, also encouraged me to pursue my passions without holding back. They both had a dream of getting their doctoral degrees, but for known reasons to me could not happen. Hence I dedicate this thesis to them.

To my advisor Marco Genovese, who is truly perfect supervisor. He has helped me a lot during this 3 years of my PhD which I cannot express in few words. I would be ever grateful to him for giving me an opportunity to work under his guidance. I would like to thank especially Ivano and Paolo, were the main people those who helped me during this 3 years of my PhD, from bureaucratic works to lab work and even correcting my thesis. The discussions and brainstorming sessions about the project with these people helped me learn a lot about this project. With sharing their expertise, I have just about learnt many valuable techniques in the lab required for this project. I would also like to thank Massimo Zucco where I have worked in his lab during my 1st year of my PhD. I would like to thank him for his guidance and sharing his expertise in setting up the interferometers.

Since I spent 18 months of time at Danmarks Tekniske Universitet (DTU),Lyngby, I would also like to thank Dr.Ulrik Andersen for hosting me and providing me guidance. I would also like to especially thank Tobias and Christian, were the main people who helped me during my stay at DTU. The valuable discussions with Tobias especially helped me learn things on my own, from setting up the experiment to understanding electronics and how cool is to work with quantum light.

I would also like thank Elena, who was my co-PhD student, also helped me in completing the experiment during my stay at DTU. I would also like to thank other researchers and colleagues such as Ivo Pietro Degiovanni, Marco Gramegna, Fabio Saacomandi, and others whoever I have interacted and whoever helped me with the bureaucratic works and wherever translation was required. Finally, I would like to thank the referees Prof. Paolo Olivero and Prof. Matteo Paris for giving their valuable comments on the thesis.

LIST OF SYMBOLS AND ACRONYMS

$D(\alpha)$	Displacement operator
$S(\xi)$	Squeezing operator
$S_{ab}(\xi)$	Two mode squeezing operator
$\mathscr{F}$	Fisher information
c	Speed of light
h	Planck constant
λ	Wavelength of the light
P_{BS}	Power at the Beam splitter
R_{PRM}	Reflectivity of the power recycling mirror
F	Finesse of the cavity
R_{BS}	Reflectivity at the beam splitter
G	Power Recycling Gain
V	Visibility of the interferometer
ΔX_{offset}	DARM Position of the fringe
ΔX_{rms}	Strain caused by the EOM
r_1,r_2	squeezing factors
ΔX	Displacement Sensitivity
ϵ	Contrast defect
η	Transmission efficiency
V_π	Half wave voltage of the EOM

r_{13} Electro optical coefficient

X_{jSN} Time series of the Shot noise of the j^{th} interferometer

X_{jWN} Time series of the white noise of the j^{th} interferometer

X_{jSQ} Time series of the Squeezed noise of the j^{th} interferometer

X_{jPN} Time series of the Photon noise of the j^{th} interferometer

$\rho_{12}(\tau)$ Normalized cross correlation coefficient

$R_{12}(\tau)$ Cross correlation function

$R_{xx}(\tau)$ Auto Correlation function

var Variance of a quantity

Cov Covariance of a quantity

PSD Power Spectral Density

CPSD Cross Power Spectral Density

DARM Differential Arm length

CARM Common Arm length

PI controller Proportionality Integral controller

AC output 100kHz High Passed power

DC power optical power measured at low frequencies

TWB state Twin beam state

SNL Shot Noise level

CONTENTS

CHAPTER 1

INTRODUCTION TO QUANTUM STATES OF LIGHT AND QUANTUM METROLOGY

1.1 Introduction

Quantum metrology is a field of study aiming at using quantum technologies to overcome the classical approaches in making highly sensitive measurements of physical parameters[12][6]. In general, when N classical probes are used to probe a system for estimation of an unknown parameter, the precision is limited by a scaling given by $1/\sqrt{N}$ known as the shot-noise limit. This scaling arises from the central limit theorem of statistics [7]. Consider for example an optical interferometer, where interference of photons at the output port carries information on the relative optical path difference between the interferometer arms, when a standard laser is used, the uncertainty in phase estimation is bound by the limit $1/\sqrt{N}$ where N is the number of photons used in the interferometer. To beat this shot noise limit, we need to exploit the properties of quantum light. In this chapter, some types of quantum states and advantages of using them in optical interferometers are described. I will then, more specifically introduce the experimental scheme of a double interferometer system with quantum light injected, since it has been my thesis work. The applications of this scheme would also be discussed.

1.2 Quantization of Electromaganetic Field

Let us consider a plane electromagnetic wave of frequency ω_k that is propagating in direction $\vec{k}$. The electric field and magnetic field are given by [30]

$$\vec{E}(\vec{r},t) = \vec{e}E_0 e^{(i\vec{k}\cdot\vec{r}-i\omega_k t)} + c.c \tag{1.2.0.1}$$

$$\vec{B}(\vec{r},t) = \frac{(\vec{k}\times\vec{e})}{k}E_0 e^{(i\vec{k}\cdot\vec{r}-i\omega_k t)} + c.c \tag{1.2.0.2}$$

where $c.c$ represents the complex conjugate and $\vec{e}$ denotes the polarization vector of the electromagnetic field and $k = |\vec{k}| = \frac{2\pi}{\lambda}$.

For convenience we work with vector potential $\vec{A}(\vec{r},t)$ and in a non relativistic domain. We adopt the Coulomb gauge and other Maxwell equations, where

$$\boldsymbol{\nabla} \cdot \vec{A}(\vec{r},t) = 0 \tag{1.2.0.3}$$

$$\vec{E} = -\frac{\partial A}{\partial t},\ \vec{B} = \nabla \times \vec{A} \tag{1.2.0.4}$$

In the case of plane wave we can write,

$$\vec{A}(\vec{r},t) = \epsilon A_0 e^{(i\vec{k}\cdot\vec{r}-i\omega_k t)} + c.c \tag{1.2.0.5}$$

where $A_0 = -\frac{ic}{\omega_k}E_0$

We would consider that this electromagnetic field is confined in box of volume V with length of each dimension L. We impose a periodic boundary conditions allowing the values of $\vec{k}$ as

$$\vec{k} = \frac{2\pi\vec{n}}{L} \text{ where } \vec{n} = (n_x, n_y, n_z) = 0, \pm1, \pm2, \pm3, ... \tag{1.2.0.6}$$

Here n is an integer with all possible values. Thus we can write the vector potential as

$$\vec{A}(\vec{r},t) = \frac{1}{2}\sum_k \sum_s (A_{ks} e^{i\vec{k}\cdot\vec{r}-i\omega_k t}\vec{e}_{ks} + c.c.) \tag{1.2.0.7}$$

where s is the basis of polarization which takes values 1,2. We can then derive E and B using equation (1.2.0.4) and we get,

$$\vec{E}(\vec{r},t) = \frac{1}{2}\sum_k \sum_s A_{ks} e^{i\vec{k}\cdot\vec{r}-i\omega_k t}\omega_k \vec{e}_{ks} \tag{1.2.0.8}$$

The energy of the electromagnetic field contained in volume V, is given by

$$U = \frac{1}{2}\int_V [\epsilon_0 E^2(r,t) + \frac{B^2(r,t)}{2\mu_0}]d^3r \tag{1.2.0.9}$$

Using the equation (1.2.0.9) ,(1.2.0.7) and (1.2.0.8) we get,

$$U = \frac{1}{2\pi}\sum_k \sum_s \frac{\omega_k^2}{c^2}|\vec{A}_{ks}|^2 \tag{1.2.0.10}$$

When we quantize the electromagnetic field, all the electric field and magnetic field vectors $\vec{E}$, $\vec{B}$ and $\vec{A}$ are changed to operators and the energy U is changed to Hamiltonian operator. All quantum fields would now be expressed as

$$\vec{A}(\vec{r},t) = \sum_k \sum_s \hat{a}_{\vec{k}s} e^{i\vec{k}\cdot\vec{r}-i\omega_k t}\alpha\vec{e_{ks}} + H.C. \tag{1.2.0.11}$$

$$\vec{A^*}(\vec{r},t) = \sum_k \sum_s \hat{a}^+_{\vec{k}s} e^{-(i\vec{k}\cdot\vec{r}-i\omega_k t)}\alpha\vec{e_{ks}} + H.C. \tag{1.2.0.12}$$

$$\vec{E}(\vec{r},t) = i\sum_k \sum_s \hat{a}_{\vec{k}s} e^{i\vec{k}\cdot\vec{r}-i\omega_k t}\alpha e_{\vec{k}s}\omega_k + H.C. \tag{1.2.0.13}$$

$$\vec{B}(\vec{r},t) = i\sum_k \sum_s \hat{a}_{\vec{k}s} e^{i\vec{k}\cdot\vec{r}-i\omega_k t}\alpha\omega_k \frac{(\vec{k}\times e_{\vec{k}s})}{|\vec{k}|} + H.C. \tag{1.2.0.14}$$

where $\alpha = \sqrt{\frac{2\pi\hbar c^2}{V}}$, a_{ks} is called as the "annihilation operator" and $\hat{a}^+_{ks}$ is called as the "creation operator". The commutation relation holding between $\hat{a}$ and $\hat{a}^+$ is given by,

$$[\hat{a}_{ks}, \hat{a^+}_{ks}] = 1 \tag{1.2.0.15}$$

Now the equation (1.2.0.10) can be rewritten as

$$\hat{H} = \frac{1}{2}\sum_{k,s} \hbar\omega_k(\hat{a}^+_{ks}\hat{a}_{ks} + \hat{a}_{ks}\hat{a}^+_{ks}) = \sum_{k,s} \hbar\omega_k(\hat{n}_{\vec{k}s} + \frac{1}{2}) \tag{1.2.0.16}$$

where $\hat{n}_{\vec{k}s} = \hat{a}^+_{ks}\hat{a}_{ks}$ is called the number operator for the frequency ω_k is the frequency, the wave vector being $\vec{k} = \omega_k/c$ and c is the velocity of light. More on the properties of the number operator would be discussed in the next subsection 1.2.1.

1.2.1 Fock States

For brevity, we remove the subscript $\vec{k}s$ throughout the discussion of this section and denote the single mode photon number operators as $\hat{n}$. The eigenvectors of number operator $|n\rangle$ are called Fock states, thus we can write:

$$\hat{n}\,|n\rangle = n\,|n\rangle \tag{1.2.1.1}$$

where n represents the eigenvalue of number operator. However the smallest eigenvalue of the number operator is zero since $\hat{n}$ is hermitian operator. For n=0, it can be seen that

$$\hat{n}\,|0\rangle = \hat{a}^+\hat{a}\,|0\rangle = 0 \tag{1.2.1.2}$$

Therefore we can write $a\,|0\rangle = 0$. The state $|0\rangle$ is called the vacuum state as it has no photons associated with radiation field. Its energy obtained according to the equation 1.2.0.16 is called the zero point energy and its contribution is given by $\sum_{k,s}\hbar\omega_k/2$.

Using the commutation relation in equation (1.2.0.15) applying it to the vacuum state holds the following result:

$$(\hat{a}\hat{a}^+ - \hat{a}^+\hat{a})\,|0\rangle = |0\rangle \tag{1.2.1.3}$$

which gives us,

$$\hat{a}(\hat{a}^+\,|0\rangle) = |0\rangle \tag{1.2.1.4}$$

Now we apply the creation operator on both sides to the above equation (1.2.1.4), we get $(\hat{a}^+\hat{a})\hat{a}^+\,|0\rangle = \hat{a}^+\,|0\rangle$. This implies that $\hat{a}^+\,|0\rangle$ is the eigenvector of operator $\hat{a}^+\hat{a}$ whose

eigenvalue is 1. Hence we can write

$$\hat{a}^+ |0\rangle = |1\rangle \tag{1.2.1.5}$$

The $|1\rangle$ is called a single photon state obtained by applying $\hat{a}^+$ on the vacuum state. Similarly the state $|n\rangle$ is formed by repeated application of the the creation operator $\hat{a}^+$ for n times on the vacuum state $|0\rangle$. The state $|n\rangle$ with an appropriate normalizing factor could then be given by,

$$|n\rangle = \frac{(\hat{a}^+)^n}{\sqrt{n!}} |0\rangle \tag{1.2.1.6}$$

Furthermore we could deduce the following properties of annihilation and creation operators as,

$$\hat{a} |n\rangle = \sqrt{n}|n-1>, \hat{a}^+ |n\rangle = \sqrt{n+1}|n+1> \tag{1.2.1.7}$$

1.2.2 Quadrature of field

In the equation (1.2.0.8) the plane wave field has an amplitude E_0 which is a complex number. The information of its real and complex amplitudes can be obtained by performing using certain measurement techniques such as homodyne detection which would be described it in subsection 1.3.2 where the squeezed states are introduced. In quantum optics however, the amplitude E_0 gets replaced by the annihilation operator $\hat{a}$ and its complex conjugate as creation operator $\hat{a}^+$ which do not correspond to any observable since they are not Hermitian. Since all observables are represented by Hermitian operators whose expectation values give a certain measurable value [31], we can thus define the two Hermitian quadrature operators $\hat{X}$ and $\hat{Y}$ which measure the Electric field as:

$$\hat{a} = \frac{\hat{X} + i\hat{Y}}{\sqrt{2}} \tag{1.2.2.1}$$

$$\hat{a}^+ = \frac{\hat{X} - i\hat{Y}}{\sqrt{2}} \tag{1.2.2.2}$$

which gives us,

$$\hat{X} = \frac{\hat{a} + \hat{a}^+}{\sqrt{2}} \tag{1.2.2.3}$$

$$\hat{Y} = \frac{\hat{a} - \hat{a}^+}{\sqrt{2}i} \tag{1.2.2.4}$$

Their commutation relation can be evaluated as,

$$[\hat{X}, \hat{Y}] = i \tag{1.2.2.5}$$

The commutative relation in equation (1.2.2.5) is similar to the position operator and momentum operator.

The Heisenberg uncertainty relationship for operators $\hat{A}$ and $\hat{B}$ which are non commutative is given by[32],

$$\Delta\hat{A}\Delta\hat{B} \geq \frac{|\left\langle[\hat{A},\hat{B}]\right\rangle|}{2} \tag{1.2.2.6}$$

Hence we could construct the Heisenberg uncertainty from the equations (1.2.2.5) and (1.2.2.6) we get,.

$$\Delta\hat{X}\Delta\hat{Y} \geq \frac{1}{2} \tag{1.2.2.7}$$

1.3 Quantum states

In this section we discuss properties of various types of quantum states such as Coherent states, single mode squeezed states and two mode squeezed states.

1.3.1 Coherent States

The coherent states are one of the prominent states in quantum theory of light[30] because their properties closely resemble the one's of classical electromagnetic plane wave. A single mode laser operated well above threshold generates a coherent state excitation [33].

Coherent states are denoted by $|\alpha\rangle$ and can be defined as superposition of fock states $|n\rangle$ given by:

$$|\alpha\rangle = e^{-\frac{|\alpha^2|}{2}} \sum_{n=0}^{\infty} \frac{\alpha^n}{\sqrt{n!}} |n\rangle\,, \tag{1.3.1.1}$$

where α is a complex number.

Properties of coherent states

1. It can be easily verified that the coherent states are normalized.

$$\langle\alpha|\alpha\rangle = e^{-|\alpha^2|} \sum_{n} \frac{\alpha^n}{n!} = 1 \tag{1.3.1.2}$$

2. The coherent states are non-orthogonal to each other. Lets take two states $|\alpha\rangle$ and $|\beta\rangle$.

$$\langle\alpha|\beta\rangle = e^{(\alpha^*\beta - \frac{|\alpha|^2}{2} - \frac{|\beta|^2}{2})} \tag{1.3.1.3}$$

3. It can be seen that coherent states are eigenstates of the annihilation operator with

eigenvalue α.

$$\begin{aligned} a(|\alpha\rangle) = a(e^{-\frac{\alpha^2}{2}} \sum_{n=1}^{\infty} \frac{\alpha^n}{\sqrt{n!}} |n\rangle) &= e^{-\frac{\alpha^2}{2}} \sum_{n=1}^{\infty} \frac{\alpha^n}{\sqrt{n!}} \sqrt{n} |n-1\rangle \\ &= e^{-\frac{\alpha^2}{2}} \sum_{n=1}^{\infty} \frac{\alpha^n}{\sqrt{(n-1)!}} |n-1\rangle \\ &= \alpha(e^{-\frac{\alpha^2}{2}} \sum_{n=1}^{\infty} \frac{\alpha^{(n-1)}}{\sqrt{(n-1)!}} |n-1\rangle) \\ &= \alpha |\alpha\rangle \end{aligned} \tag{1.3.1.4}$$

4. The complex parameter α is related to mean photon number of the field. It is given by,

$$\langle \hat{n} \rangle = \langle \alpha | \hat{n} | \alpha \rangle = \langle \alpha | \hat{a}^+ \hat{a} | \alpha \rangle = |\alpha|^2 \tag{1.3.1.5}$$

The second order momentum of the photon number distribution is given by,

$$\langle \hat{n}^2 \rangle = \langle \alpha | \hat{n}^2 | \alpha \rangle = \langle \alpha | \hat{a}^+ \hat{a} \hat{a}^+ \hat{a} | \alpha \rangle = |\alpha|^2 (1 + \langle \alpha | \hat{a}^+ \hat{a} | \alpha \rangle) = |\alpha|^2 + |\alpha|^4 \tag{1.3.1.6}$$

Hence the Variance of the photon number is given by

$$\mathrm{var}(\hat{n}) = \langle n^2 \rangle - \langle \hat{n} \rangle^2 = \langle \hat{n} \rangle \tag{1.3.1.7}$$

The photon number distribution of $p(N)$ is given by :

$$p(N) = |\langle N | \alpha \rangle|^2 = e^{-\alpha^2} \sum_{n=0}^{\infty} \frac{\alpha^n}{\sqrt{n!}} |\langle N | n \rangle|^2 = \frac{e^{-\langle \hat{n} \rangle} \langle \hat{n} \rangle^N}{N!} \tag{1.3.1.8}$$

The above probability distribution represents a Poissonian distribution with variance in the photon number as demonstrated to be equal to mean photon number. The relative intensity noise of a coherent state is given by the ratio of the standard deviation of the photon number to the expectation value of the mean photon number of the coherent state.

$$\frac{\Delta I}{\langle I \rangle} = \frac{\Delta n}{\langle n \rangle} = \frac{1}{\sqrt{\langle n \rangle}} \tag{1.3.1.9}$$

where I is the intensity of the coherent light. Hence the relative intensity noise is limited by $\langle n \rangle$. This limit is called as Shot noise limit.

5. The coherent states can be generated by displacing the vacuum state, $|\alpha\rangle = D(\alpha) |0\rangle$, where $D(\alpha)$ is called as the displacement operator. It is given by:

$$D(\alpha) = e^{(\alpha \hat{a}^+ - \alpha^* a)} \tag{1.3.1.10}$$

It is shown pictorially in fig. 1.1 in XY quadrature space.

6. Let us evaluate the uncertainties on the quadratures $\Delta \hat{X}$ and $\Delta \hat{Y}$ using the above properties.

$$\Delta\hat{X} = \sqrt{\left\langle \hat{X}^2 \right\rangle - \left\langle \hat{X} \right\rangle^2} = \sqrt{\langle\alpha| \hat{X}^2 |\alpha\rangle - (\langle\alpha| \hat{X} |\alpha\rangle)^2}$$

Using $\hat{X}$ as in equation (1.2.2.3)

$$\left\langle \hat{X} \right\rangle = \frac{\langle\hat{a}\rangle + \langle\hat{a}^+\rangle}{2} = \text{Real}(\alpha) \tag{1.3.1.11}$$

Similarly the second order moment of quadrature $\hat{X}$ is given by,

$$\left\langle \hat{X}^2 \right\rangle = \frac{\left\langle (\hat{a}^2 + \hat{a}^{+2} + \hat{a}\hat{a}^+ + \hat{a}^+\hat{a} \right\rangle}{4} = \frac{\alpha^2 + \alpha^{*2} + 2\alpha\alpha^* + 1}{4} = \frac{1 + 4\text{Real}(\alpha)^2}{4} \tag{1.3.1.12}$$

Hence the uncertainty is evaluated as using equation (1.3.1),

$$\Delta\hat{X} = \frac{1}{\sqrt{2}} \tag{1.3.1.13}$$

In similar way we can show that $\Delta Y = \frac{1}{\sqrt{2}}$. Hence the Coherent states are known as the minimum uncertainty states with the uncertainties in the quadratures $\Delta\hat{X} = \frac{1}{\sqrt{2}}$ and $\Delta\hat{Y} = \frac{1}{\sqrt{2}}$ with $\Delta\hat{X}\Delta\hat{Y} = \frac{1}{2}$. The fig. 1.1 represents the quadrature space of the coherent state.

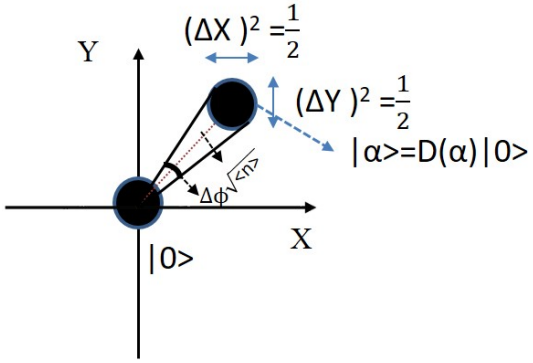

Figure 1.1: The figure above shows the pictorial representation of coherent state in Quadrature XY space. It can be seen that the coherent state is obtained by the displacement operator $D(\alpha)$.

8. The phase uncertainty limit based on the Fisher information is given by,

$$(\Delta\phi) = \frac{1}{2\sqrt{\text{var}(\hat{n}_{sig})}} = \frac{1}{2\sqrt{N}} \tag{1.3.1.14}$$

This fundamental limit is called the shot noise limit. Considering the above equation we can establish the number-phase uncertainty relationship as:

$$\Delta n \Delta\phi = \frac{1}{2} \tag{1.3.1.15}$$

1.3.2 Single mode Squeezed States

Squeezed states are the type of quantum states which compress the uncertainty in one quadrature at the expense of the other whilst maintaining the Heisenberg uncertainty limit. The Squeezing operator is defined as,

$$S(\xi) = e^{(\frac{\xi a^{+2}}{2} - \frac{\xi^* a^2}{2})},\ \xi = re^{i\psi} \tag{1.3.2.1}$$

It can be seen that the Squeezing operator satisfies the conditions for unitary operator,

$$S(\xi)S^{+}(\xi) = S^{+}(\xi)S(\xi) = 1 \tag{1.3.2.2}$$

The squeezed vacuum state $|\xi\rangle$ is given by,

$$|\xi\rangle = S(\xi)\,|0\rangle \tag{1.3.2.3}$$

The final form of the squeezed vacuum state can be written as [30],

$$|\xi\rangle = \frac{1}{\sqrt{\text{cosh}r}} \sum_{n=0}^{\infty} e^{in\psi} (\text{tanh}r)^n \frac{\sqrt{(2n)!}}{n!2^n}\,|2n\rangle \tag{1.3.2.4}$$

Properties of Squeezed vacuum and Squeezing operator

1. The squeezing operator transforms the annihilation and creation operator as $b = S^{+}(\xi)\hat{a}^{+}S(\xi)$ and $\hat{b}^{+} = S^{+}(\xi)aS(\xi)$. The final form of the operator is given by:

$$\begin{aligned} b &= S^{+}(\xi)\hat{a}^{+}S(\xi) = \hat{a}\text{cosh}(r) + \hat{a}^{+}e^{i\psi}\text{sinh}(r) \\ \hat{b}^{+} &= S^{+}(\xi)aS(\xi) = \hat{a}^{+}\text{cosh}(r) + \hat{a}e^{-i\psi}\text{sinh}(r) \end{aligned} \tag{1.3.2.5}$$

where ψ is an appropriate phase and r is the squeezing factor. This transformation is also known as Bougliubov transform. The evolved operators also satisfy the non-commutative property as $[b, \hat{b}^{+}] = 1$

2. The Quadrature operators $\hat{X}_\theta$ which is a linear combination of quadratures $\hat{X}$ and $\hat{Y}$ are defined as,

$$\hat{X}_\theta = \frac{be^{(-i\theta)} + b^{+}e^{(i\theta)}}{\sqrt{2}} \tag{1.3.2.6}$$

which for values of $\theta = 0(\pi/2)$ reduces to qudratures $\hat{X}$ ($\hat{Y}$).

We try to evaluate the uncertainty in the quadratures $\Delta\hat{X}$ and $\Delta\hat{Y}$ by evaluating $\Delta\hat{X}_\theta$ given by,

$$(\Delta\hat{X}_\theta)^2 = \left\langle \hat{X}_\theta^2 \right\rangle - \left\langle \hat{X}_\theta \right\rangle^2 \tag{1.3.2.7}$$

The expectation value of the quadrature $\hat{X}_\theta$,

$$\begin{aligned}\left\langle \hat{X}_\theta \right\rangle = \left\langle \frac{be^{-i\theta} + b^+e^{i\theta}}{\sqrt{2}} \right\rangle &= \langle \xi | \frac{be^{-i\theta} + b^+e^{i\theta}}{\sqrt{2}} | \xi \rangle \\ &= \frac{\langle b \rangle e^{-i\theta} + \left\langle \hat{b}^+ \right\rangle e^{i\theta}}{\sqrt{2}}\end{aligned} \tag{1.3.2.8}$$

The first term in the above equation (1.3.2.8) is given by,

$$\langle b \rangle = \langle a \rangle + e^{i\psi} \left\langle \hat{a}^+ \right\rangle = 0 \tag{1.3.2.9}$$

where the the mean value $\langle . \rangle$ is intended to be evaluated on the Squeezed vacuum state. Hence the $\left\langle \hat{X}_\theta \right\rangle = 0$

The expectation value of $\hat{X}_\theta^2$ is given by,

$$\begin{aligned}\left\langle \hat{X}_\theta^2 \right\rangle = \langle \xi | \hat{X}_\theta^2 | \xi \rangle &= \langle \xi | b^2e^{-2i\theta} + b^{+2}e^{2i\theta} + b\hat{b}^+ + \hat{b}^+b | \xi \rangle \\ &= \left\langle b^2 \right\rangle + \left\langle b^{+2} \right\rangle + \left\langle b\hat{b}^+ \right\rangle + \left\langle \hat{b}^+b \right\rangle\end{aligned} \tag{1.3.2.10}$$

For brevity, let us define $u = \cosh(r)$ and $v = \sinh(r)$ The expectation value of each term can be evaluated as,

$$\begin{aligned}\left\langle b^2 \right\rangle &= uve^{i\psi} \\ \left\langle b^{+2} \right\rangle &= uve^{-i\psi} \\ \left\langle \hat{b}^+b \right\rangle &= |v|^2\end{aligned} \tag{1.3.2.11}$$

We get the expectation value of $\hat{X}_\theta^2$ as

$$\left\langle \hat{X}_\theta^2 \right\rangle = \frac{1}{2} + v(v + \sqrt{1+v^2}cos(2\theta - \psi)) \tag{1.3.2.12}$$

Without loss of generality, we set $\psi = 0$ and evaluating the $\left\langle \hat{X}_\theta^2 \right\rangle$ at $\theta = 0$ and $\theta = \pi/2$, we get

$$\begin{aligned}\left\langle \hat{X}^2 \right\rangle &= \frac{e^{2r}}{2} \\ \left\langle \hat{Y}^2 \right\rangle &= \frac{e^{-2r}}{2}\end{aligned} \tag{1.3.2.13}$$

Then evaluating the uncertainties $\Delta\hat{X}$ and $\Delta\hat{Y}$ we get,

$$\begin{aligned}\Delta\hat{X} &= \sqrt{\left\langle \hat{X}^2 \right\rangle - (\left\langle \hat{X} \right\rangle)^2} = \frac{e^r}{\sqrt{2}} \\ \Delta\hat{Y} &= \sqrt{\left\langle \hat{X}^2 \right\rangle - (\left\langle \hat{X} \right\rangle)^2} = \frac{e^{-r}}{\sqrt{2}}\end{aligned} \tag{1.3.2.14}$$

The equations (1.3.2.14) shows that they satisfy the uncertainty relation $\Delta\hat{X}\Delta Y = \frac{1}{2}$.

The squeezed vacuum state in the XY-quadrature space, is pictorially represented as ellipse as seen in fig. 1.2. One of the quadrature is compressed in uncertainty at the expense of increase of the other quadrature with uncertainty.

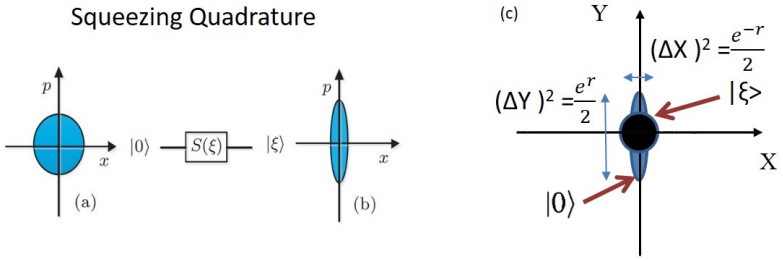

Figure 1.2: The figure above represents the pictorial representation of Squeezed vacuum state. It can bee seen that the uncertainty in one quadrature is compressed at the expense of the other.

Squeezed states can be generated, for instance, through a process of parametric down conversion. This would be eventually discussed in Chapter 3 in section 3.3.1.

3. The amount of squeezing produced by squeezer can be measured by using a balanced homodyne detection scheme. In this scheme, the squeezed light is interfered with a coherent local oscillator on a beam splitter and the photon number signals between the output ports c_1 and c_2 is subtracted. Let b_1 port be injected with coherent local oscillator $|\alpha\rangle = \left|\mu e^{i\phi}\right\rangle$while b_2 has in input squeezed vacuum $|\xi\rangle$. The fig. 1.3 depicts the scheme of the homodyne detection.

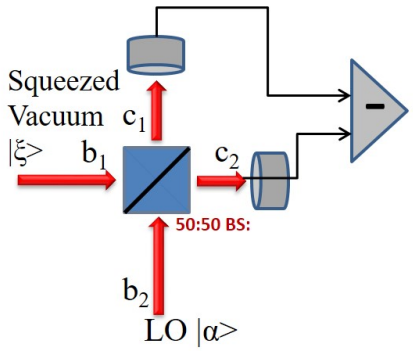

Figure 1.3: The figure above depicts the homodyne scheme for measuring the quadratures. The output port c_1 and c_2 are subtracted.

The operators c_1 and c_2 are given by,

$$\hat{c}_1 = \frac{\hat{b}_1 + i\hat{b}_2}{\sqrt{2}}, \hat{c}_2 = \frac{\hat{b}_2 + i\hat{b}_1}{\sqrt{2}} \tag{1.3.2.15}$$

The number of photons exiting in c_1 is given by $\langle N_1\rangle = \left\langle \hat{c}_1^{+}\hat{c}_1\right\rangle$ and similarly in port c_2 is given by $N_2 = \left\langle \hat{c}_2^{+}\hat{c}_2\right\rangle$. When we perform the subtraction,

$$\begin{aligned}\langle N_1 - N_2\rangle &= \left\langle \hat{c}_1^+ \hat{c}_1 \right\rangle - \left\langle \hat{c}_2^+ \hat{c}_2 \right\rangle \\ &= \left\langle \hat{b}_1^+ b_1 + \hat{b}_2^+ \hat{b}_2 + i(\hat{b}_1^+ \hat{b}_2 - \hat{b}_2^+ \hat{b}_1) \right\rangle - \left\langle \hat{b}_1^+ b_1 + \hat{b}_2^+ \hat{b}_2 - i(\hat{b}_1^+ \hat{b}_2 - \hat{b}_2^+ b_1) \right\rangle \\ &= 2i \left\langle ((\hat{b}_1^+ \hat{b}_2 - \hat{b}_2^+ \hat{b}_1) \right\rangle = 2\sqrt{\mu} \left\langle e^{i(\phi+\pi/2)} \hat{b}_2 - e^{-i(\phi+\pi/2)} \hat{b}_2^+ \right\rangle \\ &= \sqrt{2\mu} \left\langle \hat{X}_{\phi+\pi/2} \right\rangle\end{aligned} \tag{1.3.2.16}$$

At the same time, it can be shown that the variance in difference of photon number is proportional to the variance of the quadrature according to the following expression:

$$\mathrm{var}(N_1 - N_2) = \left\langle (N_1 - N_2)^2 \right\rangle - (\langle N_1 - N_2 \rangle)^2 = 2\mu^2 (\Delta X_{\phi+\pi/2})^2. \tag{1.3.2.17}$$

It can be inferred from the above two expressions that when we perform the subtraction, the expectation value and variances are proportional to the quadratures of the field. If the phase $\phi = -\pi/2$, we measure the anti-squeezing quadrature of the field, while $\phi = 0$ measures the squeezing quadrature of the field. This phase ϕ is in general controlled by a phase shifter which is described in section 5.1

4. Combining squeezing and displacement operator, one can generate the squeezed coherent states defined by [30][32],

$$|\xi, \beta\rangle = D(\beta) S(\xi) |0\rangle \tag{1.3.2.18}$$

i) The annhilation operators are transformed into $a(\xi, \beta)$ given by,

$$c = S^+(\xi) D^+(\beta) a D(\beta) S(\xi) = a\cosh(r) + \hat{a}^+ + e^{i\psi}\sinh(r) + \beta \tag{1.3.2.19}$$

It should be noted that $D(\beta)$ and $S(\xi)$ do not commute with each other.

ii)The expectation values are given by :

$$\langle c \rangle = \beta, \left\langle \hat{a}^+ a \right\rangle = |\beta|^2 + \sinh^2(r) \tag{1.3.2.20}$$

$$\left\langle c^2 \right\rangle = \beta^2 + \frac{\sinh 2r\, e^{i\psi}}{2}, \left\langle \hat{X}_\theta \right\rangle = \frac{\beta e^{-i\theta} + \beta e^{i\theta}}{\sqrt{2}} \tag{1.3.2.21}$$

Hence the variance in the quadratures is given by,

$$(\Delta \hat{X}_{\frac{\psi}{2}})^2 = \frac{e^{2r}}{2}, (\Delta \hat{X}_{\frac{\psi}{2}+\frac{\pi}{2}})^2 = \frac{e^{-2r}}{2} \tag{1.3.2.22}$$

It can be seen that they satisfy the Heisenberg uncertainty relation $\Delta \hat{X}_{\frac{\psi}{2}} \Delta \hat{X}_{\frac{\psi}{2}+\frac{\pi}{2}} = \frac{1}{2}$.

(iii) There are two types of Displaced squeezed vacuum states that we can represent in the XY quadrature space as shown in fig. 1.4. The fig. 1.4 (a) shows the amplitude squeezed state and fig. 1.4 (b) shows the phase squeezed state

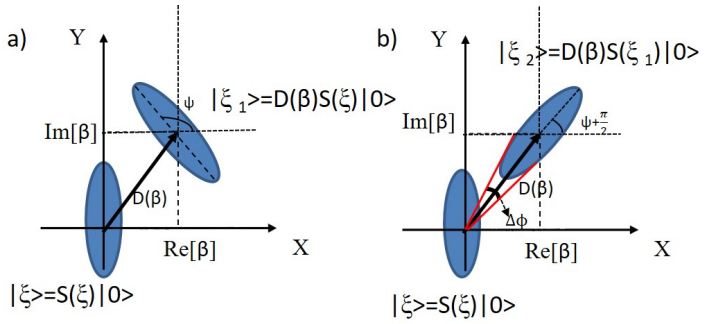

Figure 1.4: a) Amplitude squeezed b) Phase squeezed where $\xi_1 = \xi e^{i\frac{\pi}{2}}$

The two ellipses represent two orthogonal squeezed states: we observe that one squeezed state shows less fluctuations than a coherent state in the angular phase (phase squeezing), while the other state shows less fluctuations in the direction of α (amplitude or intensity squeezing). This squeezing angle is controlled by a seed beam or control beam which is discusses in chapter 3 in section 3.3.1. Phase squeezed states have a super-Poissonian statistics, while amplitude squeezed states, for $|\alpha|$ sufficiently large, are an example of sub-Poissonian distribution whereas its phase distribution is wider[32][34]. We can establish the uncertainty in photon number and phase as $\Delta n = \sqrt{n}e^{-r}$ and $\Delta\phi = \frac{e^r}{2\sqrt{n}}$. Whilst for the phase-squeezed light, it has reduction of the uncertainty in the phase fluctuations $\Delta n = \sqrt{n}e^{r}$ and $\Delta\phi = \frac{e^{-r}}{2\sqrt{n}}$ with respect to a coherent state of the same amplitude. The phase squeezing is useful for injection into the interferometers because of its low phase fluctuations.

1.3.3 Two Mode Squeezing

A state that is closely related to the single-mode squeezed vacuum in its theoretical description and experimental procedures, but quite different in properties is the two mode squeezed vacuum (TMSV), also known as the twin-beam state [35]. We generate two mode squeezed states by applying the two mode squeezing operator on the two mode vacuum state $|0,0\rangle$,

$$S_{ab}(\xi) = e^{(\xi\hat{a}^+\hat{b}^+ - \xi^*\hat{a}\hat{b})},\ \xi = re^{i\psi} \tag{1.3.3.1}$$

$$|\xi_{twb}\rangle = S(\xi)\,|0,0\rangle \tag{1.3.3.2}$$

The final form of the two mode squeezed vacuum state are given by,

$$|\xi_{twb}\rangle = \frac{1}{\cosh(r)}\sum_{n=0}^{\infty} e^{in\psi}(\tanh r)^n\,|n,n\rangle \tag{1.3.3.3}$$

By evolving the input operator a and b by the two-mode squeezing operator, i.e

$$\hat{c} = S_{ab}^{+}(\xi)\hat{a}S_{ab}(\xi),\ \hat{d} = S_{ab}^{+}(\xi)\hat{b}S_{ab}(\xi) \tag{1.3.3.4}$$

It turns out that the output operators can be expressed by the following Bogoliubov equation:

$$\hat{c} = \hat{a}\cosh(r) + \hat{b}^{+}\, e^{i\psi}\sinh(r),\ \hat{d} = \hat{b}\cosh(r) + \hat{a}^{+}\, e^{i\psi}\sinh(r) \tag{1.3.3.5}$$

The TWB presents perfect correlations in the photon number between two modes a $\hat{N_a} = \hat{c}^{+}\hat{c}$ and mode b $\hat{N_b} = \hat{d}^{+}\hat{d}$ meaning that $\langle \xi_{ab}| \left(N_a - N_b\right)^M |\xi_{ab}\rangle = 0,\ \forall\, M > 0$. It implies for example that variance of the photons numbers difference $\left\langle \delta(N_a - N_b)^2 \right\rangle$ is identically null if losses are neglected.

The expectation value of correlation between two modes is given by,

$$\left\langle \hat{c}\hat{d} \right\rangle = \cosh(r)\sinh(r)\, e^{i\psi} \tag{1.3.3.6}$$

The other properties could be evaluated such as $\left\langle \hat{c}^2 \right\rangle = \left\langle \hat{d}^2 \right\rangle = 0,\ \langle \hat{c} \rangle = \left\langle \hat{d} \right\rangle = 0$. The correlation $\left\langle \hat{c}\hat{d} \right\rangle$ between the two modes leads to non-classical properties like single mode squeezed vacuum state. The non vanishing of $\left\langle \hat{c}\hat{d} \right\rangle$ suggests that we must consider quadratures of the operators which are linear combinations of $\hat{c}$ and $\hat{d}$,

$$\hat{g} = \frac{\hat{a} + \hat{b}}{\sqrt{(}2)} \tag{1.3.3.7}$$

satisfying $[\hat{g}, \hat{g}^{+}] = 1$ The second order moments for $\hat{g}$ are given by [30],

$$\left\langle g^{+} g \right\rangle = \sinh^2 r,\ \left\langle g^2 \right\rangle = \cosh(r)\sinh(r) e^{i\psi} \tag{1.3.3.8}$$

The above expression is similar to the single mode squeezed vacuum with reference to (1.3.2.11). Hence defining the quadrature operator $\hat{X}_\theta$ similar to one in the single mode squeezed vacuum:

$$\hat{X}_\theta^{(g)} = \frac{\hat{g}e^{-i\theta} + \hat{g}^{+}e^{i\theta}}{\sqrt{2}} \tag{1.3.3.9}$$

we would get $\Delta\hat{X}^{(g)}_{\frac{\psi}{2}+\frac{\pi}{2}} = \frac{1}{2}(1 - e^{-2r})$

Similarly we can define another linear combination operator c as

$$\hat{h} = \frac{\hat{b} - \hat{a}}{\sqrt{2}} \tag{1.3.3.10}$$

satisfying the non commutativity $[\hat{h}, \hat{h}^{+}] = 1$.

We can note that $\frac{(\hat{h}^2 - \hat{g}^2)}{2} = \hat{a}\hat{b}$ and hence we can rewrite the two mode squeezed vacuum state as,

$$e^{(\xi\hat{a}^{+}\hat{b}^{+} - \xi^{*}ab)} = e^{(\frac{\xi}{2}g^{+2} - \frac{\xi^{*}}{2}g^2)} e^{(-\frac{\xi}{2}h^{+2} + \frac{\xi^{*}}{2}h^2)} \tag{1.3.3.11}$$

Thus the two mode squeezing operator can be written as a product of two-single mode states operators. It can be noted that operators c and d can be realized by 50-50 beam splitter. Hence the generation of twin beam states can be done using two single mode squeezed states interfered on the beam splitter as shown in fig. 1.5.

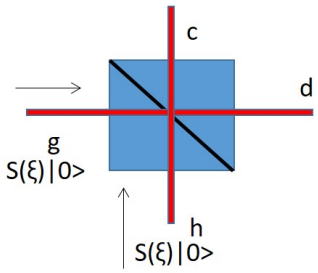

Figure 1.5: The above figure represents the generation of twin beam state with two single mode squeezers interfered on a beam splitter.

Since we now know that the two mode squeezed state is generated through two single mode squeeeezed vacuum states interfered on the beam splitter, we can calculate the uncertainties in quadratures. There are four quadratures in total to be considered, two corresponding to each mode of the field defined by,

$$\hat{X}_{1,\theta} = \frac{\hat{c}e^{i\theta} + \hat{c}^{+}e^{-i\theta}}{\sqrt{2}},\ \hat{X}_{2,\theta} = \frac{\hat{d}e^{i\theta} + \hat{d}^{+}e^{-i\theta}}{\sqrt{2}} \tag{1.3.3.12}$$

Let us consider the difference in two quadrature of two modes,

$$\left\langle (\hat{X}_{(1,0)} - \hat{X}_{(2,0)}) \right\rangle = \frac{\left\langle \hat{c} - \hat{d} + \hat{c}^{+} - \hat{d}^{+} \right\rangle}{\sqrt{2}} = 0 \tag{1.3.3.13}$$

Now we evaluate the variance of the difference as

$$\mathrm{var}(\hat{X}_{(1,0)} - \hat{X}_{(2,0)}) = \mathrm{var}(\hat{X}_{(1,0)}) + \mathrm{var}(\hat{X}_{(2,0)}) - 2\left\langle (\hat{X}_{(1,0)}, \hat{X}_{(2,0)}) \right\rangle. \tag{1.3.3.14}$$

We can evaluate $\mathrm{var}(\hat{X}_{(1,0)}) = \left\langle \hat{X}^2_{(1,0)} \right\rangle - \left\langle \hat{X}_{(1,0)} \right\rangle^2$ The second term in the above expression is zero. Hence the second order moment of the operator is given by,

$$\left\langle \hat{X}^2_{(1,0)} \right\rangle = \frac{\hat{c}^2 + \hat{c}^{+2} + \hat{c}\hat{c}^{+} + \hat{c}^{+}\hat{c}}{2} = \frac{(1 + 2\mathrm{sinh}^2(r))}{2} \tag{1.3.3.15}$$

Similarly, $\left\langle \hat{X}^2_{2,0} \right\rangle = \frac{1}{2}(1 + 2\sinh^2 r)$.

The covariance of the two quadratures is given by,

$$\left\langle \hat{X}_{(1,0)}\hat{X}_{(2,0)} \right\rangle = \frac{\hat{c}^{+}\hat{d} + \hat{c}\hat{d}^{+} + \hat{c}\hat{d} + \hat{c}^{+}\hat{d}^{+}}{2} = -\mathrm{sinh}(r)\mathrm{cosh}(r)\mathrm{sin}(\psi) \tag{1.3.3.16}$$

Without loss of generality we put $\psi = \pi/2$

Hence we can evaluate the variance of the difference in quadratures as ,

$$\mathrm{var}(\hat{X}_{(1,0)} - \hat{X}_{(2,0)}) = \frac{e^{-2r}}{2} \tag{1.3.3.17}$$

Similarly when we evaluate the variances of the sum of the other two quadratures we

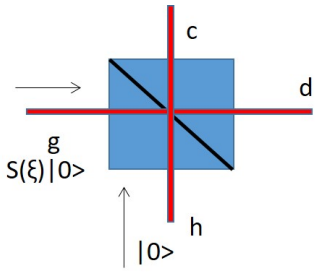

Figure 1.6: The figure above shows the generation of twin beam like state by splitting a single mode squeezer on a beam splitter.

get $\text{var}(\hat{X}_{(1,\frac{\pi}{2})} + \hat{X}_{(2,\frac{\pi}{2})}) = \frac{e^{2r}}{2}$ satisfying the Heisenberg's uncertainty principle:

$$\Delta(\hat{X}_{(1,0)} - \hat{X}_{(2,0)})\Delta(\hat{X}_{(1,\frac{\pi}{2})} + \hat{X}_{(2,\frac{\pi}{2})}) = \frac{1}{2} \tag{1.3.3.18}$$

5. A twin beam like state which produces anti-correlations can be generated by having a single mode squeezer split on a beam splitter as shown in fig. 1.6.

Let us now consider the variance of difference between quadratures $\hat{X}_{(1,0)}$ and $\hat{X}_{(2,0)}$.

$$\text{var}(\hat{X}_{(1,0)} - \hat{X}_{(2,0)}) = \text{var}(\hat{X}_{(1,0)}) + \text{var}(\hat{X}_{(2,0)}) - 2\left\langle(\hat{X}_{(1,0)}, \hat{X}_{(2,0)})\right\rangle \tag{1.3.3.19}$$

where, $\hat{X}_{(1,0)} = \frac{(\hat{c}+\hat{c}^+)}{\sqrt{2}}$ and $\hat{X}_{(2,0)} = \frac{(\hat{d}+\hat{d}^+)}{\sqrt{2}}$

The expressions of output operators $\hat{c}$ and $\hat{d}$ can be written in terms of input operators $\hat{g}$ and $\hat{h}$ through beam splitter,

$$c = \frac{\hat{g}+\hat{h}}{\sqrt{2}},\ d = \frac{\hat{g}-\hat{h}}{\sqrt{2}} \tag{1.3.3.20}$$

From the above expression we can evaluate,

$$\text{var}(\hat{X}_{(1,0)}) = \frac{(1+\cosh(2\,r)+\sinh(2\,r))}{4} \tag{1.3.3.21}$$

$$\text{var}(\hat{X}_{(2,0)}) = \frac{(1+\cosh(2\,r)+\sinh(2\,r))}{4} \tag{1.3.3.22}$$

and

$$\left\langle(\hat{X}_{(1,0)}, \hat{X}_{(2,0)})\right\rangle = \frac{(1+\cosh(2\,r)-\sinh(2\,r))}{4} \tag{1.3.3.23}$$

The variance of the difference is then given by,

$$\text{var}(\hat{X}_{(1,0)} - \hat{X}_{(2,0)}) = \frac{e^{-2r}}{2} \tag{1.3.3.24}$$

Similarly when we evaluate the $\text{var}(\hat{X}_{(1,\frac{\pi}{2})} - \hat{X}_{2,\frac{\pi}{2}}) = \frac{e^{2r}}{2}$

1.4 Phase sensing in Michelson interferometers

Michelson Interferometer has been an extremely important tool in phase sensing experiments and are used in applications as gravitational wave detector[36][21]. The Michelson interferometer consists of a beam splitter and two end mirrors as shown in the fig. 1.7. More details of the Michelson interferometer are presented in Chapter 2. In this section we discuss various quantum limits with respect to each state injected in the Michelson interferometer. We will discuss two types of detection schemes : (i) Balanced homodyne detection and (ii) Dark port readout.

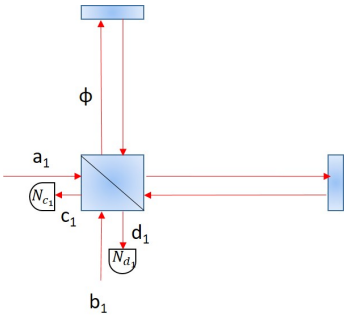

Figure 1.7: The figure above depicts the Michelson interferometer. The coherent state is injected in port a_1. The port c_1 is called the antisymmetric and d_1 is called the symmetric port. When the phase of the arms is set to make the intensity output at the antisymmetric port it can be called "dark" port and while the other one becomes "bright"

1.4.1 Phase Sensing using Dark -port readout

The field of quantum metrology broadly started when Caves showed theoretically that squeezed states of light could be used to suppress quantum noise in an inteferometric phase measurement [37]. The effect of squeezed state injected can be seen by looking at just the dark port output of the interferometer. Let us consider T as transmittivity of the interferometer given by $T = \cos^2(\theta/2)$ and coherent state $\left|\mu e^{i\phi}\right\rangle$ in b_1 with μ photons and squeezed vacuum state with photons n_1 in b_2 as depicted in fig. 1.8. Then the output port operators c_1 and c_2 are given by,

$$\hat{c}_1 = \sqrt{T}\,\hat{b}_1 + i\sqrt{1-T}\,\hat{b}_2,\ \hat{c}_2 = \sqrt{T}\,\hat{b}_2 + i\sqrt{1-T}\,\hat{b}_1 \tag{1.4.1.1}$$

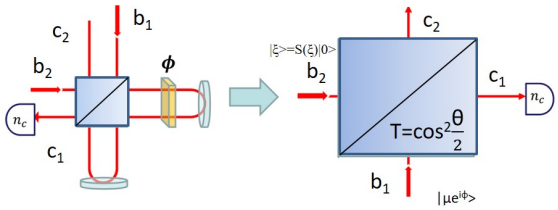

Figure 1.8: The figure above represents the model for Michelson interferometer phase sensing using dark port readout. The port b_1 has coherent state and port b_2 has squeezed light injected into the system. We look at the dark port output c_1.

Then the expectation value of number of photons in the output port is given by,

$$\begin{aligned}\left\langle \hat{c}_1^+ \hat{c}_1 \right\rangle &= T \left\langle \hat{b}_1^+ \hat{b}_1 \right\rangle + (1-T) \left\langle \hat{b}_2^+ \hat{b}_2 \right\rangle + i\sqrt{T(1-T)} \left\langle (\hat{b}_1^+ \hat{b}_2 - \hat{b}_2^+ \hat{b}_1) \right\rangle \\ &= T\lambda + (1-T)\mu + \sqrt{T(1-T)}\sqrt{2\mu} \left\langle \hat{X}_{\phi+\frac{\pi}{2}} \right\rangle \\ &= T\lambda + (1-T)\mu \end{aligned} \tag{1.4.1.2}$$

We then evaluate the variance in number of photons,

$$\mathrm{var}(\hat{c}_1^+ \hat{c}_1) = \left\langle \hat{c}_1^+ \hat{c}_1 \hat{c}_1^+ \hat{c}_1 \right\rangle - \left\langle \hat{c}_1^+ \hat{c}_1 \right\rangle^2 \tag{1.4.1.3}$$

$$\begin{aligned}\left\langle \hat{c}_1^+ \hat{c}_1 \hat{c}_1^+ \hat{c}_1 \right\rangle = T^2 \left\langle n_1^2 \right\rangle + (1-T)^2\mu^2 + (1-T)\mu + T(1-T)\left\langle n_1 \right\rangle + 4T(1-T)\left\langle n_1 \right\rangle \mu \\ -T(1-T)\mu(e^{2i\psi}\left\langle \hat{b}_1^{+2} \right\rangle + e^{-2i\phi}\left\langle \hat{b}_1^2 \right\rangle)\end{aligned} \tag{1.4.1.4}$$

Thus the final form of the variance is given by,

$$\mathrm{var}(\hat{c}_1^+ \hat{c}_1) = T^2 \mathrm{var}(n_1) + T(1-T)\left\langle n1 \right\rangle + (1-T)\mu\Big(1 + 2T\left\langle n_1 \right\rangle - 2T\,u\,v\cos(2\phi)\Big) \tag{1.4.1.5}$$

Without loss of generality we choose $\phi = 0$ and put $T \approx 1$ (evaluating near to the dark fringe) in equation (1.4.1.5), we get

$$\mathrm{var}(\hat{c}_1^+ \hat{c}_1) \approx T^2 \mathrm{var}(n_1) + T(1-T)\mu e^{-2r} + (1-T)^2\mu \tag{1.4.1.6}$$

The variance in photon number of the squeezed light can be evaluated as $\mathrm{var}(n_1) = \mathrm{var}(\mathrm{b}_1^+ \mathrm{b}_1) = 2\lambda + 2\lambda^2$ where $\lambda = \sinh^2 r$. Hence we can write the equation (1.4.1.6) as :

$$\mathrm{var}(\hat{c}_1^+ \hat{c}_1) = \lambda T(2T\lambda + T + 1) + T(1-T)\mu e^{-2r} + (1-T)^2\mu \tag{1.4.1.7}$$

We work at a phase where the interferometer is very close to the dark fringe. Although the output at the anti-symmetric port is near to the dark fringe, it is much stronger than

the photons in the squeezed light. Hence we consider the condition $(1-T)\mu >> T\lambda$ giving the variance as ,

$$\mathrm{var}(\hat{c}_1^+\hat{c}_1) \approx T(1-T)\mu e^{-2r} + (1-T)^2\mu \tag{1.4.1.8}$$

Similarly using equation (1.4.1.2), $\langle \hat{c}_1^+\hat{c}_1 \rangle$ can be written as,

$$\langle \hat{c}_1^+\hat{c}_1 \rangle \approx (1-T)\mu \tag{1.4.1.9}$$

The uncertainty in the phase is then given by,

$$\Delta\theta_{sqz} = \frac{\sqrt{\mathrm{var}(\hat{c}_1^+\hat{c}_1)}}{\left|\frac{\partial\langle \hat{c}_1^+\hat{c}_1\rangle}{\partial\theta}\right|} \tag{1.4.1.10}$$

Then the final form of the above equation is given by,

$$\Delta\theta_{sqz} = \frac{\sqrt{\sin^2(\frac{\theta}{2}) + \cos^2(\frac{\theta}{2})e^{-2r}}}{\cos(\frac{\theta}{2})\sqrt{\mu}} \tag{1.4.1.11}$$

The classical limit is given by putting $\sinh^2 r = 0$ which corresponds to mean number of photons of the squeezed state field being equating to vacuum state. Hence the classical limit is given by,

$$\Delta\theta_{classical} = \frac{\sqrt{2}}{\sqrt{\mu(1+\cos\phi)}} \tag{1.4.1.12}$$

and when $\phi = 0$,

$$\Delta\theta_{classical} = \frac{1}{\sqrt{\mu}} \propto \frac{1}{\sqrt{P}} \tag{1.4.1.13}$$

The equation (1.4.1.12) represents the standard quantum limit (SQL), also called the shot noise limit. This lower bound to the uncertainty in phase measurement is reached by the coherent states. Hence to further reduce the uncertainty using classical coherent states we need to increase the input power P where $\langle P \rangle = \mu\hbar\omega$. This cannot be done arbitrarily because, further increase of the power would lead to additional thermal noise and radiation pressure noise on the mirrors. Hence the optimal way to reduce the uncertainty is obtained by injecting quantum states into the interferometers and in particular squeezed state of light. Hence when we inject the squeezed light, the uncertainty $\Delta\theta_{sqz}$ can be rewritten in terms of uncertainty in classical limit as,

$$\Delta\theta_{sqz} = \Delta\theta_{classical}(\sqrt{(1-T) + Te^{-2r}}) \tag{1.4.1.14}$$

When we are much closer to dark fringe i.e, $T \approx 1$ we get $\Delta\theta_{sqz} = \Delta\theta_{classical}e^{-r}$.

In general we have to consider the inefficiency transmission losses η from the optics to the detector. This inefficiency can be taken into account by representing the dark port splitting on a beam splitter with a ratio η which is the loss as shown in fig. 1.9,

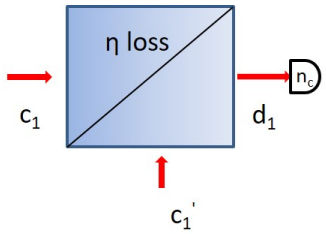

Figure 1.9: The figure above represents model for taking account of losses η. The dark port is considered to split on a beam splitter with a ratio of η

$$\hat{d} = \sqrt{\eta}\hat{c}_1 + (1 - \sqrt{\eta})\hat{c}_1' \tag{1.4.1.15}$$

After calculation, we get,

$$\left\langle \hat{N} \right\rangle = \left\langle \hat{d}^{+}\hat{d} \right\rangle = \eta \left\langle n \right\rangle \tag{1.4.1.16}$$

where $\langle n \rangle = \left\langle \hat{c}_1^{+}\hat{c}_1 \right\rangle$

Similarly, the Variance is evaluated as ,

$$V(\hat{N}) = \eta^2 V(\hat{n}) + \eta(1-\eta)\left\langle n \right\rangle \tag{1.4.1.17}$$

Hence the uncertainty in the phase is given by,

$$\Delta\theta = \frac{\sqrt{V(N)}}{\left|\frac{\partial\langle N\rangle}{\partial\theta}\right|} \tag{1.4.1.18}$$

While when the squeezed state is injected, substituting equations (1.4.1.17) and (1.4.1.8). Hence this limit is given by [5]

$$\Delta\theta = \sqrt{\left[\frac{\eta e^{-2r} + (1-\eta)}{\eta\left\langle n \right\rangle}\right]\cos(\frac{\theta}{2}) + \frac{\sin^2(\frac{\theta}{2})}{\left\langle n \right\rangle \cos^2(\frac{\theta}{2})}} \tag{1.4.1.19}$$

and near to the dark fringe we get $\theta \approx 0$ we get

$$\Delta\theta = \sqrt{\frac{e^{-2r}}{\left\langle n \right\rangle} + \frac{1-\eta}{\eta\left\langle n \right\rangle}} \tag{1.4.1.20}$$

The classical limit is given by putting $\sinh^2 r = 0$ which gives us,

$$\Delta\theta = \frac{1}{\sqrt{\eta\left\langle n \right\rangle}} \tag{1.4.1.21}$$

When the squeezed light is injected referring to equation (1.4.1.20) the uncertainty is reduced by factor of e^{-r} for $r > 0$, considering an ideal situation when $\eta = 1$. However in realistic situations, loss term inside the square root of equation (1.4.1.20) often represents the practical limit to the reduction of the uncertainty. This principle to use squeezed vacuum to enhance precision beyond the limits of classical technology is currently used in gravitational wave observatories, and has already been demonstrated in many gravitational

wave detectors prototypes [38][39] and as well as LIGO, GEO 600[21][40]. The typical strain sensitivities of the gravitational wave detectors are in the order of $10^{-22}/\sqrt{Hz}$ around frequencies of 150 Hz [21]. It was reported, as shown in fig. 1.10, around 2.15 dB of squeezing was achieved in LIGO and around 2dB of in GEO 600 [21],[40].

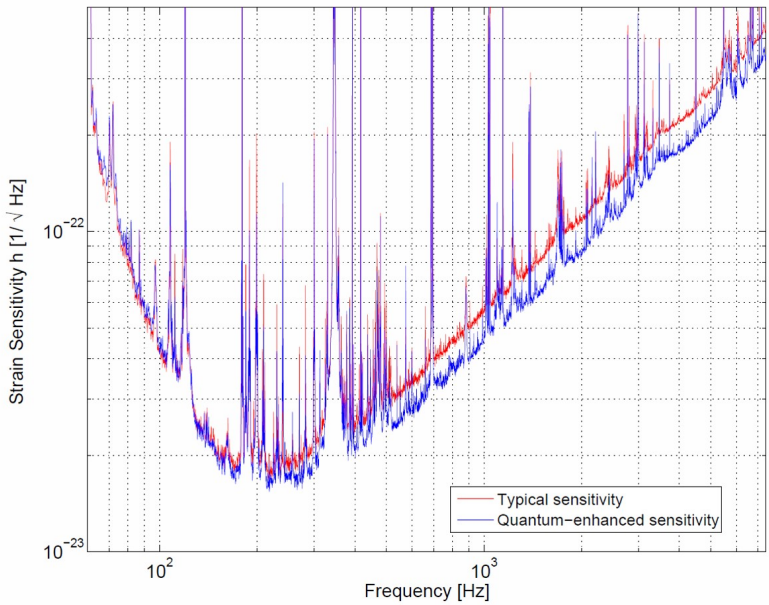

Figure 1.10: The plot shows the strain sensitivity obtained at LIGO[21]. Around 2.15dB of enhancement was observed when there was the injection of squeezed light into the interferometers.

1.4.2 Phase sensing with Balanced homodyne detection

In a balanced homodyne detection, the interferometer output is split on a beam splitter and interfered with a local oscillator of very high power compared to the output of the interferometer and subtraction between the two outputs is done as discussed in section 1.3.2.Figure 1.11 depicts the scheme of the homodyne. As demonstrated in the section 1.3.2 when we perform the expectation value of the photon number, it is proportional to the expectation value of quadrature and variance proportional to variance of the quadrature, we get similar results as in the case of looking at just the dark port of the interferometer. The balanced homodyne scheme has already been implemented in many gravitational wave detector prototypes [38] [39].

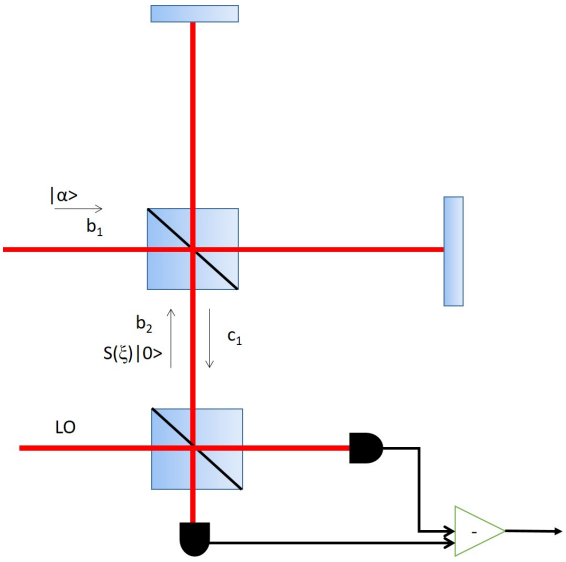

Figure 1.11: The figure above depicts the balanced homodyne scheme. The output of the interferometer at the dark port c_1 is interfered with a local oscillator. The coherent state is injected through port b_1 and the squeezed vacuum state is injected in port $\hat{b}_2$

1.5 Correlated Interferometers

We study in detail a system of two Michelson interferometers aimed at detecting extremely faint phase fluctuations. This system can represent a breakthrough for detecting a faint correlated signal that would remain otherwise undetectable even using the most sensitive individual interferometric devices. A faint correlated phase noise source acting in both the interferometers can emerge by performing the cross-correlation of their outputs whilst shot noise being uncorrelated in two interferometers. Given the advantages, this method has been the main principle in Fermilab holometer [27],[22],[25]. Even in this case injecting quantum light (Squeezed light/Twin-Beam state) in the system through their dark port of the interferometer can reduce the uncertainty in the measurement of phase correlation

1.5.1 Experimental Scheme

Let us consider two Michelson interferometers placed closed to each other with two equivalent coherent states $\left|\mu e^{i\phi}\right\rangle$ in b_k inputs of the interferometer. The quantum state $|\Psi\rangle$ (can be two independent squeezed states or two modes of the twin beam state) is injected from dark ports a_1 and a_2 of the interferometers. The fig. 1.12 depicts the experimental scheme. The observable covariance $\hat{C}(\phi_1, \phi_2)$ between the outputs of the interferometer is measured. Since we the phase fluctuations due to the holographic noise are expected to be extremely small, we can expand $\hat{C}(\phi_1, \phi_2)$ around the chosen central values $\phi_{1,0}$ and $\phi_{2,0}$ namely.

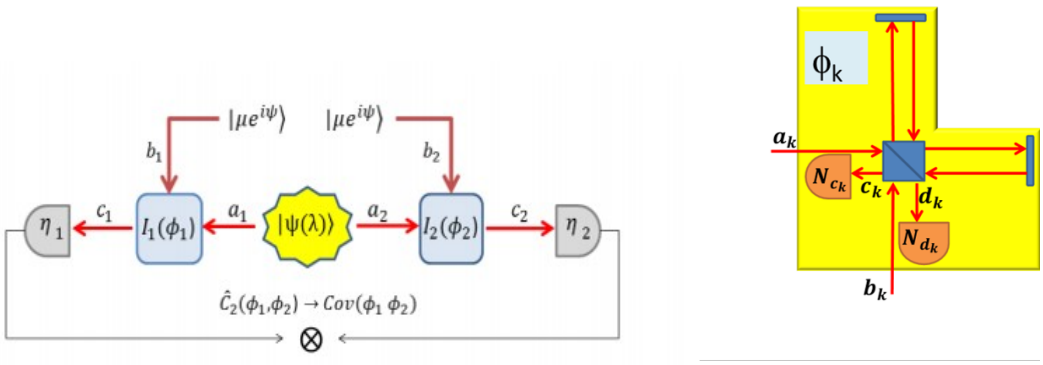

Figure 1.12: (i)The figure above represents the experimental scheme. Each interferometer is represented by I_k with coherent states injected in b_k and quantum states in a_k of the interferometers where k=1,2. (ii) The figure represents the Michelson interferometer with quantum light injected in port a_k.

Then the Taylor expansion gives us,

$$\hat{C}(\phi_1,\phi_2) = \hat{C}(\phi_{1,0},\phi_{2,0}) + \sum_i \partial_\phi \hat{C}(\phi_{1,0},\phi_{2,0})\delta\phi_i + \sum_i \partial^2_{(\phi_i,\phi_i)}\hat{C}(\phi_{1,0},\phi_{2,0})\delta\phi_i^2 + \sum_i \partial^2_{(\phi_1,\phi_2)}\hat{C}(\phi_{1,0},\phi_{2,0})\delta\phi_1\delta\phi_2 + \mathscr{O}(\delta\phi_i^3) \tag{1.5.1.1}$$

The Variance of the observable $\hat{C}(\phi_1,\phi_2)$ is given by ,

$$\mathrm{var}(\hat{C}(\phi_1,\phi_2)) = \mathrm{var}(\hat{C}(\phi_{1,0},\phi_{2,0})) + \sum_k A_{kk}\left\langle\delta\phi_k^2\right\rangle + A_{12}\left\langle\delta\phi_1\delta\phi_2\right\rangle + \mathrm{var}(\mathscr{O}(\delta\phi_i^3)) \tag{1.5.1.2}$$

where

$$A_{kk} = \left\langle \hat{C}(\phi_{1,0},\phi_{2,0})\partial^2_{(\phi_k,\phi_k)}\hat{C}(\phi_{1,0},\phi_{2,0})\right\rangle + \left\langle \partial_{\phi_k}\hat{C}(\phi_{1,0},\phi_{2,0})\right\rangle^2 - \left\langle \hat{C}(\phi_{1,0},\phi_{2,0})\right\rangle\left\langle \partial_(\phi_k,\phi_k)^2\hat{C}(\phi_{1,0},\phi_{2,0})\right\rangle \tag{1.5.1.3}$$

and

$$A_{12} = 2\left\langle \hat{C}(\phi_{1,0},\phi_{2,0})\partial^2_{(\phi_1,\phi_2)}\hat{C}(\phi_{1,0},\phi_{2,0})\right\rangle + 2\left\langle \partial_{\phi_1}\hat{C}(\phi_{1,0},\phi_{2,0})\partial_{\phi_2}\hat{C}(\phi_{1,0},\phi_{2,0})\right\rangle - \left\langle \hat{C}(\phi_{1,0},\phi_{2,0})\right\rangle\left\langle \partial_(\phi_1,\phi_2)^2\hat{C}(\phi_{1,0},\phi_{2,0})\right\rangle \tag{1.5.1.4}$$

Therefore the zero order uncertainty is given by [28],[29],

$$\mathscr{U}^{(0)}(\delta\phi_1\delta\phi_2) = \frac{\sqrt{2\mathrm{var}(\hat{C}(\phi_{1,0},\phi_{2,0}))}}{\left|\partial^2_{(\phi_1,\phi_2)}\hat{C}(\phi_{1,0},\phi_{2,0})\right|} \tag{1.5.1.5}$$

1.5.2 Independent Squeezed states

When independent squeezed states are injected into the interferometer, one can choose the operator $\hat{C}(\phi_1, \phi_2)$ given by the product of the photon number operators $\hat{N}_1\hat{N}_2$. However to remove the dc component, we evaluate

$$\hat{C}(\phi_1, \phi_2) = \left(\hat{N}_1 - \left\langle \hat{N}_1 \right\rangle\right)\left(\hat{N}_2 - \left\langle \hat{N}_2 \right\rangle\right). \tag{1.5.2.1}$$

Since both of them are independent we can evaluate variance of $C(\phi_1, \phi_2)$ as

$$\text{var}(\hat{C}(\phi_1, \phi_2)) = \left\langle \left(\hat{N}_1 - \left\langle \hat{N}_1 \right\rangle\right)^2 \right\rangle \left\langle \left(\hat{N}_2 - \left\langle \hat{N}_2 \right\rangle\right)^2 \right\rangle \tag{1.5.2.2}$$

which gives us

$$\text{var}(\hat{C}(\phi_1, \phi_2)) = \text{var}(\hat{N}_1)\text{var}(\hat{N}_2) \tag{1.5.2.3}$$

Hence the uncertainty using equation (1.5.1.5) can be written as,

$$\mathscr{U}^{(0)}(\delta\phi_1\delta\phi_2) = \frac{\sqrt{2\text{var}(\hat{N}_1)\text{var}(\hat{N}_2)}}{\left|\frac{\partial \text{var}(\hat{N}_1)}{\partial\phi_1}\frac{\partial \text{var}(\hat{N}_2)}{\partial\phi_2}\right|} = \sqrt{2\Delta\phi_{IFO_1}\Delta\phi_{IFO_2}} \tag{1.5.2.4}$$

where $\Delta\phi_{IFO_1}$ and $\Delta\phi_{IFO_2}$ are uncertainties in phases of interferometer 1 and 2. Let η_1 and η_2 be the inefficiency loss due to optics, μ and be the number of photons of the coherent state and r_1 and r_2 be the squeezing parameters of the squeezed states. Since we know from equation (1.4.1.19) and the uncertainty in phase for each interferometer, we can evaluate $\mathscr{U}^{(0)}(\delta\phi_1\delta\phi_2)_{sqz}$ as

$$\begin{aligned}\mathscr{U}^{(0)}(\delta\phi_1\delta\phi_2)_{sqz} = \left[\sqrt{2}\sqrt{\left[\frac{\eta_1 e^{-2r_1} + (1-\eta_1)}{\eta_1\mu}\right]\cos(\frac{\phi_1}{2}) + \frac{\sin^2(\frac{\phi_1}{2})}{\eta_1\mu\cos(\frac{\phi_1}{2})}}\right]\times \\ \left[\sqrt{\left[\frac{\eta_2 e^{-2r_2} + (1-\eta_2)}{\eta_2\mu}\right]\cos(\frac{\phi_2}{2}) + \frac{\sin^2(\frac{\phi_2}{2})}{\eta_2\mu\cos(\frac{\phi_2}{2})}}\right]\end{aligned} \tag{1.5.2.5}$$

Near to the dark fringe by putting condition $\phi_1 = \phi_2 \approx 0$, we get

$$\mathscr{U}^{(0)}(\delta\phi_1\delta\phi_2)_{sqz} = \sqrt{2\frac{e^{-2r_1}}{\mu} + \frac{(1-\eta_1)}{\eta_1\mu}}\sqrt{\frac{e^{-2r_2}}{\mu} + \frac{(1-\eta_2)}{\eta_2\mu}} \tag{1.5.2.6}$$

It can be seen that in ideal situations when losses are zero i.e. $\eta_1 = \eta_2 = 1$ we get $\mathscr{U}^{(0)}(\delta\phi_1\delta\phi_2)_{sqz} = \frac{\sqrt{2}e^{-r_1}e^{-r_2}}{\mu}$. This means the uncertainty is reduced by geometric mean of two squeezing factors.

For the classical case, i.e., when we consider λ_1=λ_2=0 (i.e. the mean number of photons of the squeezed state to be zero) and near to the dark fringe, the uncertainty reduction is

given by

$$\mathscr{U}^{(0)}(\delta\phi_1\delta\phi_2)_{classical} = \frac{\sqrt{2}}{\sqrt{\eta_1\eta_2}\mu} \tag{1.5.2.7}$$

Using equation (1.5.2.5) and mean number of photons of the squeezed light given by $\lambda = \sinh^2 r$, it can be shown that the uncertainty reduction with respect to classical light as function of phase ϕ (assuming both the interferometers are operated at same working point) and detection efficiencies $\eta_1 = \eta_2 = \eta$, is given by [28] [29],

$$\mathscr{R}^{(0)} = \frac{\mathscr{U}^{(0)}_{sqz}}{\mathscr{U}^{(0)}_{classical}} \approx 1 + \frac{\eta\cos\left(\frac{\phi}{2}\right)}{4\lambda} - \frac{\eta(1+\cos\left(\frac{\phi}{2}\right))}{2} \text{ (for } \lambda >> 1) \tag{1.5.2.8}$$

and similarly,

$$\mathscr{R}^{(0)} = \frac{\mathscr{U}^{(0)}_{sqz}}{\mathscr{U}^{(0)}_{classical}} \approx 1 - \eta(1+\cos(\phi))\sqrt{\lambda}(1-\sqrt{\lambda}) \text{ (for } \lambda << 1) \tag{1.5.2.9}$$

For the limit $\phi \approx 0$ in case of $\lambda >> 1$, we get,

$$\mathscr{R}^{(0)} = 1 - \eta + \frac{\eta}{4\lambda} \tag{1.5.2.10}$$

Dotted line in the fig. 1.13 represents the uncertainty reduction with respect to classical light $\mathscr{R}^{(0)}$, for high quantum efficiencies η of the photodetector and close to the dark fringe plotted as function of ϕ. It can be seen that for $\lambda >> 1$, the uncertainty reduction is flat, reaches a value of $1 - \eta + \frac{\eta}{4\lambda}$, for all the values of working phase near to the dark fringe.

1.5.3 Injection of Twin beam states

The twin beam states and its properties have been already discussed in subsection 1.3.3. This section discusses the effect of uncertainty reduction in correlated phase detection sensitivity when each mode of the twin beam state when injected into each interferometer. Since the twin beam state, at its outputs has perfect correlations in photon number, the general operator for the joint system of interferometers, $\hat{C}(\phi_1, \phi_2)$ operator unlike in the case of independent squeezers is chosen to be $(\hat{N}_1 - \hat{N}_2)^2$. The variance of the general operator $\hat{C}(\phi_1, \phi_2)$ can be calculated as $\text{var}(\hat{C}(\phi_1, \phi_2)) = \left\langle (\hat{N}_1 - \hat{N}_2)^4 \right\rangle - \left\langle \hat{N}_1 - \hat{N}_2 \right\rangle^4$.

The results of the theoretical uncertainty reduction in correlated phase detection calculated according to equation (1.5.1.5) are thoroughly discussed in [28],[29]. The solid lines represent the plot of uncertainty reduction as a function of working phase depicted in fig. 1.13 for the twin beam case. We get to see that, when each mode of the twin beam state is injected into the interferometers, the uncertainty reduction $\mathscr{R}^{(0)} = \frac{\mathscr{U}^{(0)}_{TWB}}{\mathscr{U}^{(0)}_{classical}}$ evaluated as a function of working phase ϕ, can be divided into two regimes: a) quadrature correlations regime and b) photon number entanglement regime. For higher efficiencies and as well as very close to the dark fringe when the classical field component is almost zero i.e $(1-T)\mu << T\lambda$ (where $T = \cos^2(\phi/2)$, transmission at the outputs of beam splitters of two interferometers), the photon number correlation from the injected twin beam state dominates, giving us a dramatic reduction in the uncertainty. While for

$T\lambda << (1-T)\mu$ and slightly away from dark fringe, quadrature correlations dominate and hence the uncertainty reduction behaves as same as for the case of independent squeezed states.

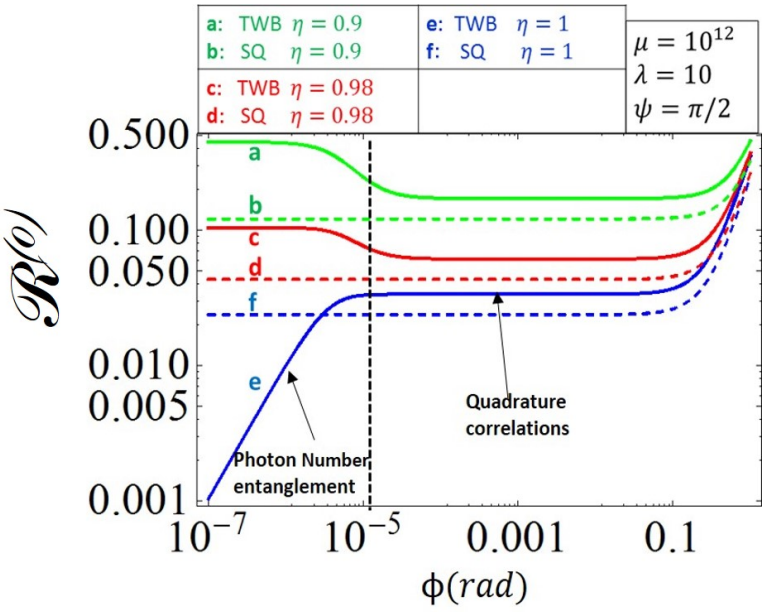

Figure 1.13: The figure above represents the uncertainty reduction (with respect to the classical uncertainty), $\mathscr{R}^{(0)}$ on the covariance sensitivity as function of the central working phase around $\phi_k = 0$ (near to the dark fringe), where k = 1, 2, in both cases of squeezed light injection and twin beam state injection. η is the overall detection probability, λ is the number of photon of the quantum light [28][29]. The Dotted lines represent the two independent squeezer case, where there is an extended range of value of the central working phase ϕ of the interferometers in which the uncertainty reduction achievable by adopting quantum light is stable. While in the twin beam case (given by solid lines), the results could be divide in two regimes the quadrature correlation regime and the photon number entanglement regime which are demarcated by the black dashed lines . It can be seen from the figure (for the curve e), that for higher detection efficiency η and working phase very close to zero where the classical component is almost zero ($T\lambda >> (1-T)\mu$) and the photon number correlation in the Twin Beam State dominates, it has an advantage in the uncertainty reduction. While for $T\lambda << (1-T)\mu$, where the classical signal dominates, it gives quadrature correlations and we have similar result as in independent squeezer case which is flat (apart a factor of $\sqrt{2}$).

However a twin beam like state which has the same non-classical behaviour can be generated by splitting a single mode squeezer on the beam splitter was used in the experiment. This state when injected into the double interferometers anti-correlations are observed as similar to the twin beam state as discussed in section 1.3.3.

1.6 Applications of Correlated phase interferometer

Optical interferometers have been the best tools used in sensing methodology fundamental detectors that have been used as gravitational wave detection [41], [20]. The recent detection of gravitational waves [20] demonstrated that a major improvement of the precision

of measuring devices can help unveil fundamental properties of nature. This improvement in precision can be obtained by injecting quantum states of light into the interferometer. In particular, this current experimental scheme is used to extract source of noises that have correlated phase fluctuations in two separated interferometers increasing the chance of distinguishing them with respect to other classical uncorrelated noises noise sources.

A double interferometer configuration is for instance the basis of the Fermilab holometer [27],[22],[25], a device consisting of two co-located 40 m Michelson interferometers. The purpose of the holometer is to search for a particular type of correlated background noise, conjectured in some heuristic Planck scale theories and dubbed holographic noise.

The experiment at Fermilab holometer is being done in two configurations. a) parallel configuration b) perpendicular configuration as shown in fig. 1.14.

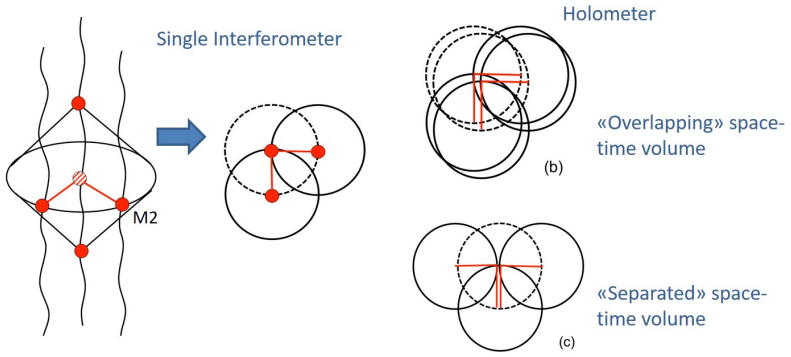

Figure 1.14: Model for probing Planckian scale effects using interferometers [22] a) Each interferometer is represented as a space-time volume b) The interferometer operated in parallel configuration. We evaluate cross correlation between two equal Michelson interferometers occupying the same space-time volume c) The interferometer operated in perpendicular configuration.Reference measurement: HN correlation cancels off by separating the space-time volumes of the two interferometers.

It has been argued that light, meanwhile propagating in the arms of an interferometer, would sum up incremental displacement at each discrete Planck interval step leading to a measurable effect when the interferometers are kept parallel to each other when the space-time volume overlap the interferometers while in the perpendicular case, the space time volume do not overlap and most of the noises are uncorrelated[25]. If holographic noise is confirmed, it would provide empirical support to theories attempting to unify quantum mechanics and gravitation. At the moment the holometer is operated with classical light only. The bandwidth of this noise depends on the arm length of interferometers. For length L, since the light travels 2L distance, the bandwidth of the noise is given by $c/2L$. (For Length=40m, the noise is expected to be present till the frequencies upto 3.75MHz range). z. The amplitude of the noise is predicted to be fixed by the Planck scale, with an expected value of about $\sqrt{l_p L}$, l_p being the planck length [42]. The first measurements of this double interferometer system was reported in [27]. Figure 1.15 shows that a strain sensitivity of around $10^{-21}/\sqrt{Hz}$ has been reached.

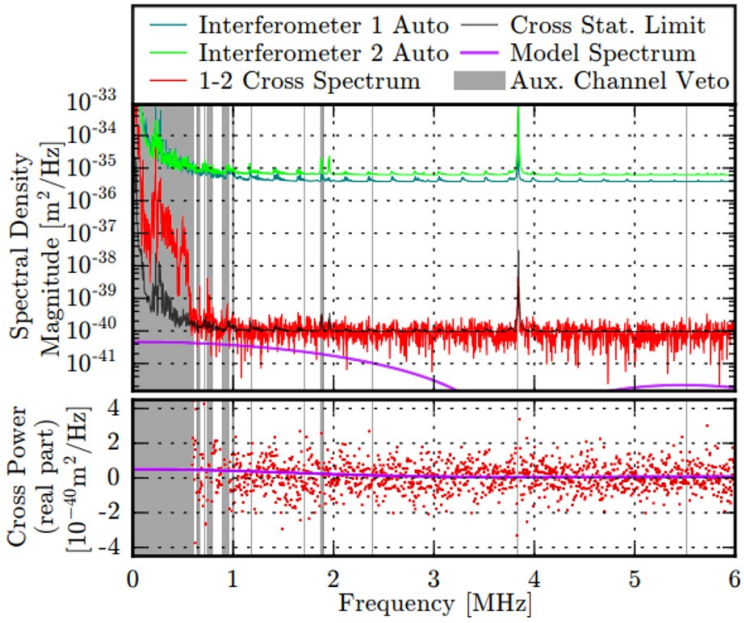

Figure 1.15: The first measurements of the Fermilab holometer [27].: With a 165 hours of measurement they where able to improve the sensitivity of several order of magnitude in the MHz regime, ruling out the presence of holographic noise up to $10^{-21}/\sqrt{Hz}$

This double interferometer system has been also been used for search of Stochastic gravitational wave background in MHz frequency regime at Fermilab holometer using the same experimental setup that could reveal information on the first few moments of the universe [26].

However, with quantum light injected into the double interferometer system, the sensitivity would further improve, as discussed in the theoretical analysis[28][29] described in the above section 1.5. The idea is to exploit properties of quantum light for both cases namely parallel and perpendicular configuration as shown in fig. 1.16. The quantum light when injected into the double interferometer system, in perpendicular configuration, would improve the sensitivity for detecting the uncorrelated noises in two interferometer system while in parallel configuration it improves the sensitivity for detection of correlated holographic noise.

With the twin beam light injection as we have discussed in fig. 1.13, if we operate working point of the michelson interferometer output very close to the dark fringe would give us a unprecedented correlated phase detected sensitivity. Although when we take the general operator $\hat{C}(\phi_1, \phi_2)$ as the difference in photon number leads to cancellation of the correlated noise if present, the covariance between the two interferometers could be extracted in the case of correlated holographic noise where the experiment is conducted in two configurations. Let us re-consider the equation (1.5.1.1) and take expectation value of it.

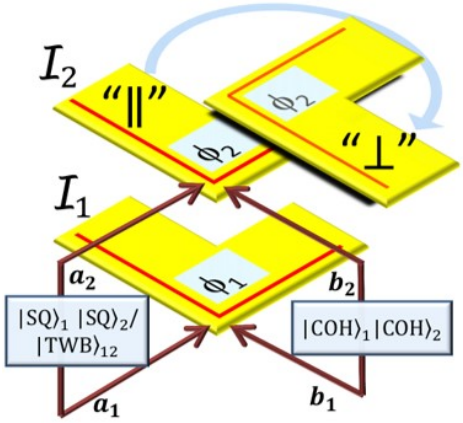

Figure 1.16: The figure is taken from [28][29]. Two measurement configurations with injected quantum light in two interferometers, namely, one in $\|^{el}$ and one in $\perp^{r}$ suggested in order to detect the holographic noise

$$\left\langle \hat{C}(\phi_1,\phi_2)\right\rangle = \left\langle \hat{C}(\phi_{1,0},\phi_{2,0})\right\rangle + \sum_i \partial_{\phi_i}\left\langle \hat{C}(\phi_{1,0},\phi_{2,0})\right\rangle \langle\delta\phi_i\rangle$$
$$+\sum_i \partial^2_{(\phi_i,\phi_i)}\left\langle \hat{C}(\phi_{1,0},\phi_{2,0})\right\rangle \langle\delta\phi_i^2\rangle + \sum_i \partial^2_{(\phi_1,\phi_2)}\left\langle \hat{C}(\phi_{1,0},\phi_{2,0})\right\rangle \langle\delta\phi_1\delta\phi_2\rangle + \mathscr{O}(\delta\phi_i^3) \tag{1.6.0.1}$$

Since $\langle\delta\phi_i\rangle = 0$ we can write

$$\left\langle \hat{C}(\phi_1,\phi_2)\right\rangle = \left\langle \hat{C}(\phi_{1,0},\phi_{2,0})\right\rangle + \sum_i \partial^2_{(\phi_i,\phi_i)}\left\langle \hat{C}(\phi_{1,0},\phi_{2,0})\right\rangle \langle\delta\phi_i^2\rangle$$
$$+\sum_i \partial^2_{(\phi_1,\phi_2)}\left\langle \hat{C}(\phi_{1,0},\phi_{2,0})\right\rangle \langle\delta\phi_1\delta\phi_2\rangle + \mathscr{O}(\delta\phi_i^3) \tag{1.6.0.2}$$

The term $\langle\delta\phi_1\delta\phi_2\rangle$ gives the covariance. Hence for the holographic noise we consider two cases parallel and perpendicular. The perpendicular configuration as mentioned is taken as a reference measurement for which covariance is zero since the noises are uncorrelated due to non overlapping of space-time volume between the interferometers while the parallel case gives us the non-zero covariance since equal Michelson interferometers occupy the same space-time volume.

Hence we can extract the covariance as

$$\langle\delta\phi_1\delta\phi_2\rangle = \frac{\left\langle \hat{C}(\phi_1,\phi_2)\right\rangle|_{\|} - \left\langle \hat{C}(\phi_1,\phi_2)\right\rangle|_{\perp}}{\frac{\partial^2\left\langle \hat{C}(\phi_1,\phi_2)\right\rangle_{\|}}{\partial\phi_1\partial\phi_2}} \tag{1.6.0.3}$$

where $\hat{C}(\phi_1,\phi_2) = (N_1 - N_2)^2$ for twin beam case. Hence we can write the above equation as

$$\langle\delta\phi_1\delta\phi_2\rangle = \frac{\mathrm{var}(N_1-N_2)|_{\|} - \mathrm{var}(N_1-N_2)|_{\perp}}{\frac{\partial^2\left\langle \hat{C}(\phi_1,\phi_2)\right\rangle|_{\|}}{\partial\phi_1\partial\phi_2}} \tag{1.6.0.4}$$

Hence the uncertainty in covariance of phase fluctuations can be calculated as

$$\mathscr{U}^{(0)}(\delta\phi_1\delta\phi_2) = \frac{\sqrt{\mathrm{var}(\hat{C}(\phi_1,\phi_2))|_{\parallel} + \mathrm{var}(\hat{C}(\phi_1,\phi_2))|_{\perp}}}{\frac{\partial^2 \langle \hat{C}(\phi_1,\phi_2)\rangle_{\parallel}}{\partial\phi_1\partial\phi_2}} \tag{1.6.0.5}$$

When we inject two independent squeezed states, to extract the covariance of the signal we can reconsider equation (1.6.0.3) and use the $\hat{C}(\phi_1,\phi_2) = \hat{N}_1\hat{N}_2$. The uncorrelated shot noise in two interferometers reduces by the geometric mean of two individual squeezing factors given by $e^{-r_1}e^{-r_2}$ of the the two independent squeezed states used in ideal conditions of no losses in the detection efficiency.

In Chapter 5 and Chapter 6, we discuss how we have experimentally demonstrated the uncertainty reduction for the double interferometer scheme by injecting quantum light (both twin beam light as well as squeezed light).

1.7 Conclusion

We have done a rigorous description quantum states and its properties. Various limits on the phase sensitivity were described in this chapter. The effects of uncertainty reduction when the quantum states are injected into a single interferometer have been discussed. The experimental scheme has been described and the consequences of reduction of uncertainty in correlated phase sensitivity detection when quantum states have been injected are discussed. The application of this current double interferometer scheme to the Fermilab holometer and search for stochastic gravitational wave background have been explained.

CHAPTER 2

BASICS OF POWER RECYCLING INTERFEROMETERS

2.1 Introduction

As we have discussed in section 1.5, to extract source of noises that have correlated phase fluctuations, we have to consider the "holometer scheme" i.e two interferometers to be setup close and parallel to each other. For this purpose, we need to consider specific type of Michelson interferometers namely *Power Recycling Michelson interferometers*. These are the types of interferometer currently operated at large scale gravitational-wave detectors. They are based on the combination of two fundamental interferometers : the Fabry-Pérot interferometer and the Michelson interferometer[43].

In this chapter, I discuss in depth, both the properties of Fabry-Pérot cavities and Michelson interferometer and the locking techniques involved to stabilize them. I will then, introduce the concept of power recycling interferometers and describe their properties.

2.2 Fabry-Pérot cavity

A Fabry-Pérot cavity is a linear cavity formed by two partially reflecting mirrors as depicted in fig. 2.1. When light is incident on this linear cavity, some part is transmitted and some part is reflected. The beam is transmitted through the cavity only when the length of the cavity L matches the multiples of wavelength λ of the incident light. Consider the Fabry-Pérot Cavity in fig. 2.1. E_{cav} represents the intra-cavity electric field inside the cavity, E_i represent the incident electric field and E_{ref} the reflected field from the cavity. Let r_1 and r_2 be the reflectivities of the two mirrors and t_1, t_2 are the transmitivities.

Under steady state conditions, when the light has made a complete round trip, the intra-cavity field can be written as

$$E_{cav} = E_i t_1 + E_{cav} * r_1 r_2 e^{2ikL} \tag{2.2.0.1}$$

where $k = \frac{2\pi}{\lambda}$, λ being the wavelength,

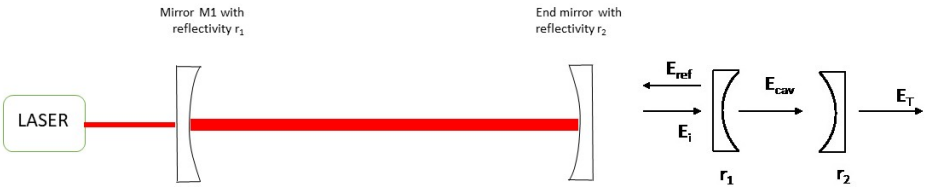

Figure 2.1: Fabry-Pérot Cavity: E_{ref}, E_{cav} and E_T are electric fields of reflection, cavity, and transmission

which gives:

$$E_{cav} = E_i \frac{t_1}{1 - r_1 r_2 e^{2ikL}} \tag{2.2.0.2}$$

Similarly $E_{ref} = -r_1 E_i + t_1 r_2 E_{cav}$ leading to,

$$E_{ref} = -E_i \left(\frac{-r_1 + (r_1^2 + t_1^2) r_2 e^{2ikL}}{1 - r_1 r_2 e^{2ikL}}\right) \tag{2.2.0.3}$$

The transmission of the field is given by, $E_T = t_2 * E_{cav}$

$$E_T = t_2 E_i \frac{t_1}{1 - r_1 r_2 e^{2ikL}} \tag{2.2.0.4}$$

From equation (2.2.0.4) we obtain the Intensity I_T measured on the photodetector as:

$$I_T = E_T^* E_T = |E_T|^2 = \frac{I_0 |t_1|^2 |t_2|^2}{|1 - r_1 r_2 e^{2ikL}|^2}, \tag{2.2.0.5}$$

where $I_0 = |E_i|^2$. We get from above equation (2.2.0.5)

$$I_T = \frac{I_0 |t_1|^2 |t_2|^2}{1 + \rho^2 - 2\rho \cos(\phi)} = \frac{I_0 |t_1|^2 |t_2|^2}{1 + [4\frac{\rho}{(1-\rho)^2}] \sin^2(\phi/2)} \tag{2.2.0.6}$$

where $\rho = r_1 r_2$ and $\phi = 2kL$

$$I_T = \frac{I_0 |t_1|^2 |t_2|^2}{(1-\rho)^2} \left(\frac{1}{1 + M \sin^2(\phi/2)}\right) \tag{2.2.0.7}$$

where $M = \frac{4\rho}{(1-\rho)^2}$. The above form of I_T in equation (2.2.0.7) is an Airy function.The figure 2.2 plots the transmitted intensity as function of detuning of frequency.

Writing equation (2.2.0.3) as a function of frequency, and assuming, no input loss from the first mirror, i.e. $r_1^2 + t_1^2 = 1$, we can write

$$E_{ref}(\omega) = -E_i(\omega) \left(\frac{-r_1 + r_2 e^{i\frac{2\omega L}{c}}}{1 - r_1 r_2 e^{i\frac{2\omega L}{c}}}\right) \tag{2.2.0.8}$$

From the equation (2.2.0.7), it can be seen that the transmission in the cavity is maximum when phase $\phi = 2kL$ is multiple of 2π which implies, whenever the detuning frequency ν is a multiple of $\frac{c}{2L}$, the transmission of the cavity is maximum. This spacing of the detuning between two successive maximas or two successive minimas of the

transmission of the cavity $\Delta\nu = \frac{c}{2L}$ is called *Free Spectral Range*.

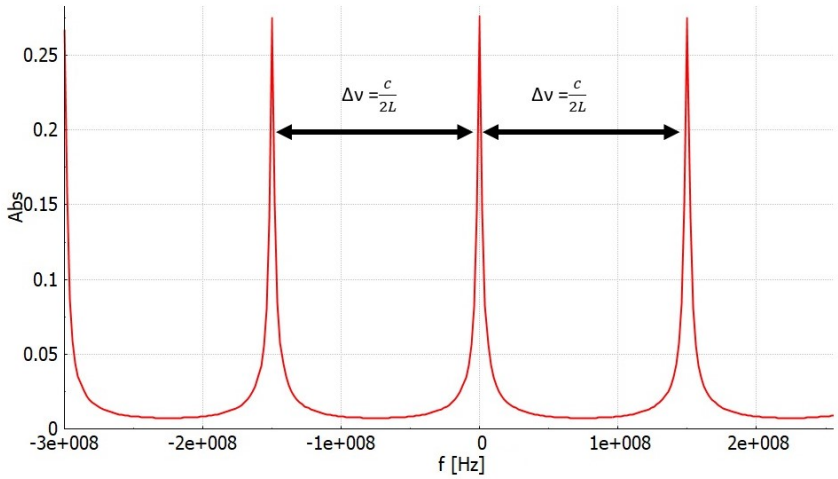

Figure 2.2: Fabry-Pérot cavity: the transmitted intensity as a function of detuning with respect to the frequency of the input field. Here in this simulation, length of the cavity considered was 1m. Hence the spacing betweeen two modes would be around 150 MHz which is the free spectral range.

Another property, which defines the losses in the cavity, is finesse. It is defined as the ratio of Free Spectral Range (FSR) of the cavity to the full-Width-at-half-maximum (FWHM) of the transmitted peak. It defines the quality of the cavity.

From the Airy function properties, the full linewidth can be written as [44]:

$$FWHM = \frac{c}{\pi L}(\sin^{-1}(\frac{1 - r_1 r_2}{2\sqrt{r_1 r_2}})) \tag{2.2.0.9}$$

The Finesse is hence given by

$$\mathscr{F} = \frac{FSR}{FWHM} = \frac{\pi}{2\sin^{-1}(\frac{1-r_1 r_2}{2\sqrt{r_1 r_2}})} \tag{2.2.0.10}$$

The Finesse of the cavity in general is used as a parameter to estimate the round trip losses in the cavity. The higher is the finesse, the lower are the round trip losses.

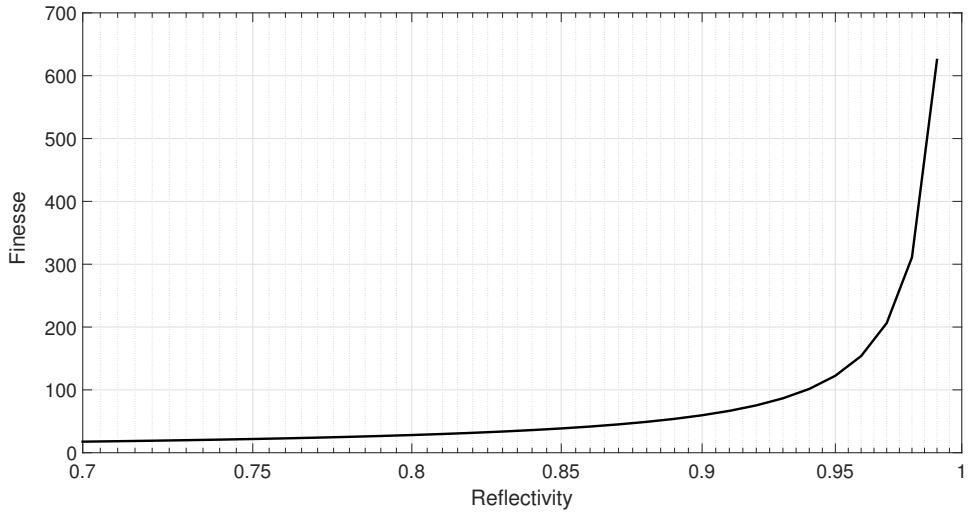

Figure 2.3: Fabry-Pérot cavity: the Finesse of the cavity is plotted as a function of reflectivity of the cavity.

2.2.1 Pound-Drever-Hall locking

The reflection coefficient is defined as, $F(\omega) = \frac{E_{ref}(\omega)}{E_i(\omega)}$. Hence

$$F(\omega) = \left(\frac{-r_1 + r_2 e^{i\frac{\omega 2L}{c}}}{1 - r_1 r_2 e^{i\frac{\omega 2L}{c}}}\right) \tag{2.2.1.1}$$

The beam reflected from the first mirror has two components: a) the reflected part of the incident beam and b) the leakage of the intra-cavity. These two beams have the same frequency, and near resonance their intensities are almost the same. Their relative phase, however, depends strongly on the frequency of the laser beam.

The cavity is said to be on resonance when the reflected beam and the leakage beams have the same amplitude and are exactly out of phase by π, while when the cavity is not perfectly resonant, the two beams will not perfectly cancel out and there would be some light out from the reflected side.

To lock the cavity to the resonance, a locking technique using the reflection of the cavity called Pound-Drever-Hall Technique is utilized[45]. Applying a periodic electronic signal to electro-optic-modulator, it induces a periodic phase modulation of the laser beam. The primary result of this phase modulation is to impose new optical fields separated in frequency from the original field by the RF modulation frequency. These new fields are usually referred to as phase modulated *sidebands*, while the central frequency component is called the *carrier*.

Concept: Consider the fig. 2.4: Let us consider that the incident carriers electric field component always lies along the real axis. The part of the carrier that gets reflected from the Fabry-Pérot cavity is also represented by a vector in this plane. The upper sideband $(\omega + \Omega)$ has a higher frequency than the carrier, so its vector rotates counterclockwise in the plane with angular frequency Ω. The lower sideband $(\omega - \Omega)$ has a lower frequency and rotates clockwise at -Ω. The sum of the two sidebands, when they are both completely

reflected off the cavity, is a single vector that oscillates at frequency 2Ω up and down along the imaginary axis. While the interference between reflected carrier and the sideband gives a Ω term.

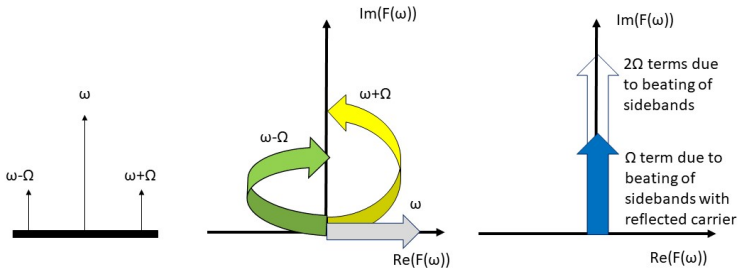

Figure 2.4: Pound-Drever-Hall [left to right]: the first figure shows the sidebands and carrier in the frequency domain. The second figure shows the rotation of the sidebands with angular frequency $(\omega \pm \Omega)$ along the complex plane. The third figure show the resulting of sidebands beating with carrier and sidebands itself

Derivation of Error Signal

Transmitting the beam through the electro optic modulator (EOM) , its electric field becomes

$$E_{inc} = E_0 e^{i(\omega t + \beta \sin(\Omega t))} \tag{2.2.1.2}$$

We can expand this expression using Bessel functions:

$$E_{inc} = E_0[J_0(\beta) + 2iJ_1(\beta)\sin(\Omega t)]e^{i\omega t} \tag{2.2.1.3}$$

where Ω is phase modulation frequency and β is modulation depth.
The reflected electric field is given by:

$$E_{ref} = E_0[F(\omega)J_0(\beta)e^{i\omega t} + J_1(\beta)F(\omega+\Omega)e^{i(\omega+\Omega)t} - J_1(\beta)F(\omega-\Omega)e^{i(\omega-\Omega)t}] \tag{2.2.1.4}$$

Then the power measured on the reflected on the photo detector is given by

$$P_{ref} = |E_{ref}|^2 = P_c|F(\omega)|^2 + P_s(|F(\omega+\Omega)|^2 + |F(\omega-\Omega)|^2) + 2\sqrt{P_c P_s}(\mathrm{Re}[F(\omega)F^*(\Omega+\omega) - F^*(\omega)F(\omega-\Omega)]cos(\Omega t) + \mathrm{Im}[F(\omega)F^*(\Omega+\omega) - F^*(\omega)F(\omega-\Omega)]\sin(\Omega t)) + (2\Omega \text{ terms}) \tag{2.2.1.5}$$

where $P_c = J_0^2(\beta)P_0$ and $P_s = J_1^2(\beta)P_0$ and $P_0 = |E_0|^2$

The cross term proportional to $\sin(\Omega t)$ represents the beating of the sidebands with the reflected carrier. The 2Ω term is the result of the two sidebands beating together as discussed in fig. 2.4. A mixer as depicted in fig. 2.5 (i) demodulates the signal at frequency Ω , for which the error signal obtained is then given by

$$\epsilon = 2\sqrt{P_c P_s}[\mathrm{Im}[F(\omega)F^*(\Omega+\omega) - F^*(\omega)F(\omega-\Omega)]] \tag{2.2.1.6}$$

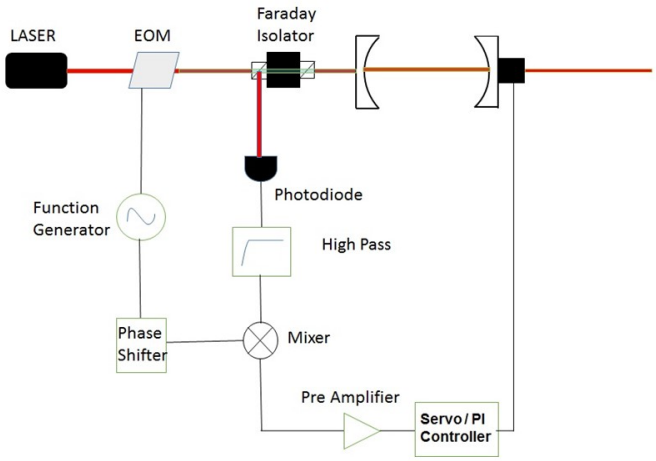

(i)

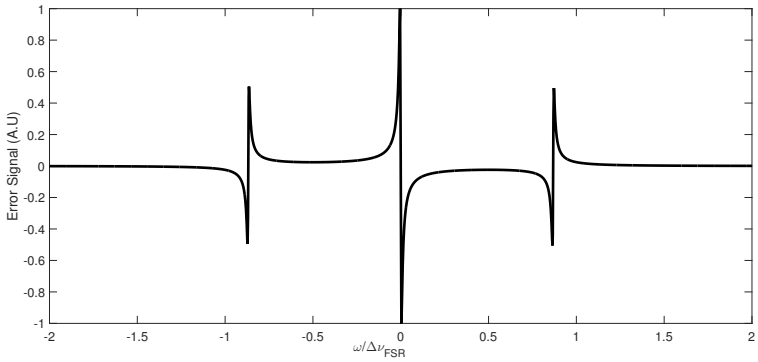

(ii)

Figure 2.5: (ii) The Feedback Experimental scheme. The EOM produces sidebands and the error signal is generated by demodulating the reflection signal and (ii)The Pound-Drever-Hall error signal of the cavity

It is important to note that the error signal crosses zero when the cavity is on resonance as shown in fig. 2.5 (ii). In practice, the phase between the local oscillator and photodiode output should be properly adjusted such that the slope of the error signal is maximized. This error signal, is sent to the piezo actuator via the feedback for locking the cavity to resonance as shown in fig. 2.5 (i).

2.2.2 Impedance matching

The reflection coefficient helps in defining the types of cavities. The fig. 2.6 categorizes the types of cavities based on the reflectivities of the mirrors. The leakage beam is generally π out of phase with the promptly reflected beam on resonance, so the interference between the two is destructive. This leakage beam properties depend on the reflectivities of the two

mirrors. Consider the equation (2.2.1.1), for $r_1 = r_2$ i.e if the leakage beam exactly cancels the reflected beam , then the cavity is said to be impedance matched or critically coupled. If the leakage beam is too weak to entirely cancel the reflected beam i.e for $r_2 < r_1$, the cavity is called under coupled. If the leakage beam is much stronger than the reflected beam i.e $r_2 > r_1$, the cavity is said to be overcoupled. For instance, in LIGO, overcoupled cavities are used, which allows having the reflected beam from the Fabry-Pérot cavities when they are on resonance [45].

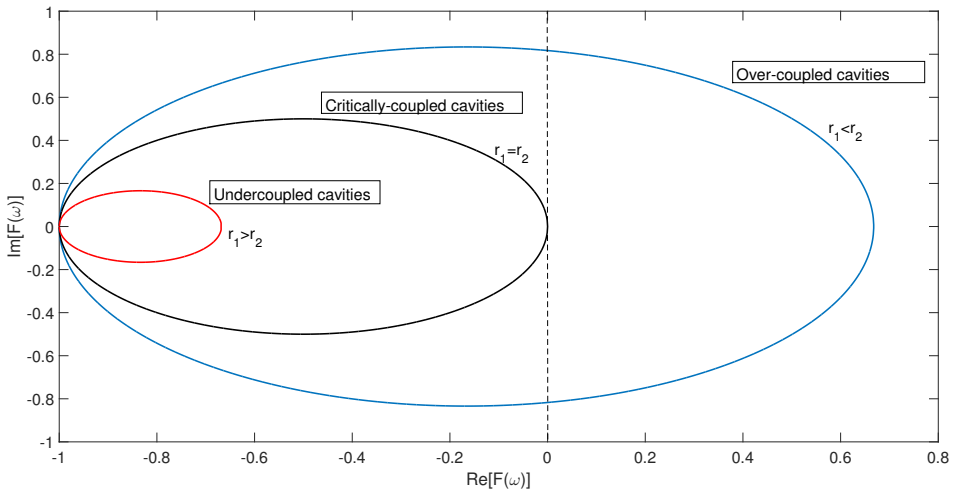

Figure 2.6: Types of the cavities depending on the reflectivities of two mirrors

2.2.3 Modematching

The higher order modes would be enhanced if the laser input TEM_{00} mode is not mode matched to that of the cavity mode. Proper lenses must usually be used to shape the incoming beam. The size and shape of the output mode of the Fabry-Pérot cavities are determined by two factors: a) the curvature of the partially reflecting mirror b) the curvature of the highly reflecting end mirrors.

If input mirror and end mirror have the same radius of curvature, the beam waist should be exactly in the middle of the length L of the cavity, i.e at $\frac{L}{2}$. This is because the radius of the Gaussian beam should effectively match the radius the partially transmitting mirror as well as radius of curvature of the highly reflecting end mirror.

If we have one partially reflecting end mirror having some radius of curvature and the highly reflecting end mirror being plane, then the condition should be that the beam waist is at the end mirror, since the radius of curvature for a plane mirror is ∞.

Here we examine the latter case as it represents our system. The lenses should be arranged such that, a) the Gaussian beam entering the cavity should have the equal radius as the radius of curvature of the partially reflecting mirror. b) the waist should be at the end mirror.

Let us consider the fig. 2.7:

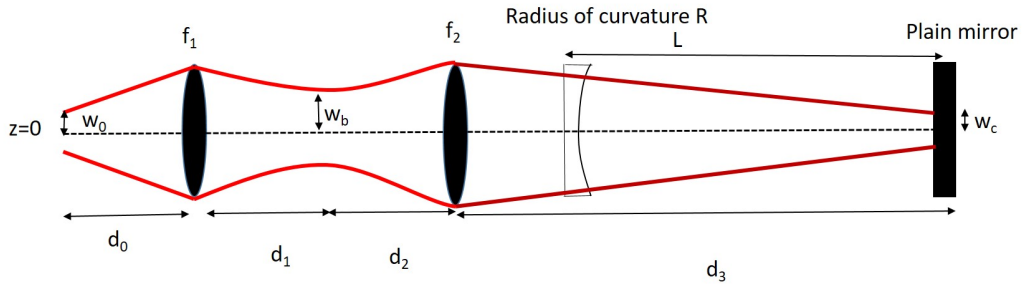

Figure 2.7: Lenses with focal lengths f_1 and f_2 are placed to mode match the input beam to the cavity.

Let *R (z)* represent the radius of curvature of the Gaussian beam and r represent the radius of curvature of the partially reflecting mirror,let w_c be the waist at the end of the plane mirror in fig. 2.7 to be matched and w_0 be the waist of the input beam.

The radius of the Gaussian beam as a function of distance z is given by[27]

$$R(z) = z + \frac{z_0^2}{z} \tag{2.2.3.1}$$

where $z_0 = \frac{kw_0^2}{2}$ [46] is called as Rayleigh range. The mode matching conditions are hence accordingly: (a) $R(L) = r$ and (b) The waist w_c should be at the end mirror.

Hence we can write, $L + \frac{z_0^2}{L} = r$, where z_0 is the Rayleigh range which could be written for waist w_c as,

$$z_0 = \frac{kw_c^2}{2} \tag{2.2.3.2}$$

Solving it for w_c,

$$w_c = (\frac{4L(r-L)}{k^2})^{1/4} \tag{2.2.3.3}$$

A ray tracing technique called Ray transfer matrix is used for calculating the lenses required for the mode-matching. A ray transfer matrix $\begin{bmatrix} A & B \\ C & D \end{bmatrix}$ is used to characterize the optic element it has gone through from input plane to output plane (Detail description of Ray matrices can be found in Appendix A).

Solving using Ray transfer matrix method described in Appendix A we can solve for d_1, w_b, d_2, d_3 and w_c

$$d_1 = \frac{f_1\pi^2 w_0^4 + d_0^2\lambda^2 - d_0 f_1 \lambda^2}{(f_1\pi^2 w_0^4 + d_0^2\lambda^2 - 2d_0 f_1\lambda^2 + f_1^2\lambda^2)^{1/2}} \tag{2.2.3.4}$$

$$w_b = \frac{f_1 w_0 \lambda}{(f_1\pi^2 w_0^4 + d_0^2\lambda^2 - 2d_0 f_1\lambda^2 + f_1^2\lambda^2)^{1/2}} \tag{2.2.3.5}$$

$$d_2 = f_2 + (\frac{f_2^2 w_b^2 \lambda^2}{w_c^2} - \pi^2 w_b^4)^{1/2}\lambda \tag{2.2.3.6}$$

$$d_3 = \frac{f_2\pi^2 w_b^4 + d_2^2\lambda^2 - d_2 f_2 \lambda^2}{(f_2\pi^2 w_b^4 + d_2^2\lambda^2 - 2d_2 f_2\lambda^2 + f_2^2\lambda^2)^{1/2}} \tag{2.2.3.7}$$

$$w_c = \frac{f_2 w_b \lambda}{(f_2 \pi^2 w_b^4 + d_2^2 \lambda^2 - 2 d_2 f_2 \lambda^2 + f_2^2 \lambda^2)^{1/2}} \tag{2.2.3.8}$$

In general, if we know the radius of curvatures of the mirror r and length of the cavity, we could evaluate the waist w_c. If we have a fixed initial waist w_0,choosing the right lenses of focal length f_1 and f_2, the distances d_1, d_2 and d_3 in fig. 2.7 could be evaluated.

Stability of Cavities

Consider a cavity of length L formed by Radius of curvatures of two mirrors R_1 and R_2. In general, few range of values of L, R_1, R_2 allows an optical cavity to be stable. This could be evaluated using Transfer matrix formalism[45]. The stability condition is given by $0 < g_1 g_2 < 1$, where $g_1 = 1 - L/R_1$ and $g_2 = 1 - L/R_2$[45]. Figure 2.8 represents the stability curve of the cavities. Areas bounded by the line $g_1 g_2 = 1$ and the axes are considered to be stable. Cavities at points exactly on the line are marginally stable. Depending on this we could choose appropriate radius of curvature of the mirrors and length for the cavity for the cavity to be stable.

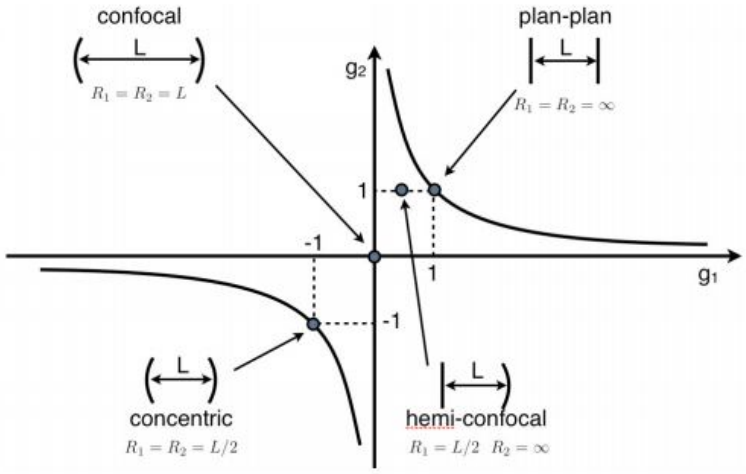

Figure 2.8: Graphical representation of the stability of a cavity

2.3 Michelson Interferometer

The detection of very weak phase noises requires performing high sensitivity measurements. As a first instance of interferometric scheme let us consider the Michelson interferometer. A Michelson interferometer consists of a 50/50 beam splitter and two piezo transducer driven end mirrors (PZT). The laser field propagates down each arm of the interferometer, before reflecting back towards the beam splitter as shown in fig. 2.9. The two beams then interfere at the beam splitter and the intensity of the transmission and reflection depends on differential arm length (DARM) $(L_1 - L_2)$ and can be sensed by using a photodetector at the output of the interferometer.

The power at the anti-symmetric port P_{AS} is given by [47] :

$$P_{AS} = P_{BS}[(\frac{r_1 + r_2}{2})^2 \sin^2(\frac{2\pi\Delta X}{\lambda}) + (\frac{r_1 - r_2}{2})^2 \cos^2(\frac{2\pi\Delta X}{\lambda})] \tag{2.3.0.1}$$

where r_1 and r_2 are the reflectivities of the end mirrors in the interferometer and $\Delta X = (L_1 - L_2)$, as the light experiences twice the path difference and P_{BS} is the power incident on the beam splitter.

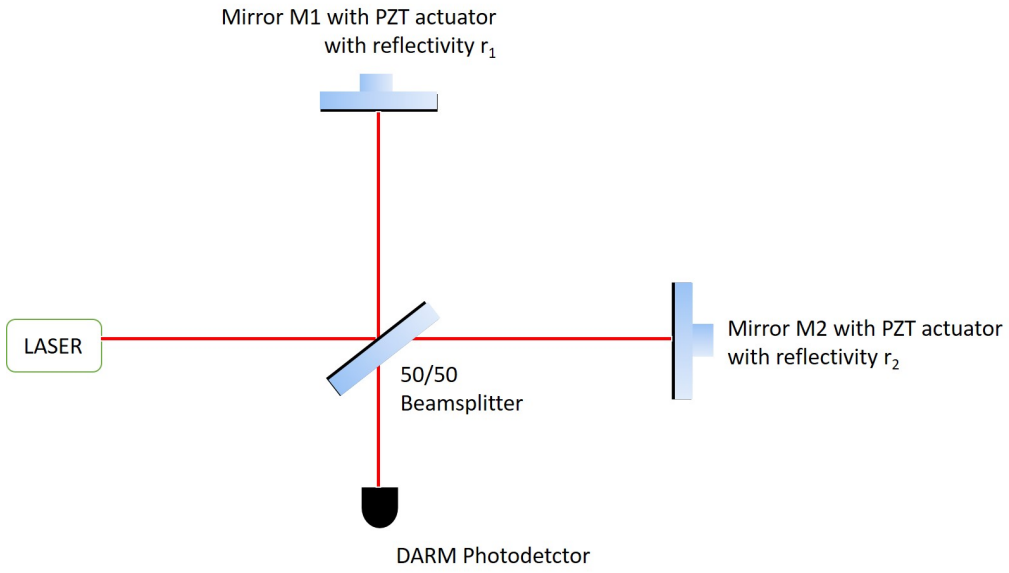

Figure 2.9: Scheme of Michelson Interferometer

The photodiode output corresponding to constructive interference is called bright fringe and destructive interference is called dark fringe. It can be obtained from equation (2.3.0.1) that the difference between displacement corresponding to maxima and displacement corresponding to minima of the fringe is $\lambda/4$ as shown in figure fig. 2.10.

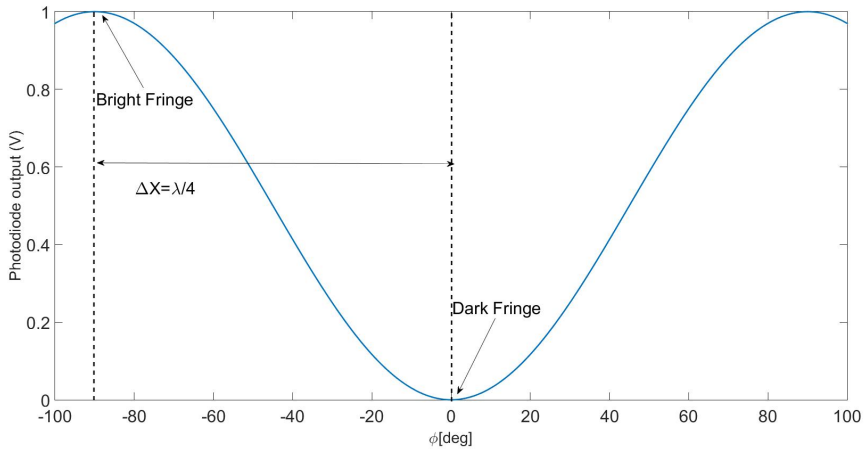

Figure 2.10: The figure above plots the photodetector output as a function of phase of the end mirrors under ideal conditions when there are no losses present,

2.3.1 Visibility

The figure of merit to quantify the contrast between the dark and bright fringe the interferometric visibility is given by:

$$V = \frac{(P_{max} - P_{min})}{(P_{max} + P_{min})} \tag{2.3.1.1}$$

When the splitting ratio is unequal, the normalized visibility is given by,

$$V' = V/v \tag{2.3.1.2}$$

where,

$$v = \frac{2\sqrt{(P_1 P_2)}}{(P_1 + P_2)} \tag{2.3.1.3}$$

and P_1, P_2 are the optical powers in each branch of interferometer.

2.3.2 Locking of the DARM

The PZT driving the end mirrors are used to stabilize the interferometer near a certain point on the fringe through a feedback system with a servo/ controller (usually a proportional- integral controller). The feedback system consists of control unit (PI controller),the detector and PZT attached mirrors. The detector produces the error signal for locking the point of the fringe. We set a value to be locked , the PI controller processes the value. The error in the value (ES) is given by:

$$ES = \text{Processed value} - \text{Set value} \tag{2.3.2.1}$$

The feedback loop tries to compensate fluctuations until it reaches the set value. However, there are different types of techniques used for locking. Some of the techniques used to lock the DARM are described in the following sections.

DC Locking

In the DC locking, the error signal is the direct DC output at the DARM photodetector. The error signal obtained from the Michelson interferometer from the photodetector is directly sent to the PZT actuators. The error signal is sent differentially (i.e by a phase of π) to both the end mirrors inducing a path difference of 2ΔL ($\Delta L = L_1 - L_2$). However the drawback of this locking technique when one is interested in locking near to the dark fringe, small fluctuations could disturb the stability of the lock.

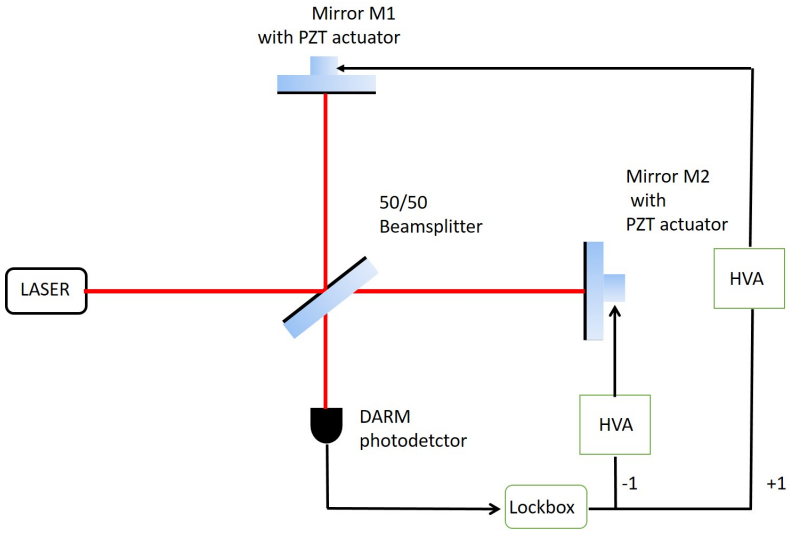

Figure 2.11: DC locking technique: here the photodiode output is directly used as error signal to be fed-back to the mirrors.

Dither Locking

A small sinusoidal modulation at audio frequency is injected to the piezos to tune the length of the interferometer, and the output (i.e. transmitted light intensity) is demodulated by a mixer at the same frequency, producing an error signal.Figure 2.12 (ii) shows the phase-flip that occurs as the system moves through the quadratic point. At the quadratic point, the error signal is zero,while on either side it attains nonzero values with opposite signs.

In this locking technique, the two end mirrors are dithered differentially (by a phase of of π with respect to each other) at frequency ω such that phase of the interferometer is $\phi(t) = \phi_0 + A\sin(\omega t)$ Hence the power fluctuations on the Photodiode using the Taylor expansion can be written as

$$P_{AS}(\phi(t)) = P_{AS}(\phi_0) + P'_{AS}(\phi(t)) * A\,\omega\,t\cos(\omega t) + 2\omega t \ \text{ terms} + \text{Higher order terms}. \tag{2.3.2.2}$$

The error signal of the interferometer is obtained by demodulating down with frequency of ω and results to be proportional to the derivative of the power P_{AS} with respect to the phase shift ϕ. Hence from equation (2.3.0.1) we can evaluate the derivative as

$$P'_{AS}(\phi(t)) = P_{BS}[\sqrt{r_1 r_2}]sin(2\phi(t)), \tag{2.3.2.3}$$

where $\phi(t) = \frac{2\pi\Delta X(t)}{\lambda}$

The error signal is then demodulated by a mixer at the same frequency of ω and further low passed. Hence the error signal we obtain is the first derivative of the power at the anti-symmetric port. With this technique, the dark fringe on the DC readout corresponds to the maximum slope point on the error signal.

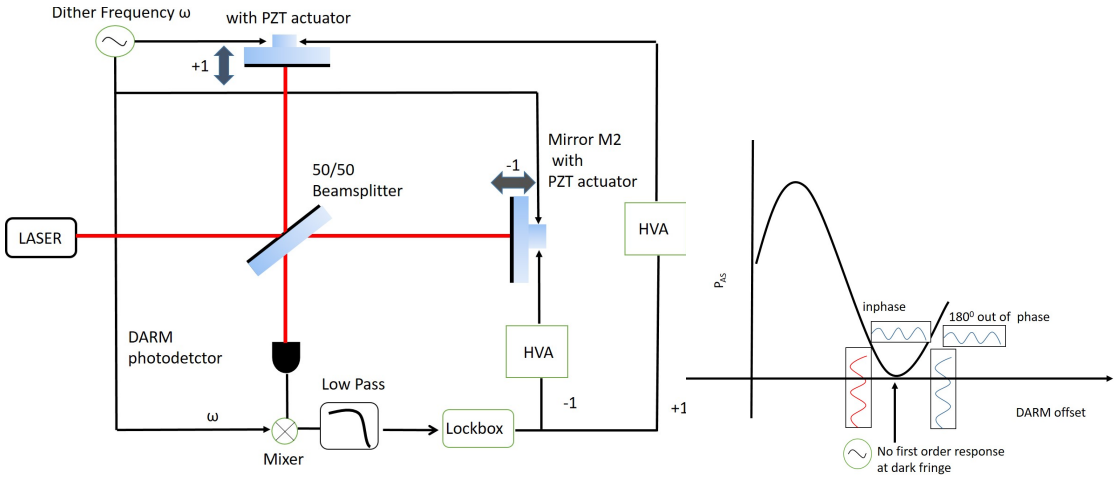

(i) Dither locking (ii) Cartoon view

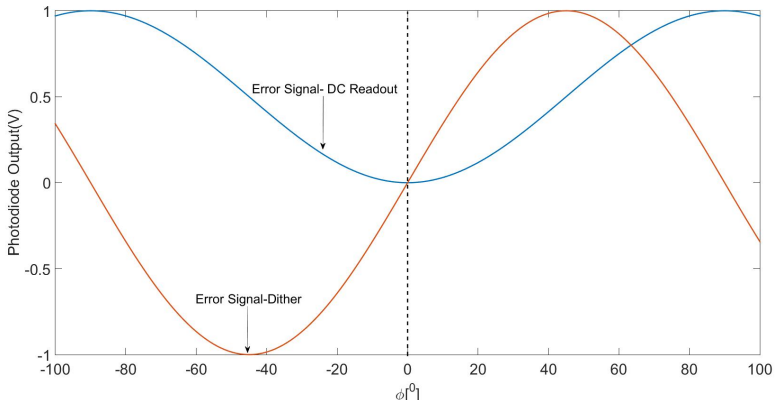

(iii) Error Signal

Figure 2.12: (i)Dither locking Technique: A sine modulation at audio frequency is applied to the piezos differentially. Here the photodiode output is demodulated by a mixer at the same frequency used as error signal to feedback it to the mirrors (ii) Cartoon view of dither locking:The figure shows the phase-flip that occurs as the system moves through the dark fringe. At the quadratic point (i.e at the dark fringe), the error signal is zero, while on either side it attains nonzero values with opposite signs. (iii) The error signal of the dither as a function of phase. It can be seen that the dark fringe corresponds to zero of the error signal

There are practical limitations that restrict the application of dithering, and in LIGO based interferometers, it is normally applied to lock auxiliary degrees of freedom where the signal to noise requirements are less severe. The limitations arise because dithering is commonly applied by mechanical means, resulting in restricted actuation force [48]. Dithering is, therefore, typically employed to monitor and control slowly varying aspects of the interferometer. For example, this technique is used in LIGO to counter any angular misalignment of the mirrors [48].

Schnupp Modulation Locking

In the Schnupp modulation technique the basic idea is to create a controlled modulation at the output port by applying a phase modulation using an EOM at certain frequency ω

to the laser beam before it enters the interferometer and introducing an intentional arm length difference ΔL between the two long arms [48], [49], [50]. By having an arm-length difference, leads to non-cancellation of side-bands. One can refer [51] for the calculations of the Schnupp modulation technique and is similar to the Pound-Drever-Hall technique as described in section 2.2.1. The photodetector signal from the interferometer output is then demodulated by a mixer at this frequency ω_m. It can be shown that the demodulated output u is given by [32],

$$u = 2J_0(m)J_1(m)\sin\phi \sin\frac{\omega_m \Delta L}{c} \tag{2.3.2.4}$$

where m is the modulation index and $J_0(m)$, $J_1(m)$ are Bessel functions.

From the above equation it can be seen that the error signal u obtained is proportional to $\sin(\phi)$ in comparison with DC readout, which has an error signal of $\sin^2(\phi)$. Hence the dark fringe corresponds to the zero of the error signal as shown in fig. 2.13 (ii), which is similar to the dither locking technique. Hence one can operate precisely near to the dark fringe using this technique. The phase between the electronic local oscillator and the output error signal while mixing down should be adjusted properly. This error signal is then sent differentially to both the mirrors as shown in fig. 2.13 (i).It can be seen that when $\Delta L = 0$, the error signal becomes zero and hence an intentional path length difference is maintained. It could be calculated from the above equation (2.3.2.4) that the optimum path difference to be maintained is given by $\Delta L = \lambda_m/4$. The simulation in fig. 2.13 (ii) is done using a software called *Finesse*[52]. The advantage of this method unlike dither is that since we are not inducing any mechanical motion to the PZTs attached mirrors we don't generate any mechanical instabilities in the system, while on the other side the disadvantage is that there is a reduction in visibility due to the intentional path length difference that is maintained. However, Schnupp technique has been used in many gravitational wave detector prototypes[53].

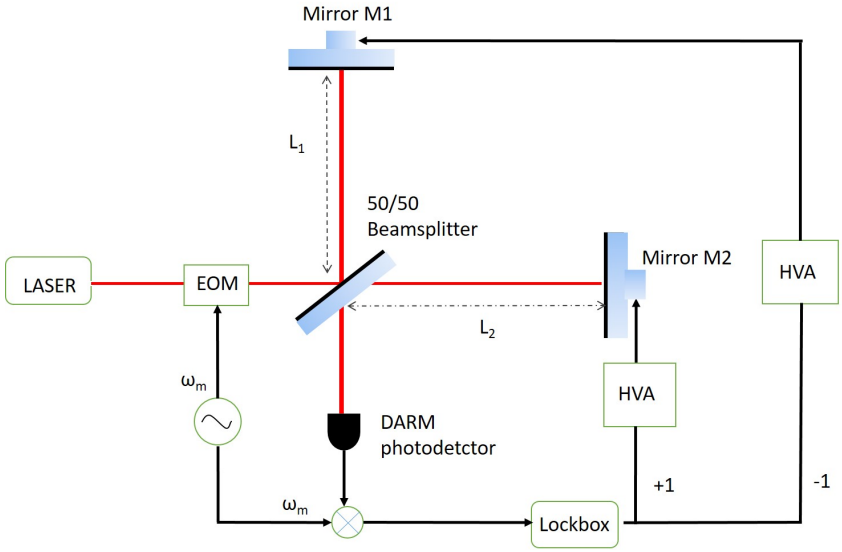

(i) Schnupp locking technique scheme of the interferometer

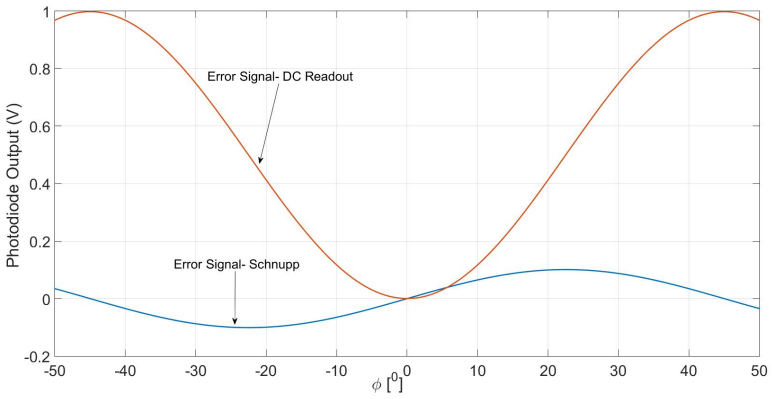

(ii) Error signal

Figure 2.13: (i) Experimental scheme using schnupp technique: the light after passing through the EOM enters the interferometer and an intentional path difference is maintained. (ii)The figure above plots the photodiode output and the demodulated output as a function of phase ϕ. When sidebands of frequency ω_m enter the interferometer and the signal is demodulated by a mixer, it could be seen that the dark fringe corresponds to the maximum slope of the error signal

Internal Modulation

In the Internal Modulation technique, the EOM is placed inside the interferometer to generate sidebands inside the interferometer at a certain frequency ω. The fig. 2.14 (i) depicts the experimental scheme. The photodiode signal from the interferometer output is demodulated by a mixer at this frequency ω. The concept is similar to the schnupp modulation technique since the sidebands itself are generated inside the interferometer, the error signal would be proportional to $\sin(\phi)$ in comparison with DC readout, $\sin^2(\phi)$. Hence the dark fringe corresponds to the zero of the error signal. We can operate precisely as in Schnupp Modulation technique at the dark fringe as it is on the maximum of the slope of the error signal as can be seen in fig. 2.14 (ii). This error signal is then sent differentially

to both the mirrors. The advantage of this method is that this phase modulator could be used also to simulate signals such as White Noise or single frequency noise. The only disadvantage of this method is that there would be losses due to EOM as it is placed inside the interferometer. Hence maximum care should be taken to avoid clipping of the beam at the EOM by placing appropriate lenses.

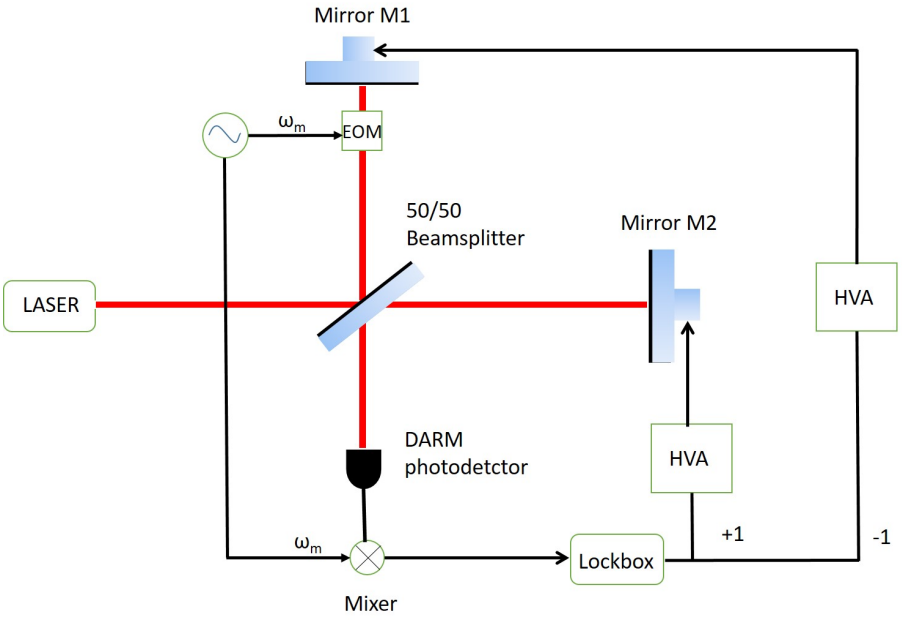

(i) Locking Scheme

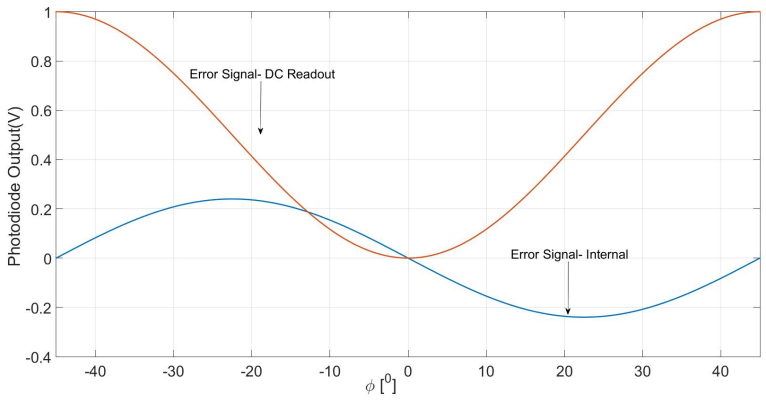

(ii) Error signal

Figure 2.14: (i) Internal modulation technique: The sidebands are generated inside the interferometer by placing the EOM in one of the arms of interferometer. (ii) The figure above plots the photodiode output and the demodulated output as a function of phase ϕ. It could be seen that the dark fringe corresponds to zero of the error signal which is on the maximum slope.

2.4 Power Recycling Interferometer

When a Michelson interferometer is operated near the dark fringe, most of the power is reflected back towards the laser. This reflected power could be recycled by placing

a partially transmitting mirror called a power recycling mirror (PRM) and forming a resonant cavity with the interferometer as shown in fig. 2.15. With this technique, as the power recycling P in the interferometer is increased by the power recycling, the shot noise reduces as the uncertainty is proportional to $\sqrt{P}$ as discussed in Chapter 1 in section 1.4.1. A Michelson interferometer operated at the dark fringe can be considered as a high-reflective compound mirror. The recycling mirror forms a recycling cavity with this compound mirror; the power in the cavity is enhanced when the cavity is resonant with the input laser beam. Hence the power recycling interferometer is combination of a Fabry-Pérot cavity and Michelson interferometer. In the next sections we will discuss about variation of output power as a function of DARM offset, calculation of optical gain

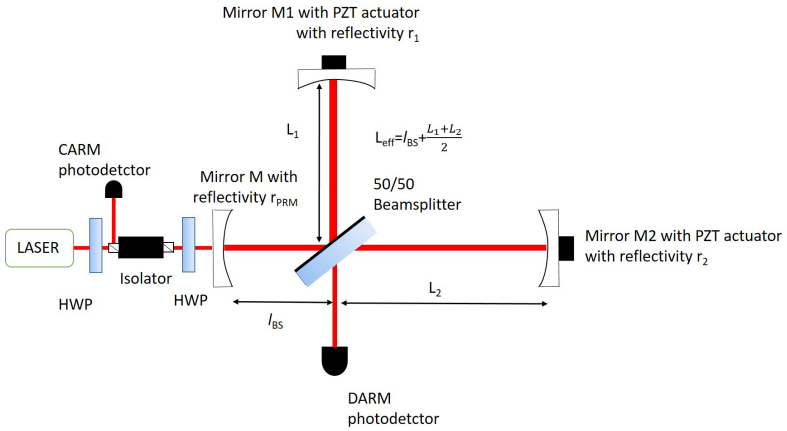

Figure 2.15: Power Recycling Michelson Interferometer: Since power recycling cavity is combination of both Fabry Pérot cavity and Michelson interferometer we need two photodetectors to stabilize the power recycling interferometer one for the DARM and the other for the CARM. More on locking of the interferometer is discussed in section 2.5.

2.4.1 Power Recycling Gain

The optical gain is defined as the ratio of power recycling inside the interferometer to input power. The PRM and rest of the Michelson interferometer setup as a Recycling cavity with E_{in} input electric field, E_{cir} field circulating inside the interferometer and E_{eff} the effective electric field after the reflection from the beam splitter as shown in fig. 2.16.

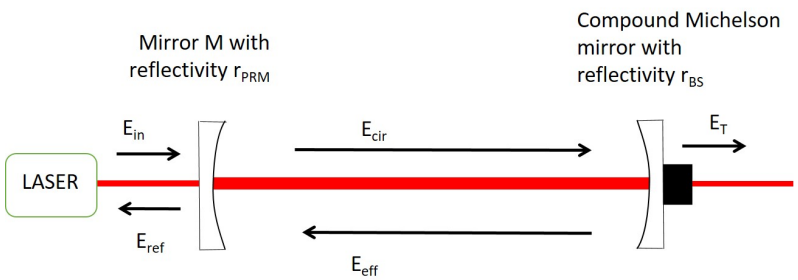

Figure 2.16: The power recycling Michelson interferometer is equivalent to a Fabry-Pérot Cavity formed between power recycling Mirror and Compound Michelson mirror

The fields in the recycling cavity are,

$$E_{eff} = t_{PRM}E_{in} + r_{BS}E_{cir} \tag{2.4.1.1}$$

$$E_{cir} = r_{BS}E_{eff} \tag{2.4.1.2}$$

$$E_{ref} = -r_{PRM}E_{in} + t_{PRM}E_{cir} \tag{2.4.1.3}$$

$$E_T = -r_{PRM}E_{in} + t_{BS}E_{cir} \tag{2.4.1.4}$$

where r_{BS} is the reflectivity of the Michelson Interferometer, r_{PRM} and t_{PRM} are reflectivity and transmittivity of the recycling mirror, t_{BS} is the transmittivity of the interferometer. From above equations, we obtain the expressions for the amplitude gain of the recycling cavity g as

$$g = \frac{E_{eff}}{E_{in}} = \frac{t_{PRM}}{1 - \sqrt{(R_{PRM}R_{BS}R_{EM})}} \tag{2.4.1.5}$$

where $R_{BS} = r_{BS}^2$, $R_{EM} = r_{EM}^2$, $R_{PRM} = r_{PRM}^2$

Since R_{BS} represents the reflectivity of compound Michelson mirror, it could be written as $R_{BS} = \cos^2(kx)$. The reflectivities of both the end mirrors are assumed to be the same and k is the wavenumber. The ratio of the optical power at the beamsplitter respectively in presence and in absence of the recycling mirror, G, is called power recycling gain or power recycling factor:

$$G = g^2 = \left|\frac{E_{eff}}{E_{in}}\right|^2 = \frac{t_{PRM}^2}{(1 - \sqrt{R_{PRM}R_{EM}R_{BS}})^2} \tag{2.4.1.6}$$

When $G > 1$, the power in the interferometer increases by GP_{IN}, hence the shot noise level is improved by $\sqrt{G}$.

Similarly, the power at the anti-symmetric port is,

$$P_{AS} = |E_T|^2 = \frac{P_{IN}\sin^2(kx)}{(1 - \sqrt{(R_{PRM}R_{EM}R_{BS})})^2} \tag{2.4.1.7}$$

The Finesse of the power recycling cavity as a function of DARM offset is given by,

$$F = \frac{\pi(R_{PRM}R_{BS}R_{EM})^{\frac{1}{4}}}{(1 - R_{PRM}R_{BS}R_{EM})} \tag{2.4.1.8}$$

where $R_{BS} = \cos^2(kx)$. The simulation of the power at the anti-symmetric port as a function of DARM offset is presented in fig. 2.17 (i). At $\phi = 0$, the perfect destructive interference leads to null power. In a narrow region near to this condition, we have a low-losses cavity, which means a high cavity gain, inducing a sudden increase of P_{AS}. However, when we move far enough to the $\phi = 0$ condition, losses in the power recycling cavity start to dramatically reduce the finesse and the cavity gain accordingly, so also P_{AS} starts decreasing. The results of these two opposing effects is that the dark fringe region is much narrower than in the case of standard Michelson Interferometer.

The power recycled Michelson interferometers at LIGO/VIRGO consists of 4km linear

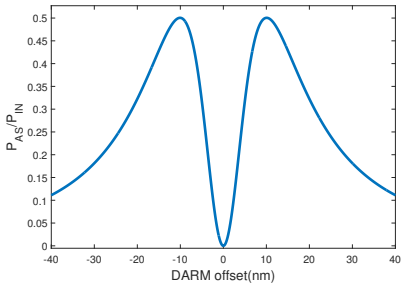

(i) P_{AS} vs DARM offset

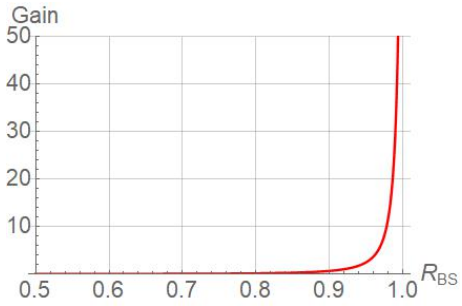

(ii) Gain vs R_{BS}

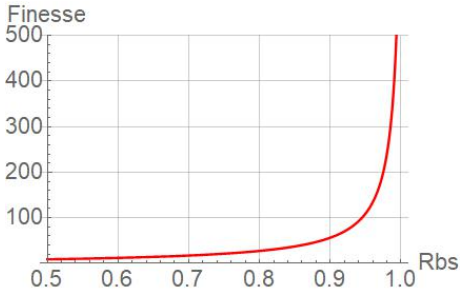

(iii) Finesse vs R_{BS}

Figure 2.17: (i)Power at anti-symmetric port as a function of DARM offset. (ii) Gain as function of DARM offset. When r_{BS} is close to one it can be seen that power recycling gain is very high. (iii)Finesse as a function of DARM offset. It can be seen that as we move away from dark fringe, the finesse decreases

Fabry-Pérot cavities in their arms known as "arm cavities" along with a signal recycling mirror. The enhancement in the phase measured, can be achieved by increasing the length, i.e. by a factor of FL, F being the finesse of the arm cavities and L being the length of arm cavities. Figure 2.18 depicts the experimental setup of the LIGO. The typical order of the power recycling gain of the interferometer is around 30-70 times the input power[39].

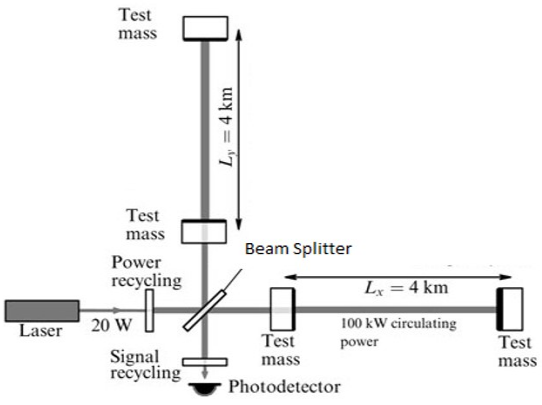

Figure 2.18: Experimental setup of the power Recycling Michelson interferometers at LIGO. The interferometers consists of power Recycled Michelson setup with arm cavities and signal recycling Mirrors in it [21]

The interferometers at Fermilab do not have arm cavities. This is because, the holographic noise is expected to be present until the frequency $c/2L$, L being the length of arm

of interferometer. Since the Fabry-Pérot cavities act as a lowpass filter, the presence of arm cavities would limit the existence of noise below MHz frequency. Figure 2.19 depicts the experimental setup of the holometer.

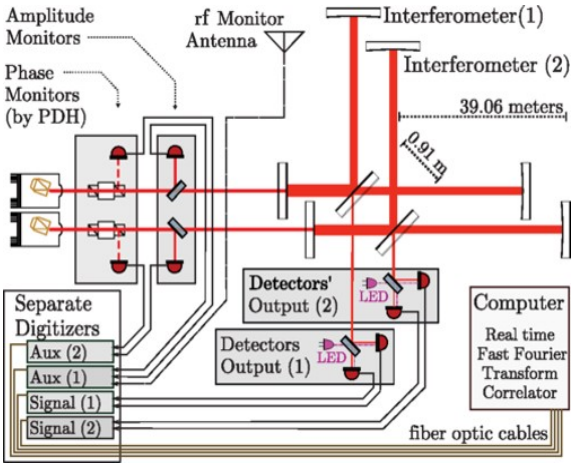

Figure 2.19: Experimental setup of the double power recycling Michelson interferometers at Fermilab [27]. The interferometers consists of power Recycled Michelson setup without the arm cavities.

2.4.2 Mode-matching of the Power Recycling Cavity

The size and shape of the output mode of the Power Recycling cavities are determined by three factors: a) curvature of the partially reflecting mirror b) curvature of the highly reflecting end mirrors and c) the effective length of the power recycling cavity $L_{eff} = l_{BS} + \frac{(L_1+L_2)}{2}$ (In the remainder of the thesis I would refer this effective length as *common arm* length, (CARM)). The Power Recycling cavity needs to be well mode matched to maximize the power build up and avoid high contrast defects. Proper lenses have to be arranged such that the cavity is well mode-matched. Since power recycling interferometer is an equivalent Fabry-Pérot cavity, the lenses could be calculated in the same way as in section 2.2.3 by choosing the length of the cavity as effective length of the interferometer.

2.5 Locking of the Power Recylcing Interferometers

Since power recycling cavity is a combination of both Michelson interferometer and Fabry-Pérot cavity, there are two degrees of freedom to be controlled as mention in fig. 2.15 and two detectors are required for locking the interferometer. The DARM of the interferometer should be locked near to the dark fringe while the CARM is locked to the resonance i.e $L_{eff} = l_{BS} + \frac{L_1+L_2}{2} = m\lambda$. The DARM is locked by using any of the locking techniques mentioned in section 2.3.2 while the CARM is locked using the Pound-Drever-Hall technique accordingly in section 2.2.1. The order of locking is important when we stabilize the power recycling interferometer, since the Finesse of the cavity changes with respect to the fringe position. Hence the DARM is locked initially to a point on the fringe followed by locking of the CARM to the resonance.

In most of the gravitational wave detectors, DC locking technique and Schnupp modulation technique are used to control the DARM. However we have used internal modulation technique in our experiment which would be mentioned in Chapter 3 of section 3.2.1. In the following are details in 4 figures representing the different schemes for locking the Power Recycled Michelson Interferometer.

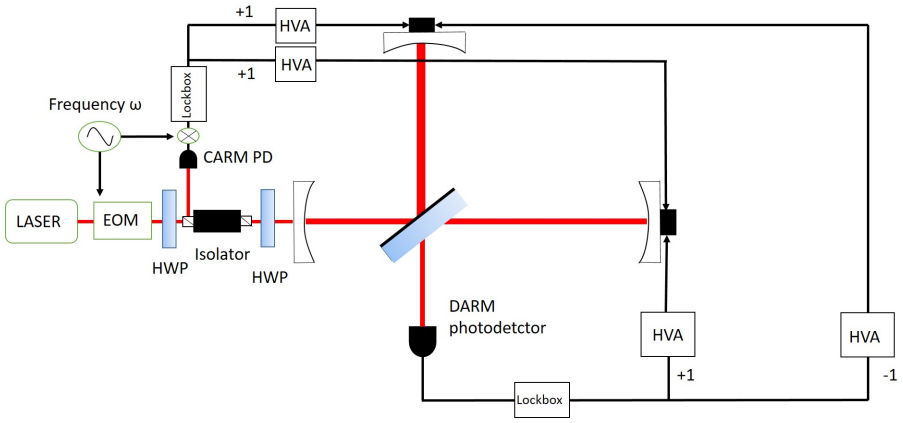

Figure 2.20: **DC locking**: The DARM is locked using the DC locking technique and the CARM is locked using the Pound -Drever-Hall technique. The DARM output signal is directly sent differentially to end mirrors (i.e by phase shift of π) while the CARM error signal equally to end mirrors. The error signal of the CARM is obtained by demodulating the PD output at frequency ω and is locked to the zero which corresponds to the resonance of the cavity as mentioned in section 2.2.1. PD: Photodiode; HWP :Half wave plate; HVA: High voltage Amplifier; EOM:Electro optic Modulator.

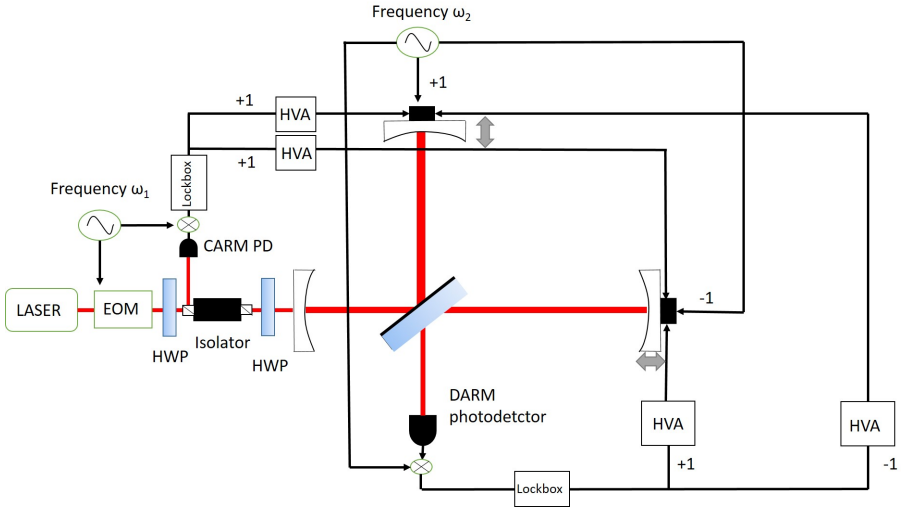

Figure 2.21: **Dither Locking**: The DARM is locked using the Dither locking technique and the CARM is locked using the Pound -Drever-Hall technique. As we have discussed in section 2.3.2 the PZT's are given small modulation at audio frequency range at frequency ω_2 differentially and the DARM PD output is demodulated at same frequency ω_2. The error signal obtained after demodulation is sent differentially to the mirrors (with phase of π) for locking it near to the dark fringe of the interferometer. The Pound Drever hall error signal generated after the demodulation at frequency ω_1 is sent equally (without any phase) to mirrors for locking the CARM of the interferometer to the resonance. PD: Photodiode; HWP :Half wave plate; HVA: High voltage Amplifier; EOM:Electro optic Modulator.

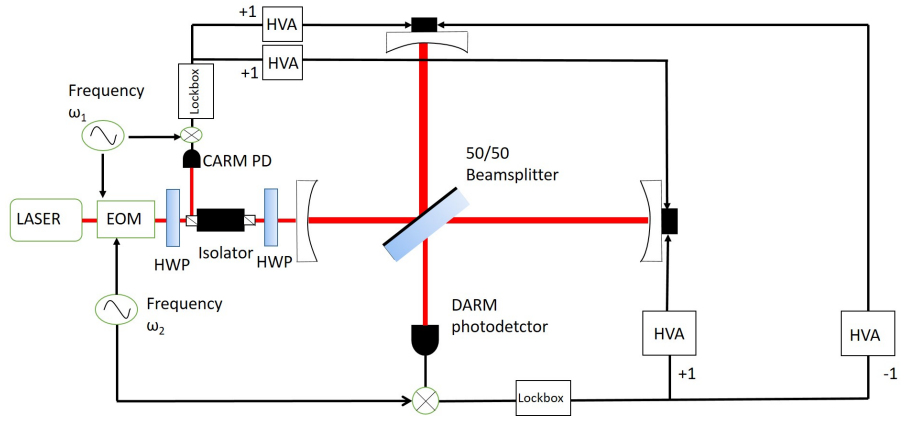

Figure 2.22: **Schnupp Modulation Technique**: The DARM is locked using the Schnupp locking technique and the CARM is locked using the Pound -Drever-Hall technique. An intentional path length is maintained so that the sidebands of frequency ω_2 enter the interferometer for locking. The frequency ω_2 should be chosen such they are within the bandwidth of the power recycling cavity. The DARM PD output is demodulated at same frequency ω_2 and the error signal is sent differentially (with phase of π) for locking it near to the dark fringe of the interferometer. The Pound Drever hall error signal generated at frequency ω_1 after the demodulation is sent equally to mirrors for locking the CARM of the interferometer to the resonance. PD: Photodiode; HWP :Half wave plate; HVA: High voltage Amplifier; EOM:Electro optic Modulator.

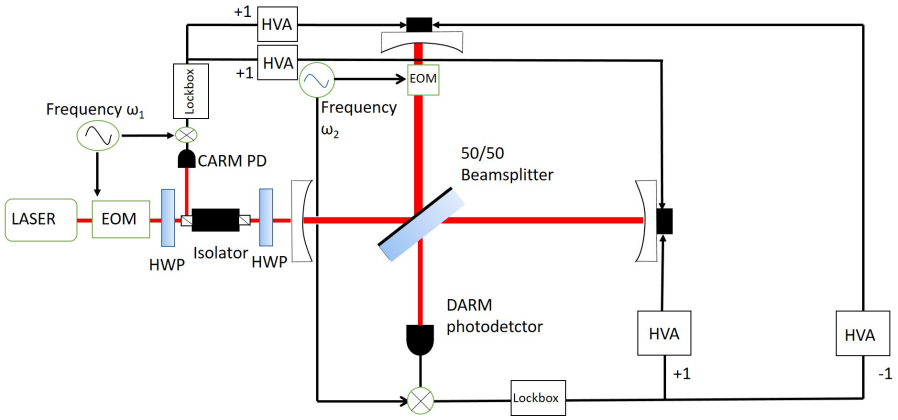

Figure 2.23: **Internal Modulation Technique**:The DARM is locked using the Internal modulation locking technique as discussed in section 2.3.2 and the CARM is locked using the Pound -Drever-Hall technique. The sideband frequencies ω_2 are generated inside the interferometer by placing EOM inside one of the arms of the interferometer. The DARM PD output is demodulated at same frequency ω_2 and the error signal is used for locking it near to the dark fringe of the interferometer. The Pound Drever hall error signal generated after the demodulation is sent equally (without any phase) to mirrors for locking the CARM of the interferometer to the resonance. PD: Photodiode; HWP :Half wave plate; HVA: High voltage Amplifier; EOM:Electro optic Modulator.

2.6 Chapter Summary

In this chapter we have introduced Fabry-Pérot cavities, Michelson interferometer and power recycling interferometers. Since power recycling cavity works on combination of both Fabry-Pérot cavities and Michelson interferometer both have been studied rigorously. Various properties such as finesse, impedance matching and Pound-Drever-Hall locking technique corresponding to the Fabry-Pérot Cavity have been thoroughly discussed. Similarly concepts of Michelson interferometer such as visibility, different types of locking schemes for Michelson interferometer like DC locking, Schnupp locking technique and internal modulation technique have been discussed.

CHAPTER 3

DESCRIPTION OF THE SETUP

3.1 Introduction

In this chapter we provide description of our experimental setup. This can be divided in two parts:
a) The classical part consisting of the power recycled Michelson interferometers: The optical and electronic setup (characterization of the fringe described in section 3.2.3) have been discussed in this present chapter; b) The quantum part that consists of squeezed light source and its injection in the interferometers. As we have discussed in chapter 1, the advantage of squeezed light injection has been demonstrated in large scale interferometers devoted to gravitational wave detectors and in many table top experiments [38], [39]. In this part we describe the experimental setup of quantum light generation, both squeezed vacuum as well as for twin beam like states. The quantum noise locking technique used to lock the interferometer phase to the squeezing quadrature will be discused in section 3.3.3.

3.2 The experimental set-up (semi-classical configuration)

As discussed in section 1.5 of Chapter 1, our system consisted of two Michelson interferometers (in particular power recycling Michelson interferometers) placed close to each other with small separation between the two beam-splitters.

Figure 3.1 depicts the simplified schematic of the experimental setup. A Nd-YAG laser with an output power of 300 mW at wavelength 1064nm was used for the experiment. Some part of the light was used for generation of the squeezed light setup while some input power around 1.5 mW for each interferometer was used. For having an efficient TEM_{00} input mode, the light from the laser was fiber coupled and was used for the interferometers. Each interferometer was formed by a power recycling mirror having the radius of curvature being 1.5m with end plain mirrors *M1* and *M2* (reflectivity around 99.9%) stabilized by a PZT actuators attached and a 50-50 beam splitter as shown in fig. 3.1. The power recycling mirror's reflectivity was choosen to be of 90% to form an over-coupled cavity with end

mirrors when locked near the dark fringe as discussed in section 2.2.2. The length of each arm of the interferometer was around 92 cm. The distance between the two beam splitters was around 8 cm. A set of lenses were placed before the interferometers for mode matching the power recycling interferometer as described in section 2.2.3 such that the waist of the beam is at the end mirror. An InGaAs photodiode with high quantum-efficiency (99%) and low noise (Noise Equivalent Power $1.2e-11\,W/\sqrt{Hz}$) was used for stabilizing the DARM near the dark fringe while the CARM signal was stabilized using another resonant photodetector at 20 MHz.

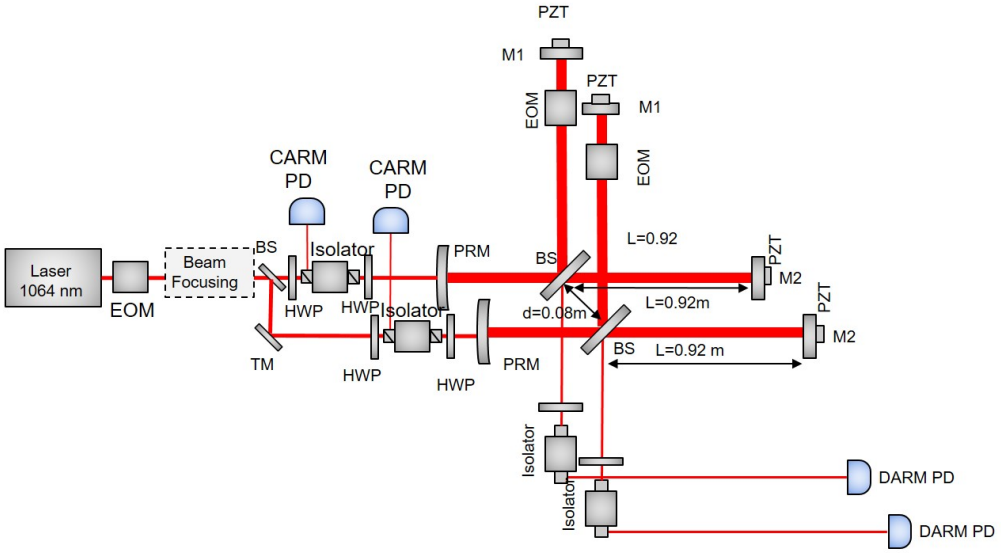

Figure 3.1: Simplified schematic of the double-interferometer setup. Two Michelson Interferometers with arm length $L = 0.92m$ were co-located, with a distance between the two balanced beam splitters (BSs) of around 8cm. M1,M2: piezo-actuated high-reflectivity (99.9%) end mirrors. PRM: partially reflecting (90%) power recycling mirror, radius of curvature $r_c = 1.5m$.;HWP:Half waveplate; PD: Photodetector; BS: Beam splitter

3.2.1 Locking of the Power Recycling cavities

Figure 3.2 depicts the detailed locking scheme of each interferometer. A resonant Electro Optic Modulator (EOM) was placed before the interfereometers for generating phase modulation at frequency 20 MHz to lock the CARM of the interferometer by Pound-Drever-Hall technique while another phase modulator which consists of Rubidium Titanyle Phosphate (RTP) crystal (4mm x 5mm area) was placed inside the interferometer, to generate sidebands at 7.6 MHz for stabilizing the DARM. The phase modulator, inside the interferometer was placed very close to the end mirror to avoid clipping of the beam, as the waist of the interferometer was at the end of the mirrors. This phase modulator was also used to inject signals for simulating phase noises for the current experimental scheme, which will be discussed in chapter 4. As stated previously in section 2.5, the DARM was locked near to the dark fringe through the internal modulation technique by generating the side-bands at 7.6 MHz with the help of the phase modulator placed inside the interferometer. We have used a set of Proportional-Integral controller (PI controller) lock boxes which have inbuilt low pass filters for stabilizing the DARM of the interferometer. More

details of the PI controller circuit are described in Appendix C.

Each DARM photodetector consists of two DC-outputs, two 100kHz high passed AC outputs and an in-built mixer used for quantum noise locking. One of the AC output was used for locking the DARM mode while the other AC output was used for data acquisition (see Appendix C for more information on the electronic circuit of the photodetector). The 100 kHz high passed AC output of the DARM photodetector was down mixed at 7.6 MHz frequency. The phase between the electronic LO and the AC output signal from the photodetector was adjusted properly to maximize the slope of the error signal and to have the dark fringe on the zero of the generated error signal. The generated error signal from the mixer was fed back to the piezo-driven end mirrors differentially (i.e with a phase of π) with a help of a High voltage Amplifier. The 20 MHz sidebands produced from the resonant EOM was used for locking the CARM of the interferometer. The output of the CARM Photodetctor was down mixed at 20MHz and the error signal was fed back to both the piezo driven end mirrors without no relative phase lag after passing through a high voltage amplifier (HVA).

3.2.2 Characterization of Michelson Visibility

Before we characterize the fringe of the power recycling Michelson interferometer, it is necessary to characterize the fringe of non recycling Michelson interferometer by performing a visibility measurement as mentioned in Section 2.3.1. For this purpose, the PZT actuator is driven with help of a function generator and high voltage amplifier. The power at the antisymmetric port is plotted as a function of input voltage V_{in} given to the PZT. The curve is fitted with the equation

$$P_{AS} = (P_1 + P_2 \sin^2(bV_{in}(t)) \tag{3.2.2.1}$$

where b is the conversion constant from Volts to meter that could be used to evaluate sensitivity , P_1 is the offset power which gives us the amount of losses while P_2 is the power at the beam splitter. The Visibility V is then evaluated using the equation (2.3.1.1). The contrast defect ϵ is defined as the amount of mode mismatch between the two arms of the interferometer and is given by $\epsilon = 1 - V$. The fig. 3.3 plots the visibility as a function of Piezo voltage. The Visibility obtained was around $(99.01 \pm 0.04)\%$ from the fit.

Balancement

For achieving high visibility, we need to have equal arm length . If the arm lengths are equal, a change in the frequency of laser does not effect the fringe and the output signal, when the arm length is different the system is sensitive to the laser ($\delta\phi = \frac{2\pi\Delta L\delta\nu}{c}$). To balance the arms of the Michelson interferometer, the interferometer was stabilized at a certain point of the fringe and a frequency noise of the laser was introduced outside the bandwidth of the feedback loop of the interferometer. One of the end mirror was mounted on a micrometer stage. The height of the noise peak was registered on a spectrum analyzer at a frequency beyond the unity gain frequency, while moving the micrometer. The point

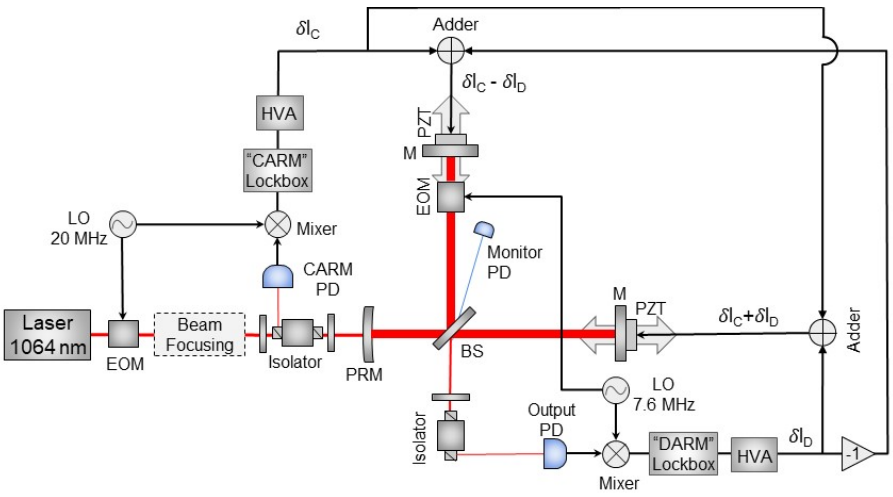

(i) Locking scheme of the interferometer

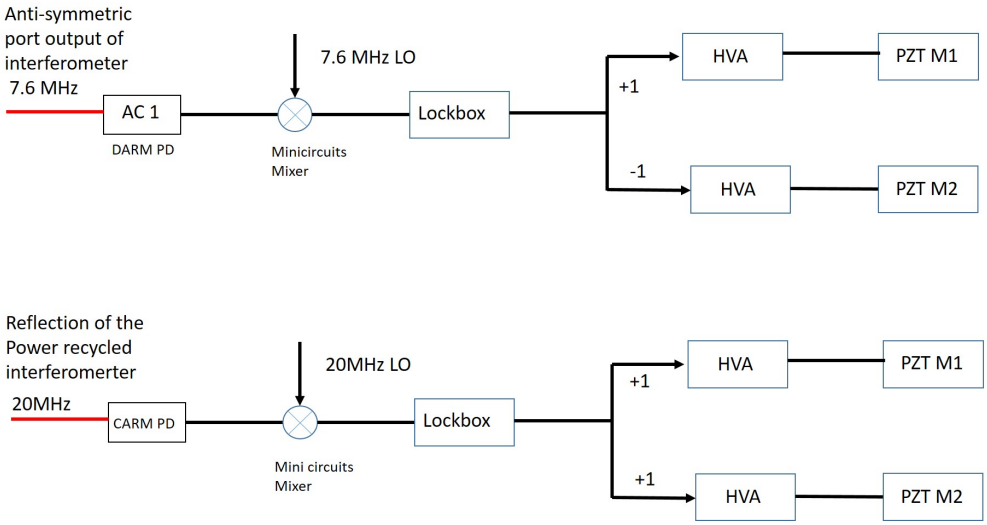

(ii) Connections for the locking

Figure 3.2: (i)Detailed Locking schematic of each interferometer. PZT: piezo-electric actuator. EOM: electro-optical modulator. HVA: high-voltage amplifier. LO: local oscillator. PD: photo-diode, InGaAs with high quantum-efficiency photodiodes (99%) and low noise (Noise Equivalent Power $1.2e-11\,W/\sqrt{Hz}$) are used at the read-out port. Beam-Focusing: set of lenses in order to have Gaussian Optical mode TEM_{00}. $\delta l_C, \delta l_D$: correction signals from the CARM and DARM lockbox respectively. The DARM was locked using the internal modulation technique while the CARM was locked using the Pound-Drever-Hall technique (ii) Pictorial representation of locking connections of the power recycling interferometer.

of minimum, where the noise cancels off completely is called the balancement point.

3.2.3 Characterization of Power Recycling Interferometer

When the Michelson interferometer is brought back to the power recycling configuration, the modes of the cavity can be traced out by locking the DARM of the interferometer and

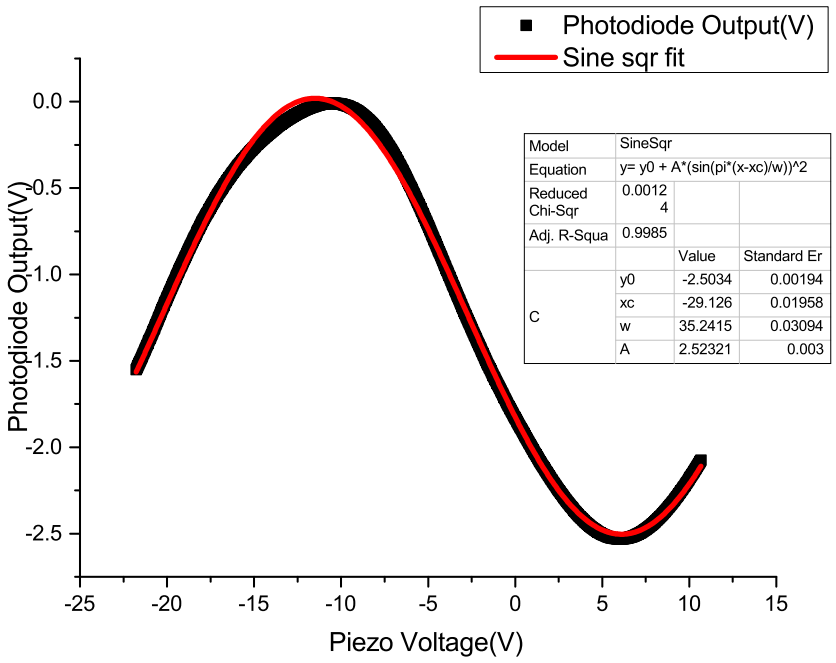

Figure 3.3: Power at the anti-symmetric port was curve fitted with equation (3.2.2.1). Visibility obtained was around 99% from the curve fitting

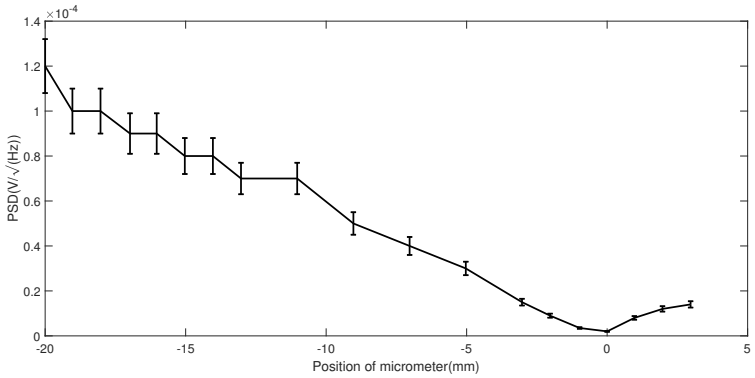

Figure 3.4: The height of the frequency noise peak is plotted as a function of path length difference. The height of PSD where minimum was obtained is the point of Balancement.

scanning the CARM of the Power Recycled Interferometer. The figure fig. 3.5 (i) shows the modes of the power recycled cavity. The main peak represented in the cavity is the TEM_{00} spatial mode while the other correspond to higher order modes of the cavity. This height of the main peak changes as we tune the DARM offset of the Michelson Fringe. The fig. 3.5(ii) shows the part of TEM_{00} with the red curve represented by the Pound-Drever-Hall error signal of the power recycled cavity. As discussed in section 2.2.1 for locking the cavity to the resonance we need to lock to the zero of the error signal. From the figure fig. 3.5 (i) we can calculate the mode matching percentage (MM%) as:

$$\mathrm{MM}(\%) = \frac{h_{\mathrm{TEM}_{00}}}{\sum_i h_i} \tag{3.2.3.1}$$

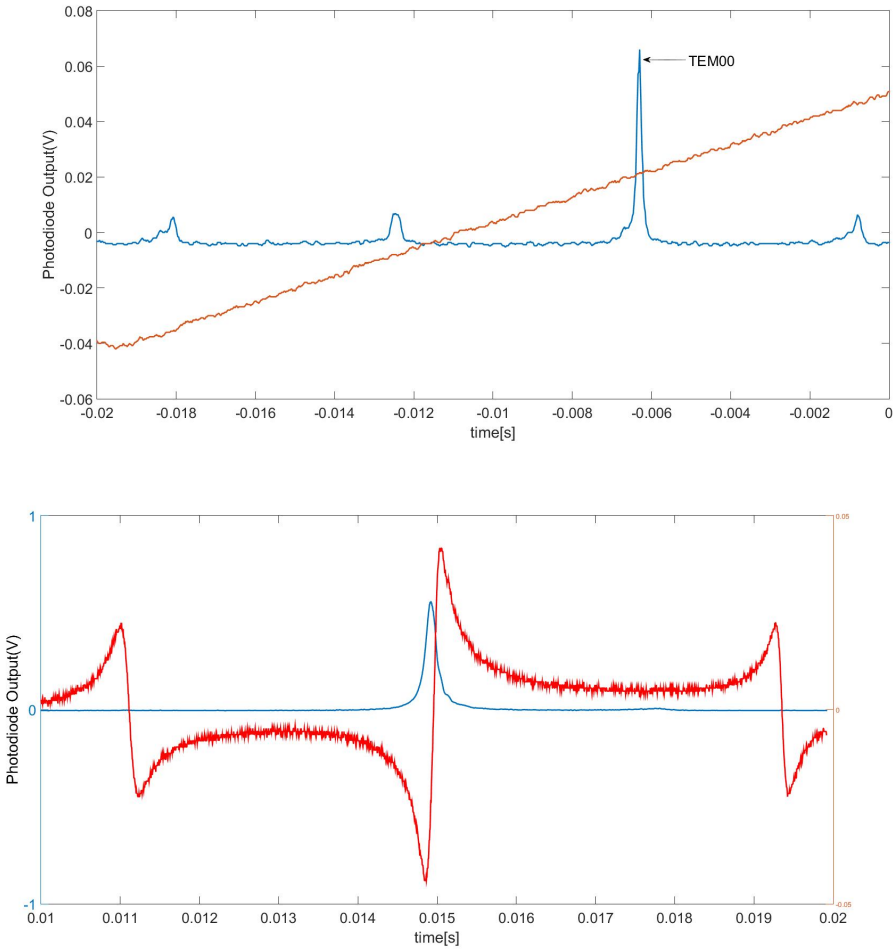

Figure 3.5: (i)The figure above shows the modes of the Power recycled cavity when the DARM is locked at certain point of the fringe. (ii) The figure above shows the DARM output cavity peak recorded along with its Pound-Drever-Hall error signal of the cavity.

where $h_{\mathrm{TEM}_{00}}$ is height of the TEM_{00} and h_i represents the height of all the modes. In our case, the mode matching percentage was around 94%.

For characterizing the fringe of the power recycling configuration, the DARM was locked at each offset of the Michelson fringe simultaneously with CARM. To measure the power recycled inside the cavity, we picked-off a small percentage (about 0.5%) of light, which was reflected by the rear surface of the central beam splitter because of the non- perfect anti-reflection coating (pick -off beam) by using a monitor photodetector as depicted in fig. 3.2. This picked-off signal was used to calculate the gain as follows :

$$G = \frac{P_{cav}}{P_{cav-misaligned}} \tag{3.2.3.2}$$

where P_{cav} is the optical power inside the cavity when it is locked, while $P_{cav-misaligned}$ is the optical power when the cavity is misaligned.

From the experimental point of view, one could rewrite the power at the antisymmetric port as a function of DARM offset considering the lossses η as the transmission loss from

the output of the interferometer to detector as:

$$P_{AS} = P_{BS}\eta[\epsilon/2 + (1-\epsilon)\sin^2(kx)] = P_{IN}G\eta[\epsilon/2 + (1-\epsilon)\sin^2(k\Delta X_{offset})] \quad (3.2.3.3)$$

where P_{BS} is the power at the beam spliiter , P_{IN} is the input power to the interferometer and G is the power recycling gain given by,

$$G = \frac{T_{PRM}}{(1-\sqrt{(R_{PRM}R_{EM}R_{loss}R_{BS})})^2} \quad (3.2.3.4)$$

where $T_{PRM} = t_{PRM}^2$, R_{EM} is the reflectivity of the end mirrors, R_{loss} is a loss term due to miscellaneous losses which includes also losses due to mode matching, η is the transmission efficiency from the beam splitter to the photodetctor and ϵ is the contrast defect evaluated by visibility of misaligned power recycled cavity forming simple michelson as discussed in subsection 3.2.2. R_{BS} is the reflectivity at the beam splitter given by $R_{BS} = \cos^2(k\Delta X_{offset})$. The power at the beam splitter can be evaluated as $P_{BS} = P_{IN}G$.

Hence we can rewrite P_{AS} in terms of Gain G using equation (3.2.3.3) and (3.2.3.4) as,

$$P_{AS} = \left[(1-\epsilon)\cos^2\left(\sin^{-1}(\frac{1}{\sqrt{R_{PRM}R_{EM}R_{loss}}}(1-\sqrt{\frac{T}{G}}))\right) + \frac{\epsilon}{2}\right]\eta P_{IN}G \quad (3.2.3.5)$$

From the fit in fig. 3.3, the contrast defect was evaluated as $\epsilon = 0.01$. As discussed in section 2.4.1, as we move away from the dark fringe, the power measured on the output port increases until certain point and decreases for a displacement corresponding to the bright fringe of the interferometer without recycling. The power at the anti-symmetric port P_{AS} as a function of power recycling gain G is plotted and a fit was performed using the equation (3.2.3.5)in the fig. 3.6. The transmission efficiency η was around 79%. An independent estimation of $T_{PRM} \approx 0.09$ was evaluated from the fit, which was indeed close to the transmittivity of the PRM. The evaluated R_{loss} was around 93.5% and this corresponds to 6.5% of miscellaneous loss. The summary of the parameters evaluated are given in table 3.1

η	$(79.3 \pm 0.1)\%$
T_{PRM}	(0.089 ± 0.001)
R_{loss}	$(93.5 \pm 0.1)\%$

Table 3.1: Evaluated parameters from the fit of P_{AS} vs G in fig. 3.6

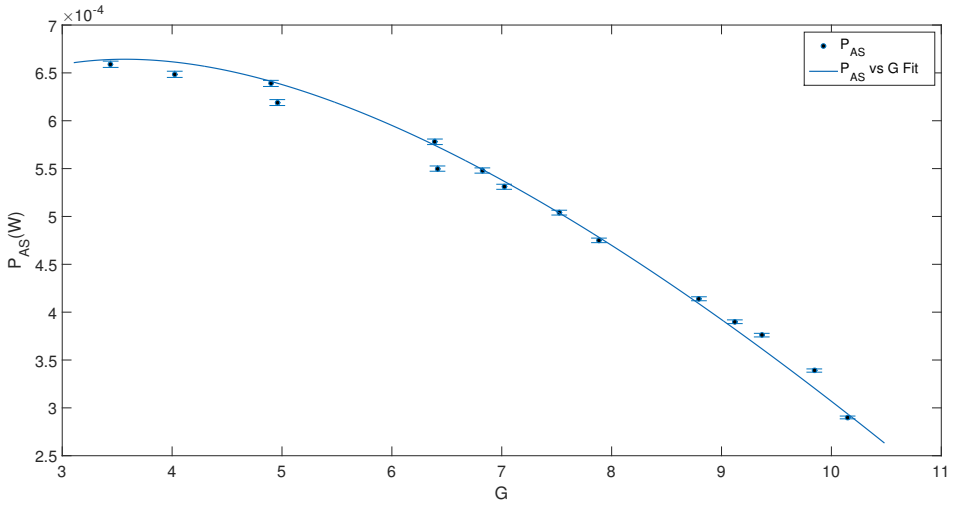

Figure 3.6: Power at the antisymmetric port P_{AS} vs power recycling Gain G

From equation (3.2.3.4) we can evaluate the displacement ΔX_{offset} as

$$\Delta X_{offset} = \frac{\lambda}{2\pi}\left[\cos^{-1}\left(\frac{1}{\sqrt{R_{PRM}R_{EM}R_{loss}}}(1-\sqrt{\frac{T}{G}})\right)\right] \tag{3.2.3.6}$$

Therefore, using equation (3.2.3.5) and parameters of the fit fig. 3.6 from table 3.1, we plot the power at the anti-symmetric port as a function of ΔX_{offset} using equation (3.2.3.3) in fig. 3.7

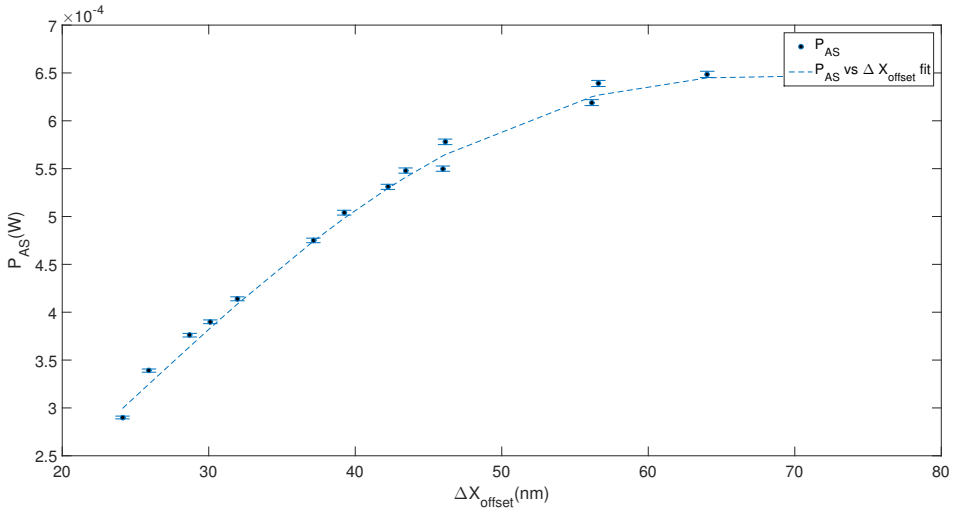

Figure 3.7: Power at the anti-symmetric port P_{AS} vs Dispacement ΔX_{offset}

3.3 Experimental Setup (Quantum light injection)

Single-mode squeezed vacuum states are generated by a process called spontaneous parametric down-conversion. The Hamiltonian of the process is given by [54],[55],

$$H = \kappa(\hat{a}^2 - \hat{a}^{+2}) \tag{3.3.0.1}$$

for polarization and frequency degenerate case, where $\hat{a}$ and $\hat{a}^+$ are annihilation and creator operators. The Unitary evolution is given by $U = e^{-iHt/\hbar} = e^{(-it\kappa(\hat{a}^2-\hat{a}^{+2})/\hbar)}$ which is nothing but the squeezed operator represented in Chapter 1 in section 1.3.2

In the process of SPDC, a pump photon with frequency ω_p, incident on a dielectric crystal with a $\chi^{(2)}$ non linearity, is converted into two new photons; a signal photon of frequency ω_s and an idler photon of frequency ω_i as shown in fig. 3.8 (i). There are two conditions to be satisfied for SPDC to occur.

The first is the energy conservation condition: $\hbar\omega_p = \hbar\omega_i + \hbar\omega_s$. For degenerate PDC, the idler and signal photons are indistinguishable in frequency ($\omega_i = \omega_s$) and polarization. The second condition is the phase matching condition where the momentum of the involved fields has to be conserved, that is $\vec{k_p} = \vec{k_s} + \vec{k_i}$ where $\vec{k_p}$ is the wave vector for the incident pump beam while $\vec{k_s}$ and $\vec{k_i}$ are the wave vectors associated with the signal and idler beams, respectively. The fig. 3.8 (ii) represents the phase matching condition and fig. 3.8 (iii) represents the energy conservation condition. Hence we can write,

$$\frac{n_i\omega_i}{c} + \frac{n_s\omega_s}{c} = \frac{n_p\omega_p}{c} \tag{3.3.0.2}$$

where n_i, n_s and n_p represent the refractive index experienced for the idler, signal and pump beam. These refractive indices are highly dependent on Temperature and hence the phase mismatch $\Delta k = \vec{k_p} - \vec{k_i} - \vec{k_s}$ depends on temperature. Hence fine tuning of temperature is required in general for satisfying the phase matching condition.

The coupling constant κ in equation (3.3.0.1) is related the nonlinear susceptibility $\chi^{(2)}_{eff}$ and geometry of the crystal [54], [56]. The $\chi^{(2)}_{eff}$ non linearity is, in general, very weak and hence in order to observe a significant induced polarization of the medium and efficient squeezing, the crystal is placed inside a cavity and SPDC takes place inside the cavity. This type of configuration is known as Optical Parametric Oscillator. More on Optical Parametric Oscillators could be read in [57],[58].

3.3.1 Generating squeezed states

We used two independent squeezed vacuum states to be injected into each interferometer system. Figure 3.9 depicts the experimental scheme for preparation of squeezed light source. Each squeezer comprises of a ppKTP (periodically poled Potassium Titanyl Phosphate) crystal placed inside a semi-monolithic cavity as shown in fig. 3.9 (i) formed by the edges of the crystal and transparent mirror of reflectivity 90%. A separate 1064 nm beam known as control beam was passed through a EOM with generation of phase modulation of 37.22 MHz and 36.5 MHz respectively for each squeezer cavity and was used to lock it using Pound-Drever-Hall technique with the help of PZT actuator attached to the transparent mirror. An internal module for second harmonic generation provided the 532 nm radiation as a pump for the generation of squeezed light. The pump beam was initially sent to a mode-cleaner to have clean TEM_{00} mode. The output pump beam from the mode cleaner was then incident on the crystal for having parametric down conversion inside the locked cavity. To establish a phase-match condition between the pump and the control

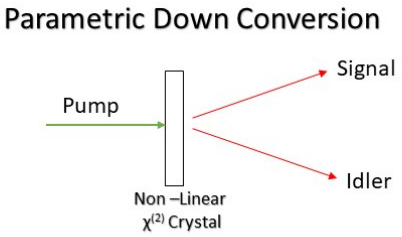

(i)

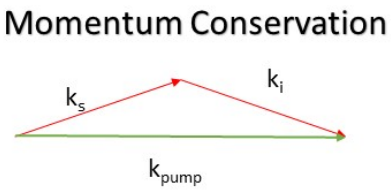

(ii)

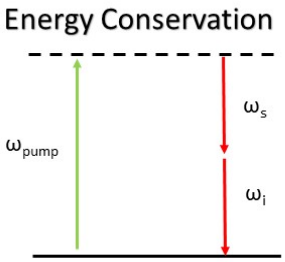

(iii)

Figure 3.8: (i) Parametric down conversion scheme: Light is incident on the non linear $\chi^{(2)}_{eff}$ material, splitting into signal and idler, (ii) Phase matching condition, (iii) Energy conservation condition.

beam, the crystals temperature was actively stabilised with a servo mechanism, a Peltier element and a thermistor, which was attached to the crystal. The phase relation between pump and control beam determines the orientation of the squeezing ellipse relative to the control beam [34]. A PZT attached to a mirror was used to lock this phase. If we lock to the bright fringe i.e to the amplification, results in phase squeezing and if we lock it to de-amplification results in ampitude squeezing as discussed in fig. 1.4 of chapter 1. The error signal for locking the phase of the control beam and pump was phase shifted by $\frac{\pi}{2}$. The squeezing phase is locked to the de-amplification by sending the error signal to the PZT attached as shown in fig. 3.9. A Dichroic beam splitter (DBS) was used at the output of the squeezed source to reflect the 1064 nm and to not allow any 532 nm to be injected into the interferometer. The output of the squeezer cavity contains a displaced squeezed state with displacement provided by the control beam. This control beam can be seen as DC

field, which carries the information of the sidebands (36.5/37.22MHz) from the squeezer to the interferometer and it perfectly overlaps spatially to the generated squeezed light at 1064nm. Hence, in general, it is used as an aligning tool for adjusting the spatial beam of the power recycling interferometer mode and the squeezed beam. Since the squeezed output is very sensitive to losses, very high reflective turning mirrors (R≈ 99%) were used to inject into interferometers.

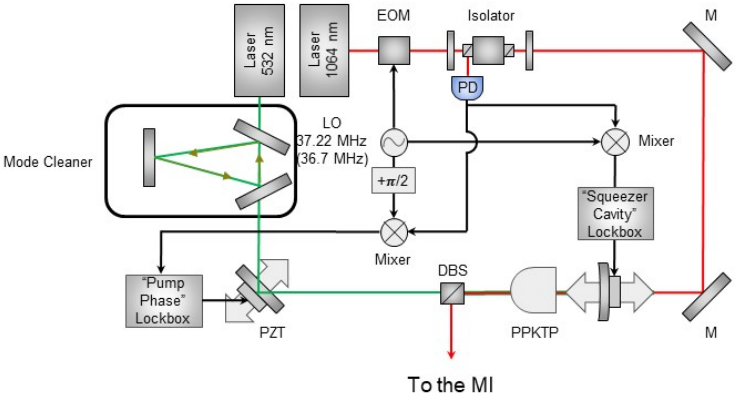

(i) Squeezed light generation

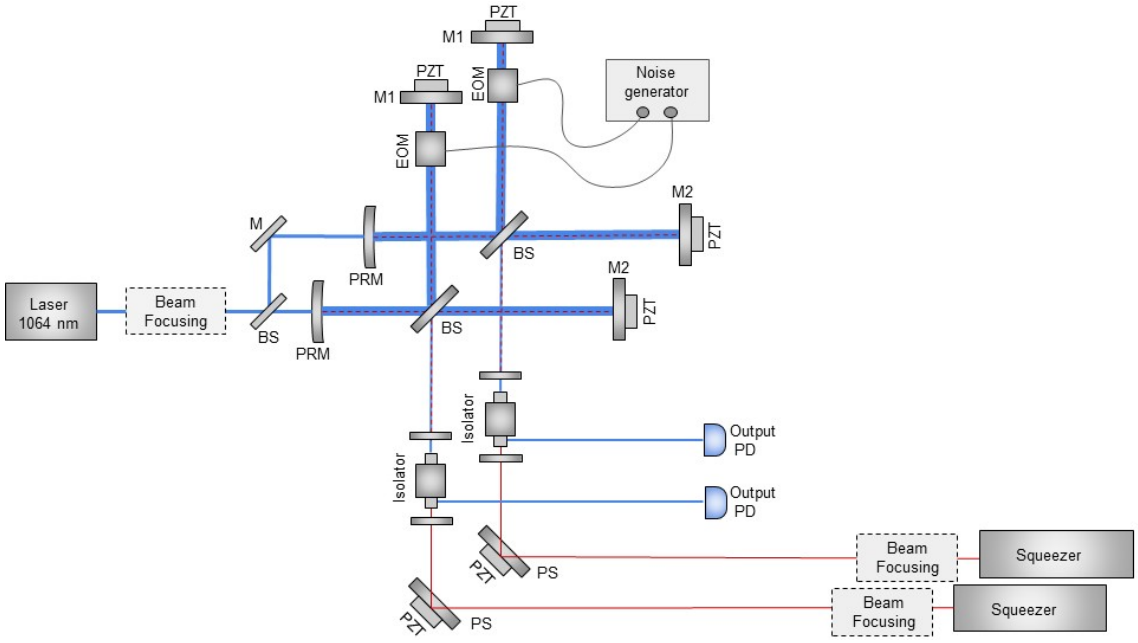

(ii) Double Squeezer injection

Figure 3.9: (i) Experimental setup of each Squeezer: PPKTP: potassium titanyl phosphate crystal. DBS: dichroic beam splitter. PZT: piezoelectric actuators. EOM: electro-optical modulator. LO: local oscillator. PD: photo-diode, (ii)Injection of Squeezed light source from each squeezer into each interferometer.

3.3.2 Mode Matching

For modematching the power recycling TEM_{00} interferometer output to the output squeezed light a reverse injection of interferometer mode was done into the squeezer cavity. Appropriate lenses were used, as calculated in section 2.2.3, to improve the mode-matching between the interferometer output mode and squeezed light mode. The PZT attached to the transperent mirror of the squeezing cavity is scanned and modes of the cavity are observed. The TEM_{00} mode was enhanced by adjusting the turning mirrors placed for aligning the squeezed light to the interferometer. The mode-matching obtained was around 99%.

3.3.3 Quantum Noise Locking

The fig. 3.10 depicts the complete locking scheme for each interferometer. Initially the interferometer is locked near to the dark fringe as described in section 3.2.1. The squeezed light after it passes through DBS is injected into the interferometer. The squeezed light together with the control beam having an output power maintained at 5 μW enters the interferometer. As stated previously, the control beam carries the information of 37.22 MHz/36.5 MHz when it enters the interferometers. When the squeezed light enters the interferometer, the DARM photodetector is demodulated at 37.22 MHz/36.5 MHz with an inbuilt mixer as discussed in section 3.2. The error signal is generated such that the point of squeezing quadrature corresponds to the maximum slope part of the error signal. The interferometer is then locked to the squeezing quadrature by help of a phase shifter with PZT attached.

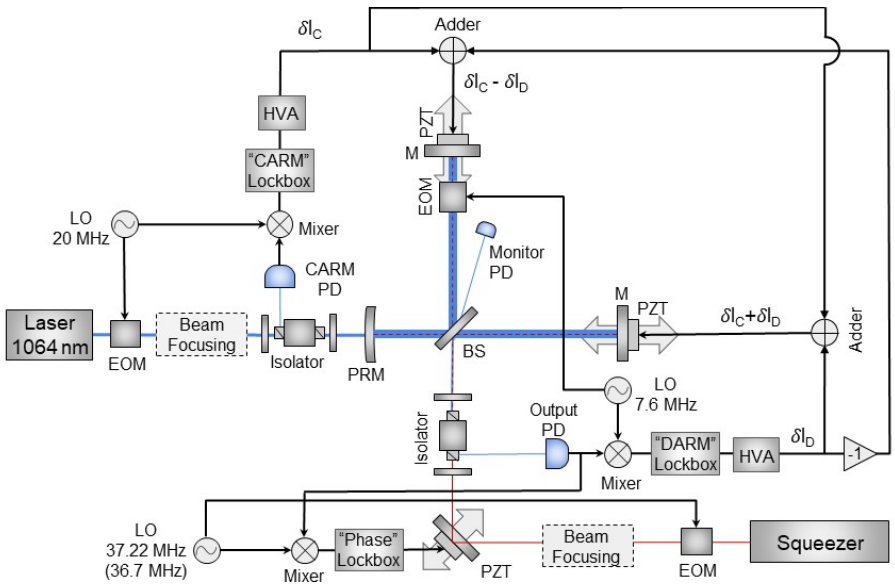

(i) Complete locking scheme of the interferometer

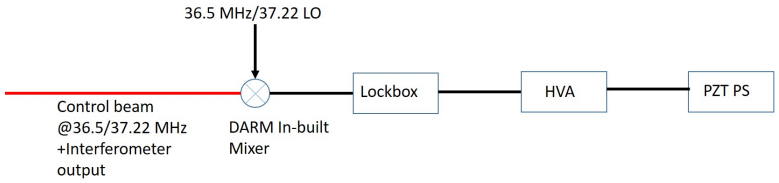

(ii) Locking connections for the quantum noise locking

Figure 3.10: (i)Locking scheme of each interferometer including Squeezer: PZT: piezo-electric actuator. EOM: electro-optical modulator. HVA: high-voltage amplifier. LO: local oscillator. PD: photo-diode PS: Phase Shifter (ii) Pictorial representation of locking connections for stabilizing the interferometer to the squeezing quadrature.

3.4 Twin Beam like State

As we have discussed in Chapter 1 in section 1.3.3 the twin beam state is entangled in number of photons and presents also non classical quadrature correlations between the two optical modes. Although photon number entanglement would provide in principle a dramatic enhancement of the sensitivity, as discussed in Section 1.5.3, its practical realization is extremely challenging. On the other side exploiting non-classical quadrature correlations is definitely feasible with some slight modification of the previous step.

3.4.1 Generation of Twin Beam State

We use an approximate twin-beam-like state in our experiment as described in Chapter 1. It is generated by splitting a single mode squeezed vacuum state on a beam splitter as discussed in section 1.3.3. Each mode of the splitted state is then sent to each interferometer. The variance of difference of the output signal of two interferometers is then measured. The fig. 3.11 represents the experimental scheme of the Twin Beam state injected in the double interferometric system. The quantum noise locking is similar to that of the double

squeezer setup in fig. 3.10. Since the single mode squeezer is split. each mode of twin beam has a some amount of control beam field associated with it, which carries the information of the sidebands at 36.5MHz. The error signal at the DARM photodetector is then demodulated at 36.5 MHz with the in-built mixer and is sent to each of the phase shifter for locking.

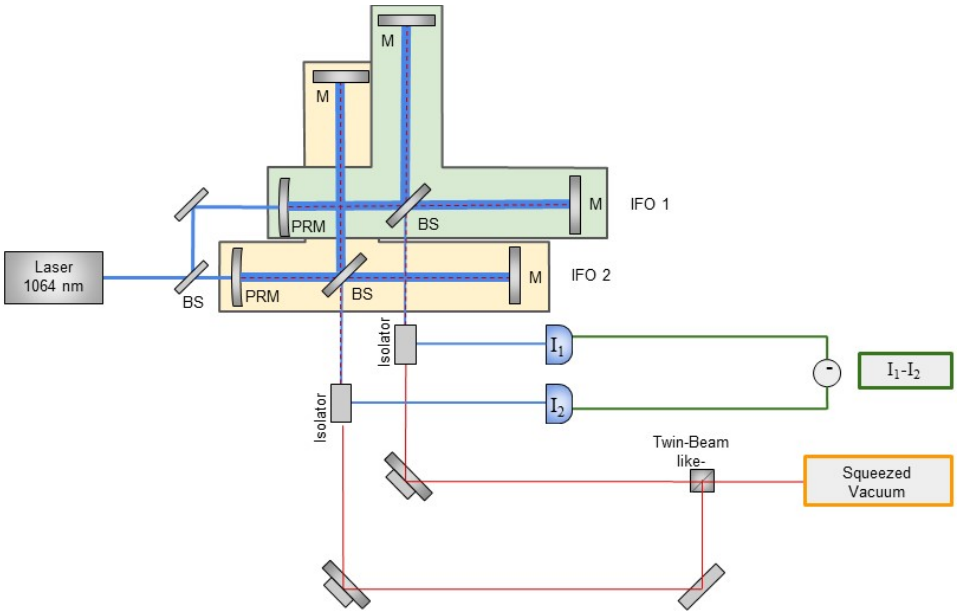

Figure 3.11: Twin Beam -like configuration: The squeezed light from the squeezer is split and each mode is sent to each interferometer.

3.5 Chapter Summary

A detail description of both classical and quantum part of the experimental setup have been presented in this chapter. Important measurements such as visibility, characterization of power recycling fringe have been described. Generation of squeezed light and twin beam like state using parametric down conversion has been discussed. The locking schemes used for stabilizing the interferometer and stabilizing the phase of interferometer to phase of the squeezing have been presented as well.

CHAPTER 4

SHOT NOISE AND SENSITIVITY

4.1 Introduction

As we have discussed in section 1.3.1 of Chapter 1, the fundamental limit to the optical intensity noise for the classical light is known as shot noise. As the standard deviation measured of the number of photons N at detector in a given interval goes as $\sqrt{N}$, which is in turn proportional to $\sqrt{P}$, P being optical power used for the incident light. Usually for a laser, the intensity noise is shot noise limited at higher frequencies while the lower frequencies are dominated by mechanical noise ,thermal noise and other source of noises. Similarly, as discussed in section 1.4.1, this shot noise limit propagates inside the interferometers and the unceratinty in phase is proportional to $\frac{1}{\sqrt{P}}$. When measured by a photodetector, usually intensity is measured in V and the shot noise limit is evaluated in units of $V/\sqrt{Hz}$, which should be eventually converted into $m/\sqrt{Hz}$ for evaluation of displacement sensitivity. In section 4.2 we discuss the results of shot noise measurements. In section 4.3 we discuss the experimental evaluation of sensitivity in $m/\sqrt{Hz}$.

4.2 Shot Noise limit

The light incident from the laser at a certain frequency is shot noise limited only if the variance of the time series obtained on a photodetector at that frequency scales proportionally with optical DC power (which is proportional to number of photons). Similarly in the frequency domain, the *power spectral density* (PSD) is evaluated, which describes how the power of a certain signal is distributed with respect to the frequency. It is defined as the Fourier transform of the auto-correlation of the time series. Let $X(t)$ be a stationary signal, then the auto correlation function $R_{xx}(\tau)$ given by:

$$R_{xx}(\tau) = \langle X(t)X(t+\tau)\rangle \tag{4.2.0.1}$$

It can be seen that $R_{xx}(0)$ provides us the variance of the time series.

The power spectral density is hence defined as,

$$S_{xx}(\omega) = \int_{-\infty}^{\infty} R_{xx}(\tau) e^{-2\pi j\omega\tau} d\tau \tag{4.2.0.2}$$

While in the discrete form for a time series of length N and sampling frequency F_s, the PSD can be written as[59],

$$S_{xx}(\omega) = \frac{1}{NF_s} \sum_{n=0}^{N} R_{xx}(n) e^{-2\pi j\omega n} \tag{4.2.0.3}$$

where $R_{xx}(n) = \langle x(m)x(m+n)\rangle$, x (m) being the m^{th} element of the time series X. The units of PSD are expressed in $\frac{V^2}{Hz}$. However, in our system, the power spectral density is evaluated using Welch's method which is discussed in Appendix D.

The mathematical form of shot noise evaluated in frequency domain is similar to white noise which has equal intensities in a given bandwidth. Similarly in time domain, when we evaluate the auto-correlation function for shot noise limted time series, has a non-zero value at $\tau = 0$ and is zero $\forall\ \tau \neq 0$. Hence we can write the PSD $S_{xx}(\omega)$ as,

$$S_{xx}(\omega) = \frac{1}{2\pi} \int_{-\infty}^{\infty} R_{xx}(0) e^{-2\pi j\omega\tau} d\tau \tag{4.2.0.4}$$

Taking the inverse Fourier transform for the equation (4.2.0.4), we get

$$R_{xx}(0) = \frac{1}{2\pi} \int_{-\infty}^{\infty} S_{xx}(\omega) e^{-2\pi j\omega\tau} d\omega \tag{4.2.0.5}$$

For a given bandwidth $\Delta\omega$, we can write $R_{xx}(0)$ as

$$R_{xx}(0) = \frac{1}{2\pi} S_{xx} \Delta\omega \tag{4.2.0.6}$$

Hence the Variance of the shot noise is proportional to the evaluate Power Spectral density for shot noise limited cases. Hence for shot noise limited cases, in the frequency domain since the power spectral density is related to the variance, should also scale with optical DC power.

4.2.1 Data acquisition

As we have mentioned in section 3.2, the photodetector had two 100kHz high passed outputs. One of the AC output was used for locking the interferometer while another AC output was used for measurement. This AC output was down mixed at 13.5MHz, pre-amplified and low passed at 100kHz as shown in fig. 4.1. Then it is further sent to a 14 bit Data acquisition system which consists of 4 channels (2 for each interferometer). The sampling rate set was 500kS/s.

Ground loops are an important problem, which occur in electronics arise when we have different source of grounds between the electronics which causes to have a potential between them. These produces unwanted resonances at MHz frequencies and shoot up the variance of the time-series. To avoid unnecessary ground loops, all the power supplies

of the electronics used were connected to a single power strip in order to have a common ground source.

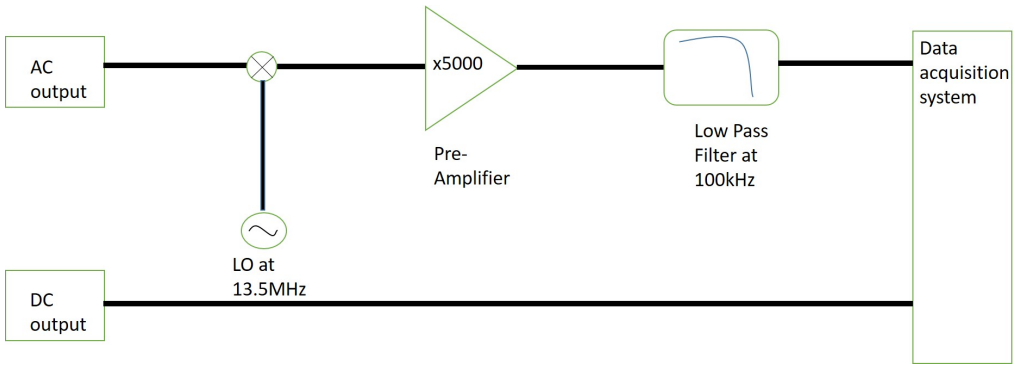

Figure 4.1: The figure above depicts the Data Acquisition system. The AC output which was down mixed at 13.5MHz along with DC-output was sent to the Data Acquisition card.

Shot Noise scaling

The laser optical power was controlled with help of half waveplate and Faraday isolator and was incident on a photodiode as shown in fig. 4.2. The input power was measured with a power meter to calibrate the conversion from voltage to watt in DC. The DC value and down mixed output at 13.5MHz were recorded together on the data acquisition system. It is known that for coherent states, as discussed in chapter 1 that the variance is

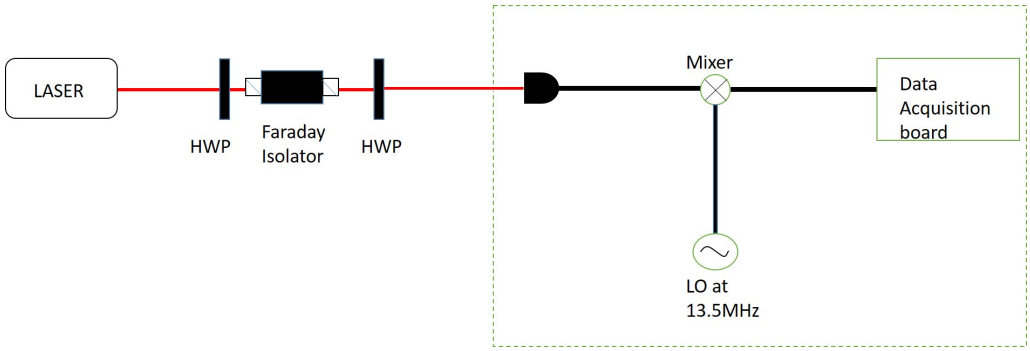

Figure 4.2: The figure above depicts the scheme of how the $\sqrt{P}$ was verified for the laser.

proportional to the mean number of photons (which is proportional to the optical power P). At the varying of the optical power, the variance of the time series after down mixing was evaluated. Figure 4.3 shows the variance normalized by the one at the smallest recorded power of $100\mu W$. The theoretical variances is expected to be proportional to the normalized optical power as:

$$\frac{\mathrm{var}(X_P)}{\mathrm{var}(X_{P_R})} = \frac{P}{P_R} \tag{4.2.1.1}$$

where X_P is the time series of the down-mixed output corresponding to optical power P , X_{P_R} corresponds to the time series of optical power corresponds to smallest recorded power P_R which in our case is $100\mu W$. It can be seen from the plot in fig. 4.3 that the mean value of variance start to deviate at $780\mu W$.

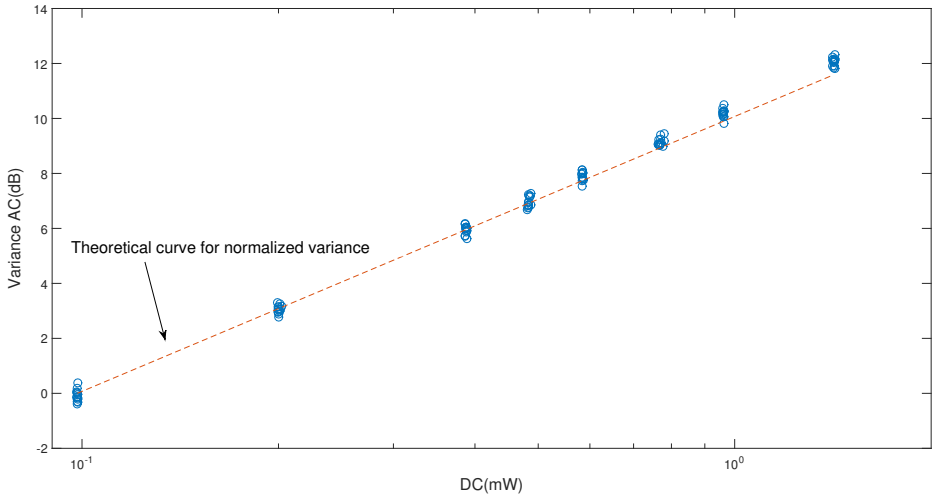

Figure 4.3: The Normalized variance plotted against input optical power of the laser. The red dashed line represents the theoretical prediction for the normalized variance. It can be seen that the laser is shot noise limited until around $600\mu W$.

The shot noise scaling has also been obtained in spectral domain by evaluating the PSD. Figure 4.4 depicts the normalized power spectral density to the power spectral density evaluated. It can be seen from the fig. 4.4, at 13.5 MHz the maximum output power that was shot noise limited was around 600μW.

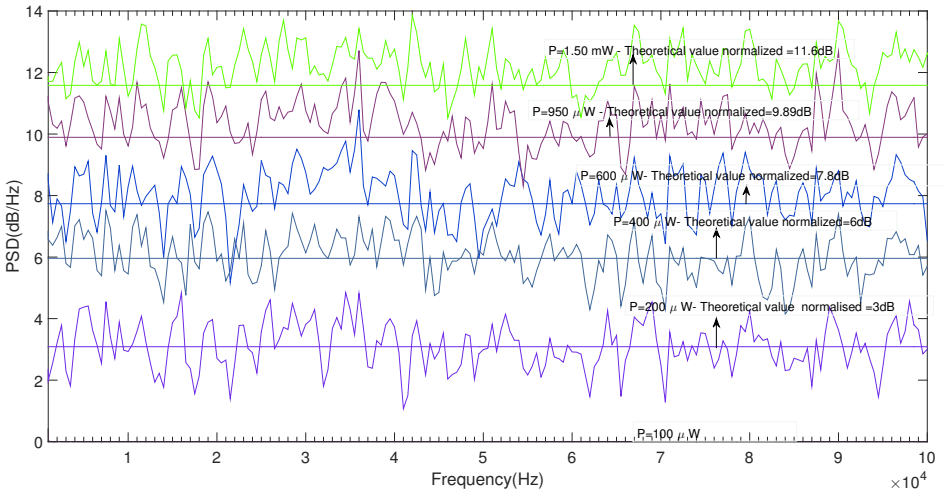

Figure 4.4: The Normalized PSD plotted against input optical power of the laser. It can be seen that the laser is shot noise limited until around $600\mu W$. The theoretical value normalized in the plot are obtained from the equation (4.2.1.1)

Similarly, for the power recycling interferometer, the shot noise scaling for output power of the interferometer should be verified. This was done by locking the interferometer close to the dark fringe as described in section 3.2.1, while the input power to the interferometer was varied . The shot noise scaling in both time domain as well as in frequency domain yields same results as in fig. 4.3 and fig. 4.4 being shot noise limited until optical power

of $600\mu W$ at frequency 13.5MHz. This is expected because the interferometer act as an attenuator for the input light. Since we are locking it close to the dark fringe, the output of the interferometer is highly attenuated, for which the technical noise at higher frequencies becomes negligible with respect to the shot noise component. Hence we expect the same results as in case of scaling of the intensity noise as in fig. 4.2, unless the power recycling cavity provides some spectral filtering.

4.3 Shot Noise Sensitivity

The noise floor evaluated from PSD as in section 4.2, when converted from V^2/Hz to strain spectral density in $m/\sqrt{Hz}$ is often referred to as the Displacement Sensitivity. As stated previously in the introduction, at higher frequencies this noise floor is limited by shot Noise. In an ideal case for both power recycled Michelson interferometer and Michelson interferometer, the theoretical shot noise limit ΔX_{shot} is given by [39]:

$$\Delta X_{shot} = 2\sqrt{\frac{\hbar c\lambda}{\pi P_{BS}}} \tag{4.3.0.1}$$

where P_{BS} represents the optical power at the beam splitter.

However in practice , we have to consider the transmission losses, contrast defect and the quantum efficiency of the detector.

The shot noise limited sensitivity is dependent on the following parameters:

- The input power P_{in}
- The power recycling gain G as mentioned in section 2.4.1.
- The transmission efficiency η from the anti-symmetric port of the beam splitter to the photodetctor .

4.3.1 Theoretical Sensitivity

Let us re-consider the equation (3.2.3.3). As discussed in section 3.2.3 where P_{BS} can be written as $P_{BS} = P_{in}G$, ϵ being the contrast defect η is the transmission efficiency for a power recycled cavity.

$$P_{AS} = \eta P_{BS}(\frac{\epsilon}{2} + (1-\epsilon)sin^2(k\Delta X_{offset})) \tag{4.3.1.1}$$

The strain sensitivity is given by,

$$\Delta X_{rms} = \frac{d(\Delta X_{offset})}{dP_{AS}}\Delta P_{AS} \tag{4.3.1.2}$$

The term ΔP_{AS} is called as the Amplitude spectral density. If the Amplitude Spectral density is shot noise limited, then ΔP_{AS} can be evaluated as:

$$\Delta P_{AS} = \Delta n_{AS}\hbar\omega \tag{4.3.1.3}$$

where n_{AS} is the number of photons exiting the anti-symmetric port. For shot noise limited case, since $\Delta n_{AS} = \frac{1}{\sqrt{n_{AS}}}$ we can evaluate ΔP_{AS} as,

$$\Delta P_{AS} = \sqrt{\frac{hc}{\lambda} P_{AS}} \tag{4.3.1.4}$$

Therefore we can evaluate the shot noise limited strain sensitivity,for the conditions that we operate the interferometer near to the dark fringe and for a low contrast defect ($\Delta X_{offset} \approx 0; \epsilon \approx 0$) as,

$$\Delta X_{shot} = \frac{1}{2\pi} \sqrt{\frac{hc\lambda}{\eta G P_{in}}} \tag{4.3.1.5}$$

4.3.2 Experimental estimation of sensitivity from the phase modulator

As we have discussed in section 3.2, we have a phase modulator placed inside the interferometer. The experimental strain sensitivity could be obtained by evaluating the strain caused by the phase modulator. When a certain voltage V is applied to the phase modulator, the equivalent strain caused by the phase modulator is given by [60],

$$\Delta X_{rms} = \frac{\lambda V_{rms}}{2V_{\pi}} \tag{4.3.2.1}$$

where V_{π} is the half wave voltage of the EOM.

The half wave voltage is defined as the voltage required for inducing a phase shift of π. In the next subsection 4.3.2 we discuss about the evaluation of V_{π}. In order to evaluate the sensitivity, we can inject a single frequency signal or a white noise over a bandwidth. Let h be the height of the single frequency signal with respect to the noise floor as shown in fig. 4.5.

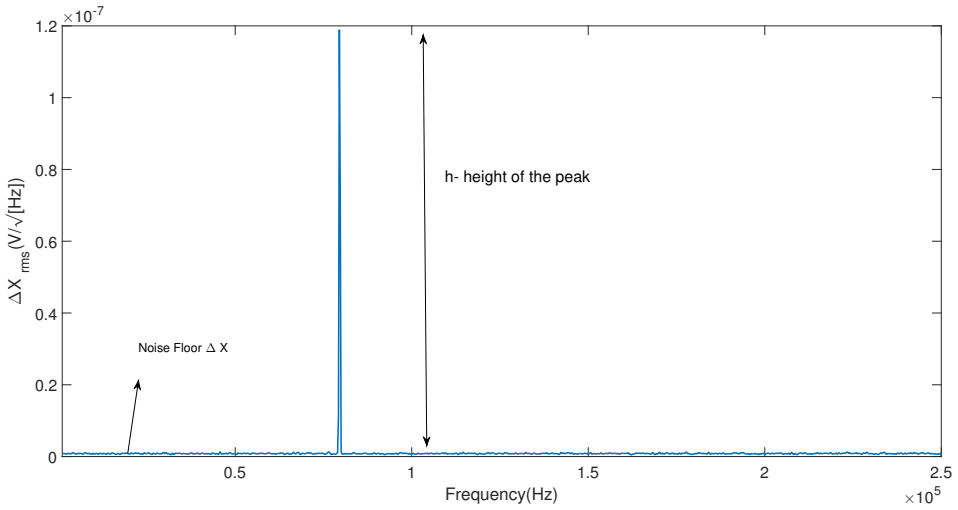

Figure 4.5: The above figure plots a PSD of a simulated linear spectral density of noise added to the single frequency signal at 100kHz

The sensitivity $(m/\sqrt{Hz})$ when a single frequency signal is given to the system can

then be evaluated by,

$$\Delta X_{rms} = \frac{\lambda V}{2V_\pi} = (\Delta X_{peak} - \Delta X)\sqrt{\Delta\omega} = \Delta X(h-1)\sqrt{\Delta\omega} \tag{4.3.2.2}$$

where ΔX is sensitivity evaluated in $m/\sqrt{Hz}$ and $\Delta\omega$ being the equivalent noise bandwidth (ENBW) evaluated accordingly in Appendix D. The above equation (4.3.2.2) can then be written as,

$$\Delta X(m/\sqrt{Hz}) = \frac{\lambda V}{2V_\pi\sqrt{\Delta\omega}(h-1)} \tag{4.3.2.3}$$

Similarly, when white noise is injected into the interferometer system with an input voltage V_{rms} measured in a resolution bandwidth $\Delta\omega$, the sensitivity $\Delta X(m/\sqrt{Hz})$ is evaluated by

$$\Delta X_{rms} = \frac{\lambda V}{2V_\pi\sqrt{\Delta\omega}} = n\Delta X - \Delta X \tag{4.3.2.4}$$

where n is the fraction of shot noise raised by white noise injection. Hence the sensitivity of the interferometer ΔX is given by

$$\Delta X = \frac{\lambda V}{2V_\pi\sqrt{\Delta\omega}(n-1)} \tag{4.3.2.5}$$

Evaluation of V_π

As we have discussed in the above section 4.3.2, it is necessary to evaluate the V_π for the evalution of the sensitivity. Usually the half wave voltage depends on the length of the crystal L and the thickness of the RTP crystal of the EOM d. Theoretically, it is given by [43]

$$V_\pi = \frac{\lambda L}{r_{13}n_0^3 d} \tag{4.3.2.6}$$

where r_{13} is called the electro-optic coefficient and n_0 is the refractive index of the material.

However, we can evaluate the V_π operating the interferometer in a standard, not power recycling, modality, by simply misaligning the power recycling mirror. As we have discussed in section 2.3, the distance between the maximum and minimum of the fringe is $\lambda/4$. This corresponds to a phase shift of $\pi/2$.

Firstly, the maximum and minimum values of the voltage were recorded by giving a modulation to the PZT of the mirrors. For the two interferometers the maxima were estimated to be 1.88V and 3.12V respectively for both interferometers. Then, a ramp function was induced with a function generator with frequency of 1kHz and high voltage amplifier (HVA) to the EOM and the trace of the fringe is recorded with the photodetector on the oscilloscope as shown in fig. 4.6.

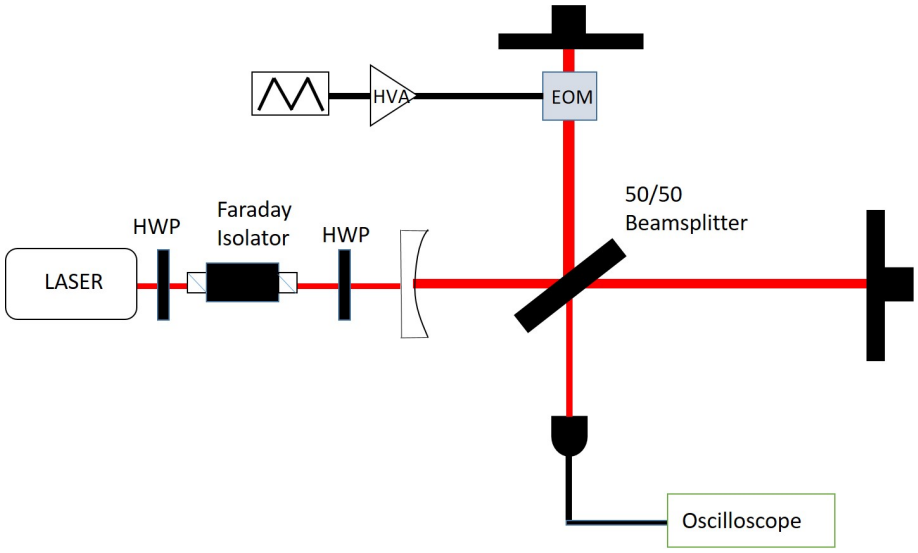

Figure 4.6: The figure above depicts the experimental scheme of how the V_π was evaluated. A ramp function was induced to the EOM at 1kHz frequency and fringe of the interferometer was traced out such that the curvature of the bright portion of the fringe seen.

Since the DARM locking bandwidth is larger than 1 kHz, this measurement must be done without locking the interferometer, because otherwise it would compensate for the fluctuation induced by EOM. However, it was necessary to temporally operate at the bright fringe of the interferometer as described in [61] so that the curvature of the fringe trace could be seen. This is done by a properly tuning the DC voltage to the PZT actuators. Then the voltage, at the antisymmetric port V_{AS} is fitted with equation:

$$V_{AS} = \frac{V_{max}}{2}\left(1 + \eta_0.\cos(\frac{2\pi V_{in}}{V_\pi} + b)\right) \tag{4.3.2.7}$$

where η_0 is the insertion loss caused by the EOM, V_{max} is the voltage output when it is at the bright fringe , V_{in} is the ramp voltage given to the EOM.

The V_π calculated from the fits were (988 ± 7) V and (1000 ± 11) V for both the phase modulators placed in each interferometer respectively. The estimate of the V_{max} obtained from the fit matches with V_{max} obtained by modulating the PZT. The fig. 4.7 shows the fitted V_{AS} curves against voltage given to the phase modulator for each interferometer.

It should be noted that since the input modulation to the EOM was given at 1kHz, the V_π evaluated above from the fit corresponds to the value at 1kHz. Since we are interested in evaluating the sensitivity at 13.5 MHz, we need to evaluate V_π at MHz frequencies, for which the transfer function of the EOM has to be evaluated. Since our detectors are high passed at 100kHz, we used a Thorlabs detector PDA10CF for the measurement which has response from DC-150MHz. The DARM of the interferometer was locked at mid position of the fringe using DC locking technique as described in subsection 2.3.2 while the phase modulator was probed with a network analyzer from frequencies across 1kHz-30MHz.

Since we lock the DARM, near the mid-position of the fringe where the trace of the fring is linear, the photodetector output voltage (V) at the anti-symmetric port can be approximated as,

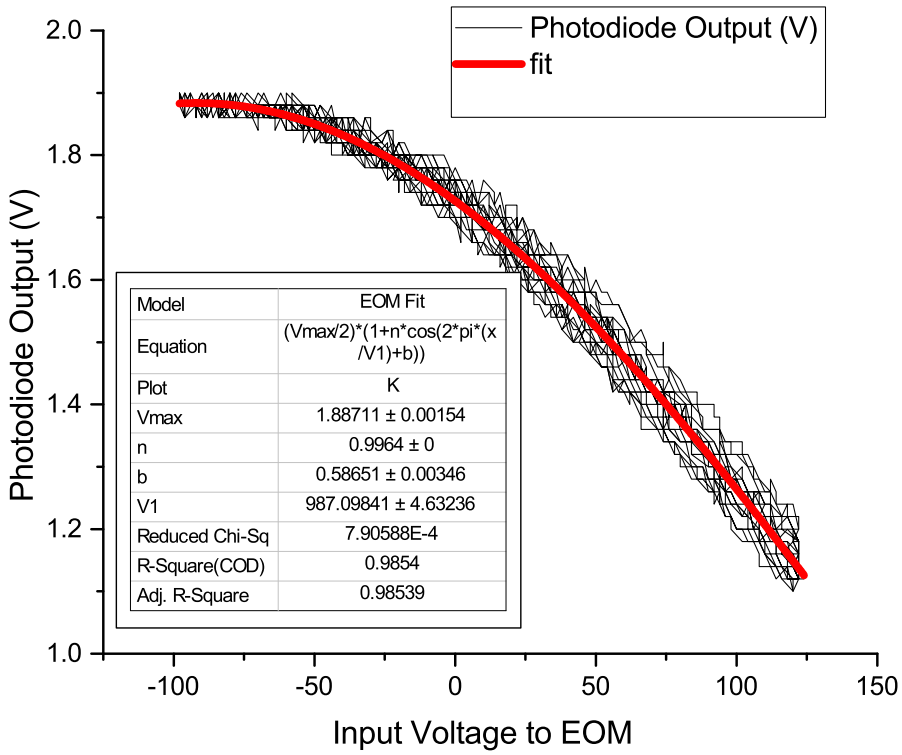

(i)

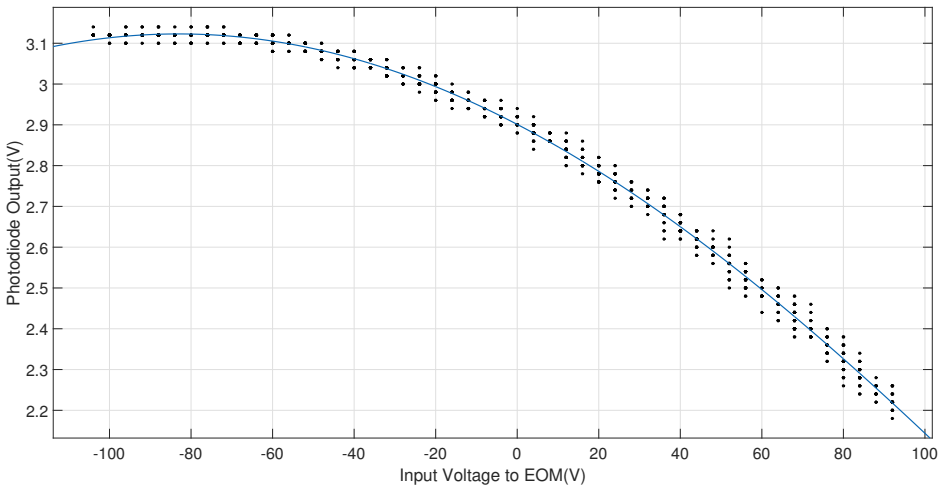

(ii)

Figure 4.7: Figures (i) and (ii) represents the fitted curves of photodetector output voltage V_{AS} against input voltage V to the EOM

$$V_{AS} \approx V_{max}\left(\frac{\eta_0 \pi V_{in}}{V_\pi}\right) \tag{4.3.2.8}$$

Hence in the frequency domain the $V_{AS}(\omega)$ is inversely proportional to $V_\pi(\omega)$

The photodetector response at all frequencies was recorded on the network analyzer as shown in fig. 4.8 (i). This measurement is known as S_{21} as the network analyzer measures the ratio of power at the anti-symmetric port to that of power given to the EOM at all frequencies. The fig. 4.8 (ii) and fig. 4.8 (iii) plots the evaluated S_{21} as a function of frequency. It can be seen that there was around 1.4dB drop at 13.5MHz in the transfer function with reference to the value at 1kHz.

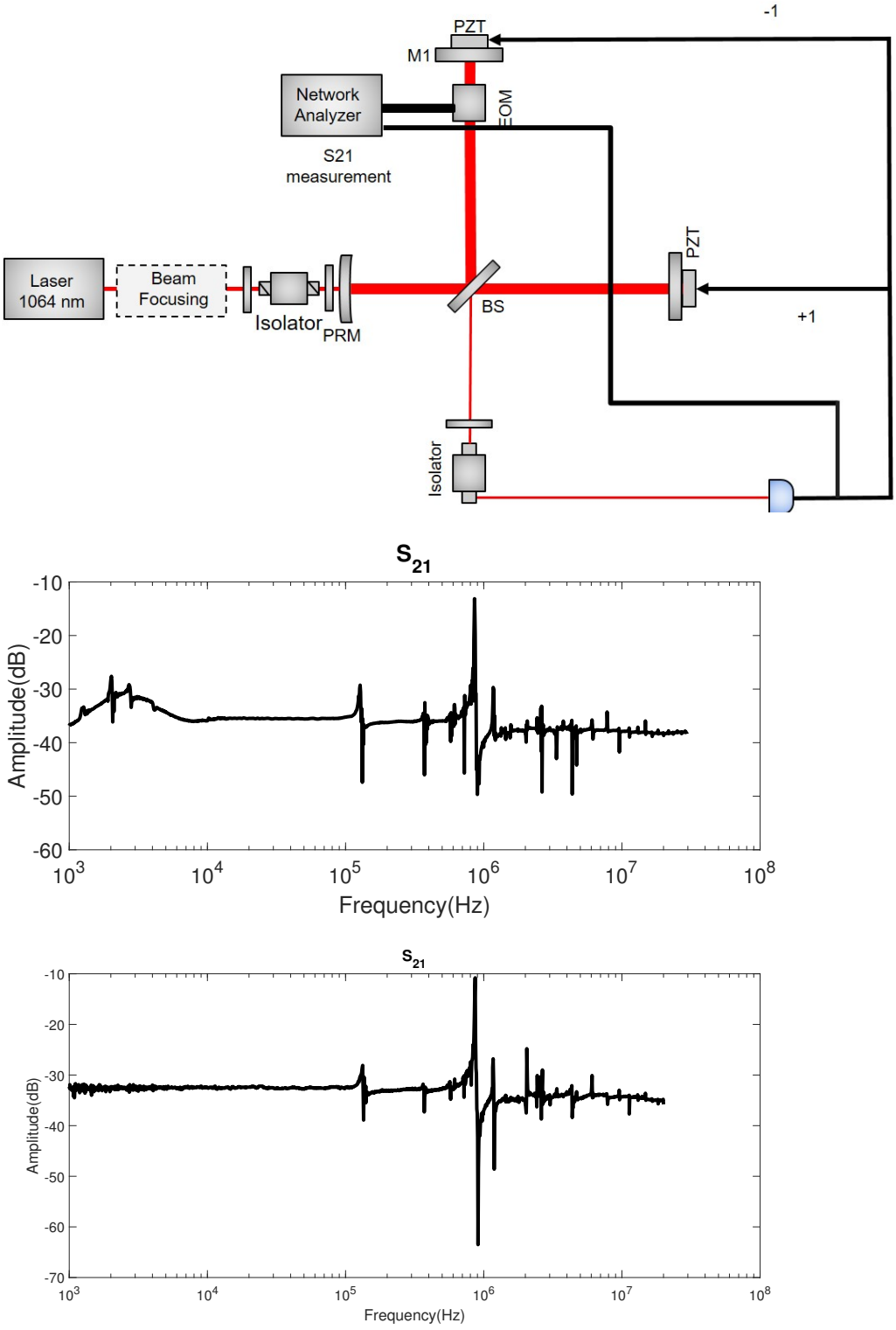

Figure 4.8: Figure (i) is the experimental scheme for performing S_{21} measurement. The DARM is locked using DC locking while the network analyzer probes the phase modulator placed inside the interferometer. Figures (ii) and (iii) represents the plots of S_{21} as a function of frequency.

It is also necessary to evaluate the transfer function of the photodetector used in the interferometer. The transfer function of the photodetector was evaluated with help of

fiber based amplitude modulator. The Amplitude modulator was probed with a network analyzer and the photodetector response was recorded at all frequencies. The fig. 4.9 plots the transfer function of the photodiode as a function of frequency. There is also a drop of 1.3dB at 13.5MHz in the transfer function evaluated for the photodetector with reference to 1kHz frequency.

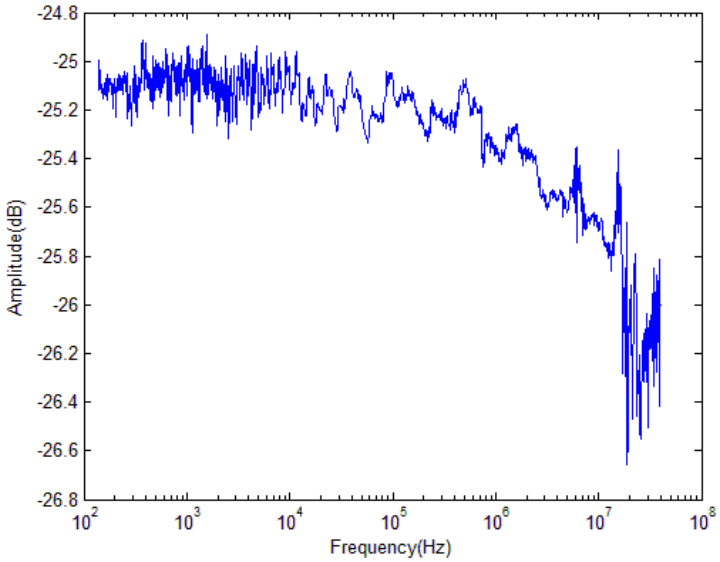

Figure 4.9: The S_{21} measurement of the photodetector plotted as a function of frequency

Hence we can evaluate $V_\pi(13.5\text{MHz})$ as

$$V_\pi(13.5\text{MHz}) = V_\pi(1\text{kHz})\left(\frac{S_{21,\,PD}(13.5\text{MHz})}{S_{21,\,PD}(1\text{kHz})}\frac{S_{21,\,EOM}(1\text{kHz})}{S_{21,\,EOM}(13.5\text{MHz})}\right) \tag{4.3.2.9}$$

where $S_{21,\,PD}$ corresponds to the evaluated transfer function of photodetector and $S_{21,\,EOM}$ corresponds to the evaluated transfer function of EOM. It was found that after applying above corrections of transfer function ,there was no change in V_π value at 13.5 MHz which was the desired frequency of measurement.

This information of evaluated V_π and discussion in section 4.3.2 would be used in the evaluating the displacement sensitivity, described in chapter 5.

4.4 Summary

We have discussed in details about shot noise measurements. Our laser is shot noise limited until $600\mu W$ of output power at 13.5 MHz frequency. We have also discussed in details of evaluation of theoretical sensitivity using the position of the fringe. We have experimentally evaluated the half wave voltage V_π which would be used for calculating the strain caused by the EOM in the interferometer. The experimental evaluation of displacement sensitivity can be established by calculating the equivalent strain caused by the EOM which is discussed in chapter 5.

CHAPTER 5

RESULTS WITH INDEPENDENT SQUEEZERS

5.1 Introduction

The effect of squeezing in single interferometers of reducing shot noise has already been demonstrated in large scale interferometers for detection of gravitational waves[36][23] as discussed in section 1.4.1. In section 1.5.1, we have described theoretically the results of the effect of two independent squeezed vacuum states when injected into the two interferometers and cross correlation between them is measured. In this chapter we present the experimental results we have obtained in that configuration.

5.2 Initial squeezing Evaluation

The squeezed light before entering the interferometers, was initially measured on a homodyne detector. In a homodyne measurement, the squeezed beam and local oscillator (LO) are interfered on a balanced beam splitter and the difference between the outputs is measured as depicted in fig. 5.1. As we have shown in section 1.3.2, this scheme allows to access the quadrature of the field.

The LO was made to pass through a mode cleaner and through a set of lenses to mode match the squeezed beam. The resulting mode matching was around 99%. Firstly the shot

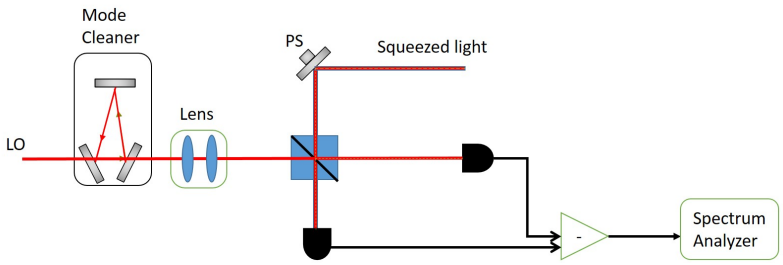

Figure 5.1: The figure above depicts the scheme of homodyne measurement. The squeezed beam and local oscillator are interfered. The phase is varied by a phase shifter and the subtracted output is sent to a spectrum analyzer.

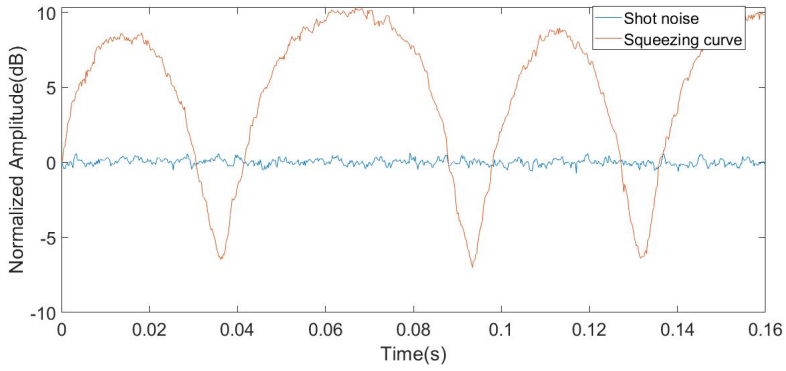

Figure 5.2: Initial squeezing measured before the interferometer via homodyne detection scheme in function of the phase shift between LO and the squeezed field. The blue line represents the shot noise level and the green curve represents the squeezing value with respect to the local oscillator.

noise of level is calibrated by performing the measurement with solely the LO, blocking the squeezed beam using the homodyne scheme at 13.5 MHz by a spectrum analyzer. Then, the squeezing was injected and homodyne measurement was performed. As we have shown in section 1.3.2, this corresponds to a change of phase of the measured quadrature, the fig. 5.2 shows the plot of squeezing as function of the phase shifter phase. The phase of the squeezing with respect to the LO was varied with a phase shifter (PS). The minima in the fig. 5.2 corresponds to the estimation of the noise in the squeezed quadrature ,V_{sqz} , while the maxima represent the measurement of the anti-squeezed one, $V_{anti-sqz}$.

By using equation (1.4.1.17), one can write the following relations:

$$\begin{aligned} V_{sqz} &= \eta_{mm}\eta V + (1 - \eta\eta_{mm}) \\ V_{anti-sqz} &= \frac{\eta\eta_{mm}}{V} + (1 - \eta\eta_{mm}) \end{aligned} \tag{5.2.0.1}$$

where $V = e^{-2r}$ is the amount of squeezing produced by the squeezer output ideally produced in the lossless scenario and η includes the transmission efficiency from the squeezer cavity to photodetector and η_{mm} is the mode-matching loss between the LO and the squeezed light. Introducing the measured value of V_{sqz} and $V_{anti-sqz}$ (6.5 dB and 10 dB respectively), in equations (5.2.0.1) allows estimating the the initial squeezing produced into the cavity and the loss component, independently. The amount of squeezing measured was around 6.5 dB with respect to shot noise level and anti-squezing measured was around 10dB. Since we know that $\eta_{mm} = 0.99$, we can evaluate the values of V and η using equation (5.2.0.1), which are given in the table 5.1:

V	0.0862
η	0.85

Table 5.1: Results of the parameters of V and η. The value of V gives us the initial squeezing produced by the squeezer which is around $10\log V = 10$dB

5.3 Squeezing in the interferometers

When we inject the squeezed light in each interferometer, the variance in single interferometers will be reduced by a factor of $\left(e^{-2r} + \frac{1-\eta_{loss}}{\eta_{loss}}\right)$, where η_{loss} includes all the losses such as detection losses of the photodiode, transmission losses due to isolators,losses due to other optics and losses due to mode-matching between the squeezed light and interferometer mode as demonstrated in chapter 1 of section 1.4.1.

Firstly, the output power of the interferometers were aimed to be maintained at $500\mu W$ for the interferometers to be shot noise limited at 13.5MHz as discussed in section 4.2.1. The AC output of the DARM photodetector was down mixed at 13.5MHz as mentioned in section 4.2.1 to measure the shot noise on the acquistion board. The squeezed output from the squeezer cavity was then injected to interferometers. For modulating the phase between the squeezed mode and the interferometer mode, a phase shifter was used to modulate the phase of the squeezer with respect to the interferometer as described in section 3.3.3

Figure 5.3 (i) depicts the shot noise level as a function of the phase of interferferometer. The interferometer was then locked to the squeezing quadrature using the quantum noise locking technique with the help of the phase shifter as mentioned in section 3.3.3. The fig. 5.3 (ii) depicts the interferometer locked to the squeezing quadrature. The data was recorded as shown in fig. 4.1 and PSD of the down mixed outputs were evaluated as described in Appendix D. There was around 2.5 dB and 3dB of squeezing observed in each of the interferometers.

The auto correlation $\rho_{11}(\tau)$ of the time series can also be defined as [59]:

$$\rho_{11}(\tau) = \mathrm{Cov}(X_1(t)X_1(t+\tau)), \tag{5.3.0.1}$$

At $\tau = 0$, the auto correlation function $\rho_{11}(0)$ should be equal to variance of the time series X_1. The fig. 5.4 depicts the plot of evaluated auto-correlation of each interferometer in both classical and squeezed light injected cases. It can be seen that the height of the peak reduces by 3dB and 2.5dB respectively at delay $\tau = 0$ when the squeezed light is injected.

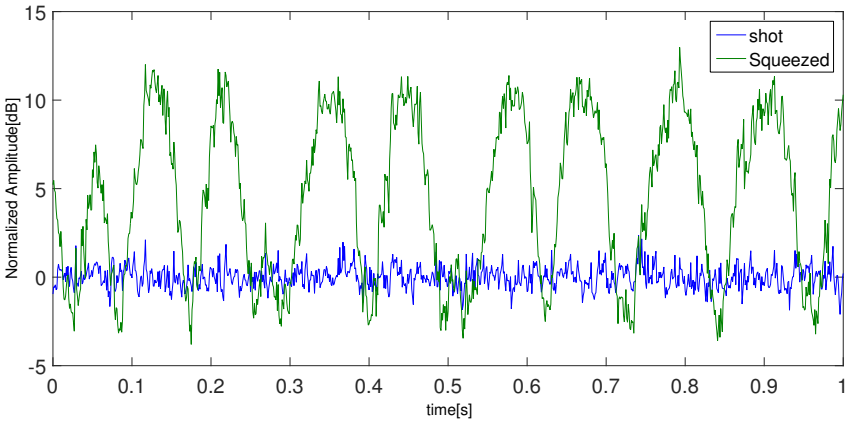

(i)

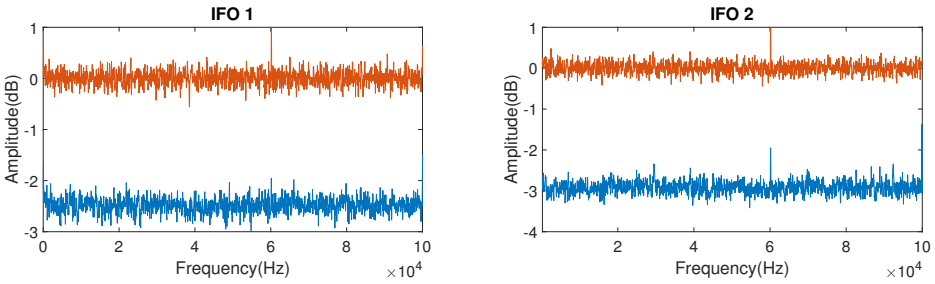

(ii)

Figure 5.3: (i)The plot represents normalized shot noise as a function of phase between the squeezer and the interferometer recorded on a spectrum Analyzer. The blue curve represents the Shot noise level and the green curve represents the squeezed injected shot noise fluctuations (ii) The plot represents the locked squeezed quadrature. Around 2.4dB and 3dB of squeezing was observed for each interferometers

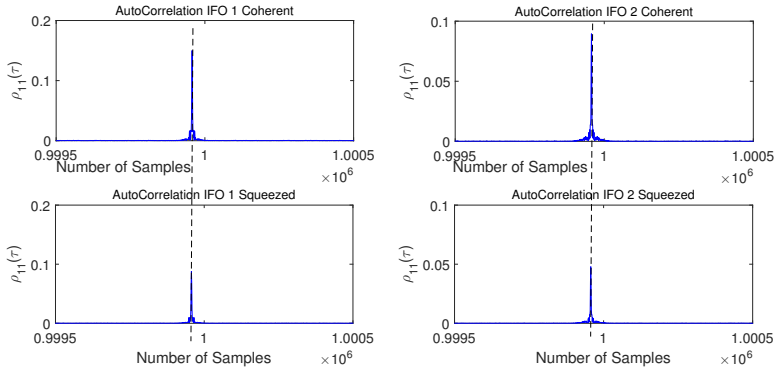

Figure 5.4: The figure above plots the auto-correlation in both cases of classical and squeezed light individual cases. It can be seen that the height of peak reduces when the squeezed light is injected.

5.4 Correlation in Time domain

We have performed the experiment in three different cases:

(i) with correlated white noise injected (ii) with uncorrelated white noise injected (iii) with no noise injected (limited by shot noise)

But we concentrate mainly on the measurements with injection of correlated white noise as it encompasses the discussion of all the three cases.

5.4.1 Measurements with Injection of Correlated white noise

Temporal Cross Correlation

As we have discussed in section 1.5.1, when we use the double squeezer setup, the cross correlation between the outputs of the interferometer is performed. As stated in section 3.2 white noise was injected with the help of the phase modulators placed inside the arms of the two interferometer.

As a first approximation the ouput signal of the j^{th} inferferometer, $X_j(t)$, is given by the sum of the photon noise fluctuation $X_{JSN}(t)$ and the photocurrent fluctuation induced by the injected white noise $X_{jWN}(t)$. Thus, the variance of the interferometer output signals is given by:

$$\begin{aligned} \mathrm{var}(X_1) &= \mathrm{var}(X_{1SN}) + \mathrm{var}(X_{1WN}) \\ \mathrm{var}(X_2) &= \mathrm{var}(X_{2SN}) + \mathrm{var}(X_{2WN}) \end{aligned} \tag{5.4.1.1}$$

Similarly, the covariance could be written as,

$$\mathrm{Cov}(X_1, X_2) = \mathrm{Cov}(X_{1SN}, X_{2SN}) + \mathrm{Cov}(X_{1WN}, X_{2WN}) \tag{5.4.1.2}$$

Then the variance of the difference between the two output time series is evaluated as,

$$\mathrm{var}(X_1 - X_2) = \mathrm{var}(X_1) + \mathrm{var}(X_2) - 2\mathrm{Cov}(X_1, X_2) \tag{5.4.1.3}$$

The cross correlation function $R_{12}(\tau)$ between the two output time-series of the interferometers X_1 and X_2 is defined as

$$R_{12}(\tau) = \mathrm{Cov}(X_1(t), X_2(t+\tau)) = \langle X_1(t) X_2(t+\tau) \rangle \tag{5.4.1.4}$$

Using equtaion (5.4.1.2) we can write the cross correlation function as,

$$R_{12} = \mathrm{Cov}(X_1(t), X_2(t+\tau)) = \mathrm{Cov}(X_{1SN}(t), X_{2SN}(t+\tau)) + \mathrm{Cov}(X_{1WN}(t), X_{2WN}(t+\tau)) \tag{5.4.1.5}$$

Since photon noises of two interferometers are uncorrelated, the first term $\mathrm{Cov}(X_{1SN}(t), X_{2SN}(t+\tau))$ in equation (5.4.1.2) is negligible and the second term $\mathrm{Cov}(X_{1WN}(t), X_{2wN}(t+\tau))$ emerges out at $\tau = 0$ depending on the strength of the signal injected and number of samples acquired. Hence, when we performed the cross-correlation between the two time-series, the phase between the two electronic local oscillator between the down-mixed outputs were adjusted such that the peak emerging from the correlation

was maximized as shown in fig. 5.5. The sampling rate set was around $500kS/s$ and the total acquisition time was around 1s.

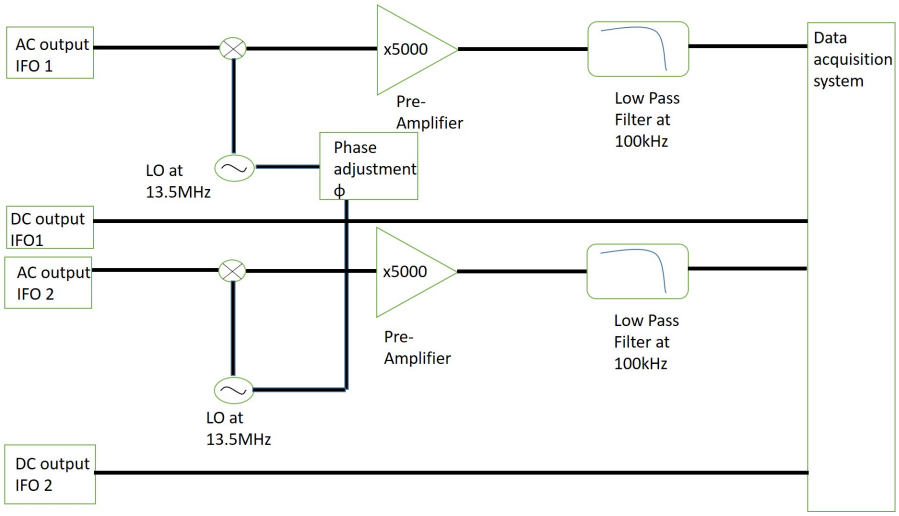

Figure 5.5: The figure above represents the scheme of data acquisition for both the interferometers. The phase between the two electronic local oscillator between the down-mixed outputs were adjusted to maximize the peak.

As a figure of merit, for quantifying this cross correlation, we consider the cross correlation normalized to shot noise of each interferometer. The normalized cross correlation coefficient $\rho_{12}(\tau)$ is defined as

$$\rho_{12}(\tau) = \frac{|R_{12}(\tau)|}{\sqrt{\text{var}(X_{1SN}(t))\text{var}(X_{2SN}(t))}} \ , \tag{5.4.1.6}$$

where $X_{1SN}(t)$ ($X_{2SN}(t)$) is the time series of the read-out signal of the first (second) interferometer recorded in the coherent case and τ is the time delay between the two timeseries. Let us consider the case of coherent light in both interferometers. The above equation (5.4.1.6) can be written as,

$$\begin{aligned} \rho_{12}(\tau) &= \frac{|R_{12}(\tau)|}{\sqrt{\text{var}(X_{1SN}(t))\text{var}(X_{2SN}(t))}} \\ &= \frac{|\text{Cov}(X_1(t)X_2(t+\tau))|}{\sqrt{\text{var}(X_{1SN}(t))\text{var}(X_{2SN}(t))}} \\ \rho_{12}(\tau) &= \frac{|\text{Cov}(X_{1SN}(t)X_{2SN}(t+\tau))| + |\text{Cov}(X_{1WN}(t)X_{2WN}(t+\tau))|}{\sqrt{\text{var}(X_{1SN}(t))\text{var}(X_{2SN}(t))}} \end{aligned} \tag{5.4.1.7}$$

It should be noted that in above equation (5.4.1.7) as we consider the absolute value of the covariance of the two interferometers for the normalized cross correlation, we have a non-zero value for the $\langle|\text{Cov}(X_{1SN}(t)X_{2SN}(t+\tau))|\rangle$.

Figure 5.6 depicts the evaluated normalized cross correlation in time domain for the coherent case using equation (5.4.1.6) as a function of the number of samples. To quantify the background floor of the noise as a function of the number of samples, let us evaluate the quantity $\text{var}(\rho_{12}(\tau))$.

$$\begin{aligned}\operatorname{var}(\rho_{12}(\tau)) &= \left\langle \rho_{12}(\tau)^2 \right\rangle - \langle \rho_{12}(\tau) \rangle^2 \\ &= \frac{1}{\langle \operatorname{var}(X_{1SN}(t)) \rangle \langle \operatorname{var}(X_{2SN}(t)) \rangle} (\left\langle \operatorname{Cov}^2(X_1(t), X_2(t+\tau)) \right\rangle - \langle \operatorname{Cov}(X_1(t), X_2(t+\tau)) \rangle^2\end{aligned} \tag{5.4.1.8}$$

Let us try to evaluate $\left\langle \operatorname{Cov}^2(X_1, X_2) \right\rangle$, it can be written as following:

$$\begin{aligned}\left\langle \operatorname{Cov}^2(X_1, X_2) \right\rangle &= \frac{1}{N^2} \sum_{i,j} \langle X_{1i} X_{2i} X_{1j} X_{2j} \rangle \\ &= \frac{1}{N^2} \sum_{i=j} \left\langle X_{1i}^2 X_{2i}^2 \right\rangle + \frac{1}{N^2} \sum_{i \neq j} \langle X_{1i} X_{2i} \rangle \langle X_{1j} X_{2j} \rangle \\ &= \frac{1}{N^2} \left[N \left\langle X_1^2 X_2^2 \right\rangle + N(N-1) \langle X_1 X_2 \rangle^2 \right] \\ &= \frac{\left\langle X_1^2 X_2^2 \right\rangle}{N} + (1 - \frac{1}{N}) \langle X_1 X_2 \rangle^2 \ ,\end{aligned} \tag{5.4.1.9}$$

where N represents the number of samples.

Thus the variance of the normalized cross correlation, using equation (5.4.1.9) could be evaluated as,

$$\begin{aligned}\operatorname{var}(\rho_{12}(\tau)) &= \frac{\left\langle \operatorname{Cov}^2(X_1, X_2) \right\rangle - \langle X_1, X_2 \rangle^2}{\operatorname{var}(X_{1SN}) \operatorname{var}(X_{2SN})} \\ &= \frac{\operatorname{var}(\operatorname{Cov}(X_1, X_2))}{N \operatorname{var}(X_{1SN}) \operatorname{var}(X_{2SN})}\end{aligned} \tag{5.4.1.10}$$

Hence the width of the noise floor (standard deviation of the $\rho_{12}(\tau)$) scales inversely proportional to $\sqrt{N}$ as the number of samples.

Now substituting $X_j = X_{jSN} + X_{jWN}$, (for j=1,2) we can get an expression:

$$\begin{aligned}\operatorname{var}(\rho_{12}(\tau)) &= \frac{\left(\operatorname{var}(X_{1SN}(t)) \operatorname{var}(X_{2SN}(t)) + \operatorname{var}(\operatorname{Cov}(X_{1WN}(t), X_{2WN}(t+\tau)) \right)}{N \operatorname{var}(X_{1SN}(t)) \operatorname{var}(X_{2SN}(t))} \\ &= \frac{1}{N} + \frac{\operatorname{var}(\operatorname{Cov}(X_{1WN}(t), X_{2WN}(t+\tau))}{N \operatorname{var}(X_{1SN}(t)) \operatorname{var}(X_{2SN}(t))}\end{aligned} \tag{5.4.1.11}$$

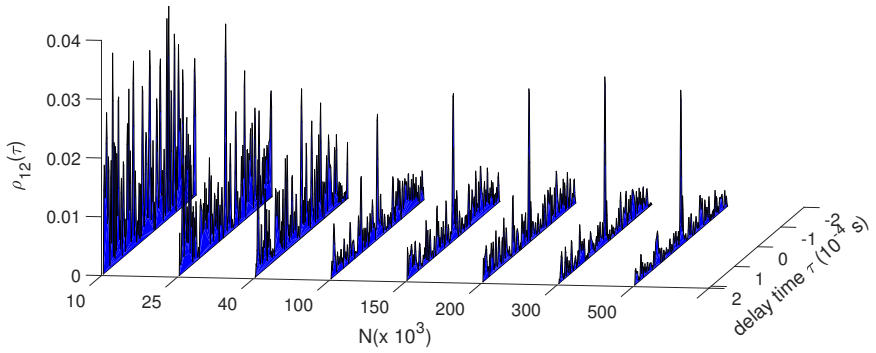

Figure 5.6: The figure above plots the evaluated cross correlation in time domain for coherent light case. Although the integration time was around 1s, for better visualization of peak we plot the time delay between $-200\mu s$ and $200\mu s$. It can be seen that the peak emerges out as we increase the number of samples since the normalized cross correlation for uncorrelated shot noise scales with $\sqrt{N}$.

To contrast the quantum enhancement, lets similarly evaluate the var(ρ_{12}) for the squeezed light injection case. Using equation (5.4.1.9) and substituting $X_j = X_{jSQ} + X_{jWN}$, (for j=1,2) we can get an expression:

$$\mathrm{var}(\rho_{12}(\tau)) = \frac{\left(\frac{\mathrm{var}(X_{1SQ}(t))\mathrm{var}(X_{2SQ}(t))}{N} + \frac{\mathrm{var}(\mathrm{Cov}(X_{1WN}(t),X_{2WN}(t+\tau))}{N}\right)}{\mathrm{var}(X_{1SN}(t))\mathrm{var}(X_{2SN}(t))} \tag{5.4.1.12}$$

$$\mathrm{var}(\rho_{12}(\tau)) = \frac{\mathrm{var}(X_{1SQ}(t))\mathrm{var}(X_{2SQ}(t))}{N\mathrm{var}(X_{1SN}(t))\mathrm{var}(X_{2SN}(t))} + \frac{\mathrm{var}(\mathrm{Cov}(X_{1WN}(t), X_{2WN}(t+\tau))}{N\mathrm{var}(X_{1SN}(t))\mathrm{var}(X_{2SN}(t))} \tag{5.4.1.13}$$

Hence the above quantity shows that the reduction of the background is effected by the quantity $\frac{\mathrm{var}(X_{1SQ})\mathrm{var}(X_{2SQ})}{\mathrm{var}(X_{1SN})\mathrm{var}(X_{2SN})}$ for given N number of samples compared to the coherent case of equation (5.4.1.11).

This can be clearly noticed in the fig. 5.7 where the correlated noise peak, which is initially hidden in background noise, is resolved for shorter integration times (shorter number of samples) when squeezing is used (red traces), compared to the classical case of no squeezing (blue traces).

Signal to Noise ratio

The Signal to Noise ratio of the normalized cross correlation function is defined as,

$$\mathrm{SNR} = \frac{\langle\rho_{12}(\tau = 0)\rangle - \langle\rho_{12}(\tau \neq 0)\rangle}{\langle\rho_{12}(\tau \neq 0)\rangle} \tag{5.4.1.14}$$

The absolute value of the cross correlation of the interferometer readouts can be evaluated as the following:

$$|R_{12}(\tau)| = |\mathrm{Cov}(X_1(t)X_2(t+\tau))| \approx \sqrt{\langle \mathrm{Cov}^2(X_1, X_2)\rangle} \tag{5.4.1.15}$$

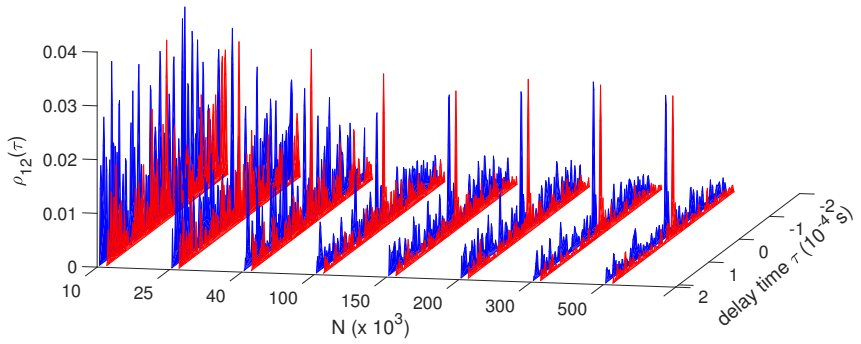

Figure 5.7: The figure above plots the evaluated cross correlation in time domain for classical case as well as for squeezed case. Although the integration time was around 1s, for better visualization of peak we plot the time delay between $-200\mu s$ and $200\mu s$. It can be seen clearly that the correlation peak which was not seen in classical case (blue traces) for shorter integration time can be resolved earlier in the injected squeezed light cases (red traces).

The above approximation in equation (5.4.1.15) holds for large N, as for the limit $N \to \infty$, the equation (5.4.1.9) becomes,

$$\left\langle \mathrm{Cov}^2(X_1, X_2) \right\rangle = \langle X_1 X_2 \rangle^2 \tag{5.4.1.16}$$

and therefore,

$$\sqrt{\langle \mathrm{Cov}^2(X_1, X_2) \rangle} = |\langle X_1 X_2 \rangle| \tag{5.4.1.17}$$

Now, let us consider the normalized cross correlation function $\rho_{12}(\tau)$. Using equation(5.4.1.9) we can write the cross correlation function $\rho_{12}(\tau)$

$$\begin{aligned} \langle \rho_{12}(\tau) \rangle &= \frac{\sqrt{\langle \mathrm{Cov}^2(X_1, X_2) \rangle}}{\sqrt{\mathrm{var(X_{1SN})var(X_{2SN})}}} \\ &= \frac{\sqrt{\frac{\langle X_1^2 X_2^2 \rangle}{N} + (1 - \frac{1}{N}) \langle X_1 X_2 \rangle^2}}{\sqrt{\mathrm{var(X_{1SN})var(X_{2SN})}}} \end{aligned} \tag{5.4.1.18}$$

Let us look into the case $\tau \neq 0$ in fig. 5.6, where the two outputs of the interferometer are shot noise limited, while the injected white noise is very much lower than shot noise of the individual interferometers, the cross correlation of the readout time series are uncorrelated away from $\tau = 0$. However the mean value of this uncorrelated noise fluctuation is non-zero as discussed before, as we consider the absolute value of the covariance. Hence for $\tau \neq 0$, we get:

$$\langle \rho_{12}(\tau \neq 0) \rangle = \frac{\sqrt{\frac{\langle X_1^2 X_2^2 \rangle}{N} + (1 - \frac{1}{N}) \langle X_1 X_2 \rangle^2}}{\sqrt{\mathrm{var(X_{1SN})var(X_{2SN})}}} \tag{5.4.1.19}$$

Since X_{1SN} and X_{2SN} are independent, $\langle X_1^2 X_2^2 \rangle$ can be written as $\mathrm{var}(X_1)\mathrm{var}(X_2)$

and using $\langle X_1 X_2 \rangle = 0$, we get

$$\langle \rho_{12}(\tau \neq 0) \rangle = \sqrt{\frac{\mathrm{var}(X_1)\mathrm{var}(X_2)}{N\mathrm{var}(X_{1SN})\mathrm{var}(X_{2SN})}} \tag{5.4.1.20}$$

(ii) For the case of $\tau = 0$, we can write similarly using equation (5.4.1.19)

$$\langle \rho_{12}(\tau = 0) \rangle = \frac{\sqrt{\frac{\langle X_1^2 X_2^2 \rangle}{N} + (1 - \frac{1}{N}) \langle X_1 X_2 \rangle^2}}{\sqrt{\mathrm{var(X_{1SN})var(X_{2SN})}}} \tag{5.4.1.21}$$

Since we have a non zero-covariance at $\tau = 0$, due to injection of white noise the term $\langle X_1 X_2 \rangle^2 = \langle X_{1WN} X_{2WN} \rangle^2$. Hence we can evaluate $\langle \rho_{12}(\tau = 0) \rangle$ as,

$$\langle \rho_{12}(\tau = 0) \rangle = \sqrt{\frac{\frac{\mathrm{var}(X_1)\mathrm{var}(X_2)}{N} + (1 - \frac{1}{N}) \langle X_{1WN} X_{2WN} \rangle^2}{\mathrm{var}(X_{1SN})\mathrm{var}(X_{2SN})}} \tag{5.4.1.22}$$

Hence the SNR as defined in equation (5.4.1.14) can be written as

$$\begin{aligned} \mathrm{SNR} &= \frac{\langle \rho_{12}(\tau = 0) \rangle - \langle \rho_{12}(\tau \neq 0) \rangle}{\langle \rho_{12}(\tau \neq 0) \rangle} \\ &\approx \sqrt{1 + \frac{N \langle X_{1WN} X_{2WN} \rangle^2}{\mathrm{var}(X_1)\mathrm{var}(X_2)}} - 1 \end{aligned} \tag{5.4.1.23}$$

Figure 5.8 shows the signal-to-noise ratio (SNR) of the measurement. Each data point as described in equation (5.4.1.14) is calculated as the ratio between the cross correlation peak height for $\tau = 0$ and the floor level as defined in equation (5.4.1.14).

It can be seen that from equation (5.4.1.23), for higher values of number of samples, SNR scales as $N^{\frac{1}{2}}$.

Similarly,the enhancement factor R defined as ratio of SNR_{sqz} to SNR_{coh} is given by,

$$R = \frac{\mathrm{SNR}_{sqz}}{\mathrm{SNR}_{coh}} = \frac{\left[\sqrt{1 + \frac{N\langle X_{1WN} X_{2WN} \rangle^2}{\mathrm{var}(X_{1SQ})\mathrm{var}(X_{2SQ})}} - 1\right]}{\left[\sqrt{1 + \frac{N\langle X_{1WN} X_{2WN} \rangle^2}{\mathrm{var}(X_{1SN})\mathrm{var}(X_{2SN})}} - 1\right]} \tag{5.4.1.24}$$

where X_{1SQ} and X_{2SQ} represent the readout time-series of interferometers when the squeezed light is injected. For higher N number of samples the ratio of SNR_{sqz} to SNR_{coh} is written as,

$$R \approx \sqrt{\frac{\mathrm{var}(X_{1SN})\mathrm{var}(X_{2SN})}{\mathrm{var}(X_{1SQ})\mathrm{var}(X_{2SQ})}} \tag{5.4.1.25}$$

The SNR_{coh} (SNR_{sqz}) evaluated for the data points as function of number of samples N is fitted with the function described below:

$$\mathrm{SNR}_{coh/sqz} = \sqrt{1 + N k_{coh/sqz}} - 1 \tag{5.4.1.26}$$

where $k_{coh/sqz}$ is a parameter estimated from the fit. From equation (5.4.1.23), the value

of k_{coh} can be written as $\frac{\langle X_{1WN} X_{2WN}\rangle^2}{\mathrm{var}(X_{1SN})\mathrm{var}(X_{2SN})}$ when we evaluate SNR_{coh}. Similarly the value of k_{sqz} can be written as $\frac{\langle X_{1WN} X_{2WN}\rangle^2}{\mathrm{var}(X_{1SQ})\mathrm{var}(X_{2SQ})}$ when we evaluate SNR_{sqz}. The values k_{coh} and k_{sqz} estimated from the fit are reported in the table 5.2.

The enhancement factor R defined in equation (5.4.1.25) which was evaluated from the data, matches the independent estimation of the ratio $\sqrt{\frac{k_{sqz}}{k_{coh}}}$ which is around 2 times more than the coherent case.

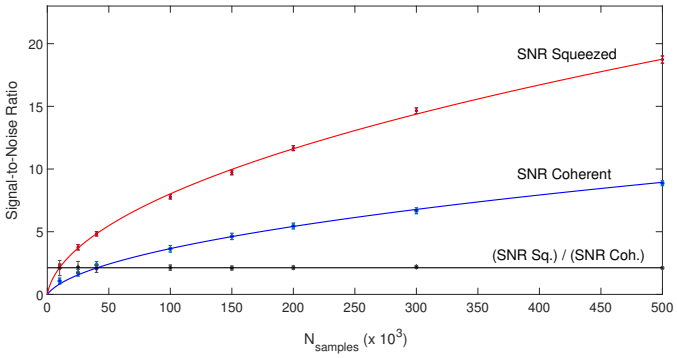

Figure 5.8: SNR of the cross-correlation as a function of the number of samples. Dots represent experimental data (error bars are too small to be appreciated). Data are well fitted by the function defined in the equation (5.4.1.26) (blue and red traces). Black trace is the ratio between squeezed and coherent SNR values.

k_{coh}	$(3.70 \pm 0.17) \times 10^{-4}$
k_{sqz}	$(1.51 \pm 0.03) \times 10^{-3}$
R	(2.12 ± 0.05)

Table 5.2: Evaluated parameters from SNR vs Number of samples fit in fig. 5.8

Noise Reduction factor

Another way for calculating the quantum enhancement is by evaluating the quantum noise reduction factor (NRF), which is defined as

$$\begin{aligned} NRF &= \frac{\mathrm{var}(X_{1SQ} - X_{2SQ})}{\mathrm{var}(X_{1SN} - X_{2SN})} \\ &= \frac{\mathrm{var}(X_{1SQ}) + \mathrm{var}(X_{2SQ})}{\mathrm{var}(X_{1SN}) + \mathrm{var}(X_{2SN})} \end{aligned} \tag{5.4.1.27}$$

where X_{1SQ}, X_{2SQ} are time series of interferometer outputs when the squeezed light is injected and X_{1SN}, X_{2SN} are the time series of interferometer outputs recorded with the coherent light. This factor should be less than unity. This quantity estimates the amount of equivalent noise reduction of the combined system when two independent squeezed light are injected into the interferometers.

The NRF in our case was around 0.56, which indicates that there was around 2.5dB equivalent reduction in the quantum noise due to the injection of squeezing.

5.5 Cross correlation in Frequency domain

In the spectral domain, correlated signals can be extracted by performing the cross-power spectral density (CPSD) $S_{12}(\omega)$ of the two interferometers[59].

$$S_{12}(\omega) = \sum_{n=0}^{N} R_{12}(n) e^{-j\omega n} \tag{5.5.0.1}$$

where $R_{12} =< x_{1,n+m} x_{2,m} >$, $x_{1,n}$ and $x_{2,n}$ are the n^{th} elements of the two time series of the interferometers. The CPSD was evaluated using the Welch method as described in section D.2 of Appendix D, implemented by a labview code. It consists in dividing the time series in $N_{spectra}$ bins and for each bin the CPSD is calculated as the discrete Fourier transform of the cross-correlation [62]. The average of the $N_{spectra}$ CPSD values is then evaluated. The cross spectral density on contrary to the power spectral density, contains both real and complex parts and thus we considered its magnitude.

In analogy with the time-domain (see equation (5.4.1.9)), the evaluation of the cross power spectral density $S_{12}(\omega)$ when correlated phase noise is injected gives,

$$\begin{aligned} S_{12}(\omega) = FFT(R_{12}(\tau)) &= \sqrt{\frac{\mathrm{PSD}_{X_1}\mathrm{PSD}_{X_2}}{N_{spectra}} + (1 - \frac{1}{N_{spectra}}) \left[S_{12}^{(w)}(\omega) \right]^2} \\ &\approx \sqrt{\frac{\mathrm{PSD}_{X_1}\mathrm{PSD}_{X_2}}{N_{spectra}} + \left[S_{12}^{(w)}(\omega) \right]^2} \end{aligned} \tag{5.5.0.2}$$

where $S_{12}^{(w)}(\omega)$ gives the estimate of CPSD of the injected phase noise in two interferometers. The cross linear spectral density (CLSD) is then evaluated by calculating the square root of the CPSD. The motivation for choosing the CLSD over CPSD is because the CLSD evaluated in units of $V/\sqrt{Hz}$ and it could be used for estimation of Displacement sensitivity ($m/\sqrt{Hz}$) as described in section 4.3.2.

When no phase noise is injected we deal only with the photon noise of the interferometers. Using the equation (5.5.0.2), we can write:

$$\mathrm{CLSD} = \sqrt{S_{12}(\omega)} = (\frac{\sqrt{PSD_{X_{1SN}} PSD_{X_{2SN}}}}{N_{spectra}^{1/2}})^{1/2} \tag{5.5.0.3}$$

The CLSD evaluated reduces the contribution of the uncorrelated signals (are which correspond to the shot noise of the two interferometers in our case) and it is enhanced by a factor $N_{spectra}^{\frac{1}{4}}$. However when a correlated phase noise injected into the system, contribution of the uncorrelated signals by a factor $N_{spectra}^{\frac{1}{4}}$, while the correlated contribution is unaffected. When $N_{spectra}$ is sufficiently high, the CLSD reaches a plateau, which represents the correlated noise contribution.

When the squeezed light is injected, the uncertainty reduction of the uncorrelated photon noise contribution is expected to be the geometric mean of the two enhancement factors of each interferometer, i.e $\sqrt{(e^{-2r_1} + \frac{1-\eta_{loss,1}}{\eta_{loss,1}})(e^{-2r_2} + \frac{1-\eta_{loss,2}}{\eta_{loss,2}})}$ where r_1 and r_2 are the squeezing factors in the individual interferometers, $\eta_{loss,1}$ and $\eta_{loss,2}$ are the losses

in each interferometer.

Figure 5.9 shows the average value of the CLSD evaluated as a function of $N_{spectra}$ in a bandwidth of 100kHz without injecting the white noise (dealing only with the photon noise of the interferometers) for both coherent case (blue trace) as well as in squeezed case (red trace).

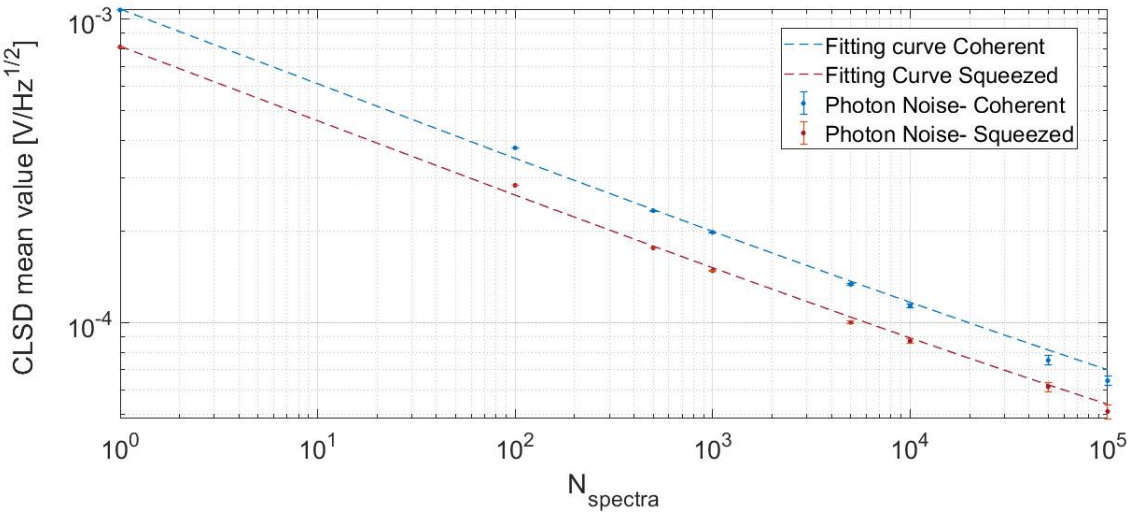

Figure 5.9: The Cross linear spectral density plotted as a function of $N_{spectra}$. It can be seen that in the case of no noise injected the CLSD scales as $N_{spectra}^{-\frac{1}{4}}$. The blue trace corresponds to coherent states while the red trace corresponds to squeezed light injection.

Since the CLSD in the photon noise case scales inversely proportional to $N_{spectra}^{1/4}$, as discussed in equation (5.5.0.3), the CLSD was fitted with:

$$\text{CLSD} = \left(\frac{A}{N_{spectra}} + c\right)^{1/4} \tag{5.5.0.4}$$

where A is a parameter that could be evaluated from the fit, which represents the square root of geometric mean of the PSD's of the individual interferometers as described in equation (5.5.0.3). When there is no correlated noise injected in the system, the CLSD($N_{spectra} = 1$) = $A^{1/4}$. If the two interferometers are having equal values of PSD, then $A^{1/2}$ represents the average PSD level of single interferometer. The fit parameters are displayed in table 5.3.

A_1	$(1.296 \pm 0.001) \times 10^{-12}$
c_1	$1.601 \times 10^{-5} \pm 1.861 \times 10^{-20}$
A_2	$(4.174 \pm 0.002) \times 10^{-13}$
c_2	$7.154 \times 10^{-21} \pm 1.051 \times 10^{-20}$

Table 5.3: The parameters A and c values of equation (5.5.0.4) evaluated from the fit of CLSD vs $N_{spectra}$ in both classical as well as squeezed case.

It is to be noted that the constants c_1 and c_2 are compatible uncertainty with the estimated mean values and hence can be approximated to zero. The ratio of $(A_2/A_1)^{0.25}$ =

1.35 gives us the uncertainty reduction in the evaluated CLSD for the squeezed light injected case with respect to the coherent case . The smallest value of CLSD obtained due to squeezed light injection in this measurement at $N_{spectra} = 10^5$ is around $\frac{1}{20}$ times reduction with respect to the value of PSD of a single interferometer (which corresponds to CLSD ($N_{spectra} = 1$)).

The fig. 5.10 (i) shows the plot of CLSD vs $N_{spectra}$ when a correlated noise is injected. For comparison with the photon noise case, the fig. 5.9 has also been depicted in the same plot. It can be seen that for lower $N_{spectra}$, the CLSD value confides with the photon noise and scales with $N_{spectra}^{-1/4}$. However, for higher $N_{spectra}$, the CLSD reaches a plateau representing the correlated noise contribution. The difference between the photon noise case and the correlated noise injected case can be seen at $N_{spectra} = 1000$ described in fig. 5.10 (ii) where we plot the CLSD spectra as a function of frequency in a bandwidth of 100kHz.

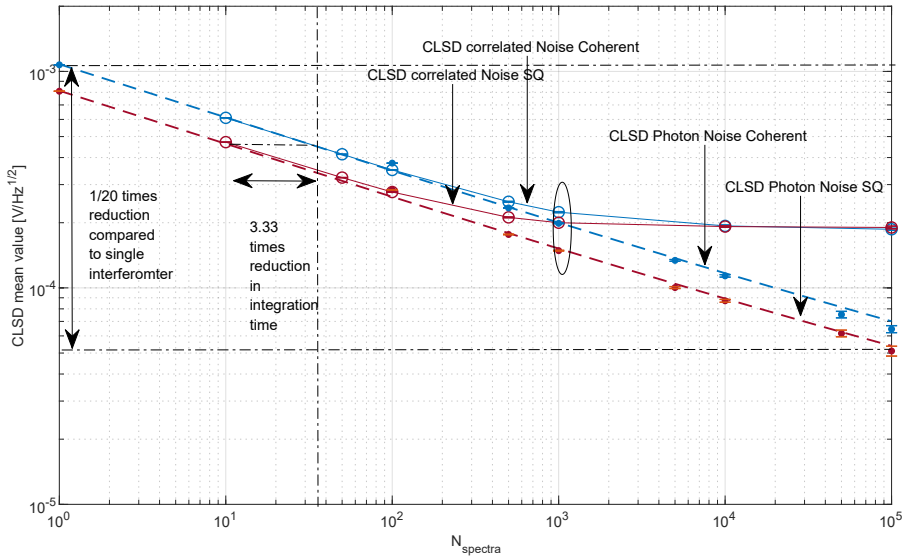

(i)

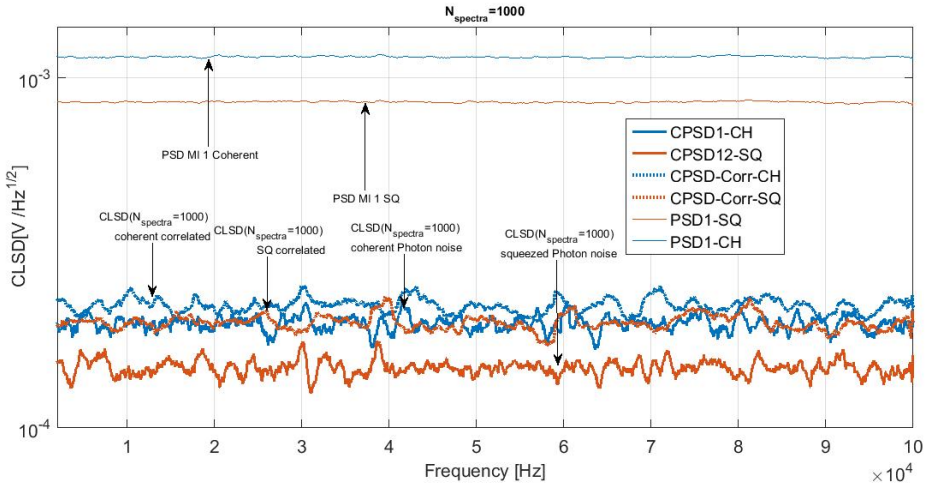

(ii)

Figure 5.10: (i)The figure above presents the Cross linear Spectral density as a function of Number of Spectra. It can be seen that for low values of $N_{spectra}$ it scales as $N_{spectra}^{-1/4}$ while for higher values of $N_{spectra}$ it reaches a plateau. (ii) The figure above corresponds to the CLSD evaluated at $N_{spectra} = 1000$ and PSDs of the first interferometer.

Since the $N_{spectra}$ is proportional to integration time, a clear advantage appears when we use squeezing, since the plateau is reached earlier for shorter $N_{spectra}$ (corresponding to around 3.3 times of integration time reduction) compared to coherent case.

5.6 Evaluation of Sensitivity

We have measured the CLSD in $\frac{V}{\sqrt{Hz}}$ and we now need to convert it into $\frac{m}{\sqrt{Hz}}$ for evaluating the displacement sensitivity. For this reason, the input voltage $V_{rms} = 40\mu V$ of the white noise given to the EOM was measured using a spectrum analyzer with a resolution bandwidth of 100kHz at 13.5MHz. The conversion from CLSD $(V/\sqrt{Hz})$ to Displacement sensitivity, we need to consider the equivalent strain ΔX_{rms} caused by the EOM as discussed in section 4.3.2. The point where we reach a plateau in the plot of CLSD as a function of $N_{spectra}$ in fig. 5.10 corresponds to this equivalent strain ΔX_{rms}. Also as we know that displacement sensitivity ΔX for CLSD ($N_{spectra} = 1$) corresponds to displacement sensitivity of single interferometer as we have discussed in section 5.5. Hence we can write the following equation as:

$$\frac{\Delta X(m/\sqrt{Hz})}{\Delta X_{rms}(m/\sqrt{Hz})} = r \tag{5.6.0.1}$$

where r is the ratio of the CLSD $(V/\sqrt{Hz})$ evaluated for $N_{spectra} = 1$ to the CLSD $(V/\sqrt{Hz})$ evaluated when it reaches the plateau and in our case it was around $\frac{1}{5}$.

However, as discussed in section 4.3.2 we can calculate the ΔX_{rms} as

$$\Delta X_{rms} = \frac{\lambda V_{rms}}{2V_\pi\sqrt{\Delta\omega}} \tag{5.6.0.2}$$

and the value of V_π evaluated for the EOM was around 980 V as discussed in section 4.3.2. Hence the displacement sensitivity $(m/\sqrt{Hz})$ ΔX can be written as:

$$\Delta X = \frac{\lambda V_{rms}}{2V_\pi\sqrt{\Delta\omega}} r \tag{5.6.0.3}$$

The fig. 5.11 shows the evaluated version of displacement sensitivity ($\frac{m}{\sqrt{Hz}}$). The sensitivity obtained in each interferometer (which corresponds to $N_{spectra} = 1$) was $(6.745 \pm 0.002) \times 10^{-16} \frac{m}{\sqrt{Hz}}$. The maximum sensitivity reported in the plot corresponding to $N_{spectra} = 10^5$ with independent squeezed states was evaluated to be $(3.21 \times 10^{-17} \pm 0.16 \times 10^{-18}) \frac{m}{\sqrt{Hz}}$, which is 1/20 of the sensitivity of each interferometer.

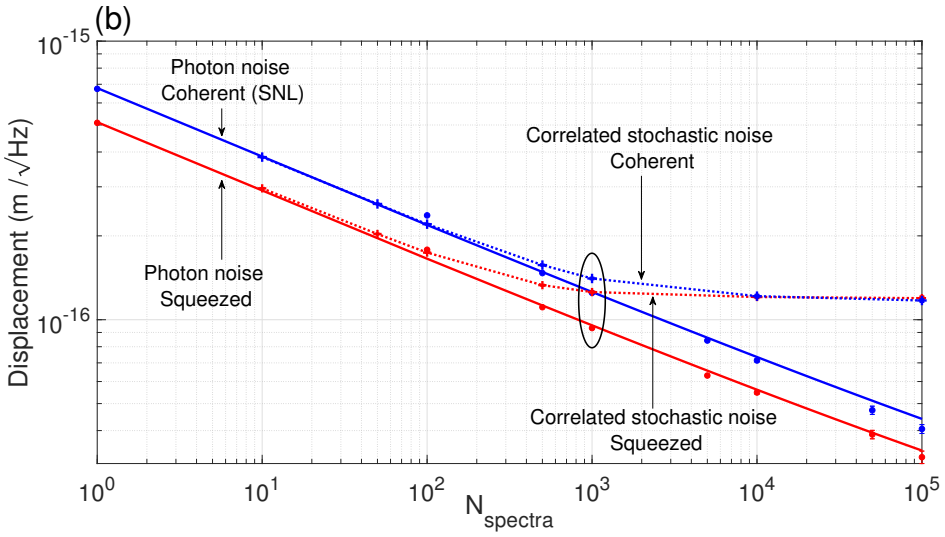

(i)

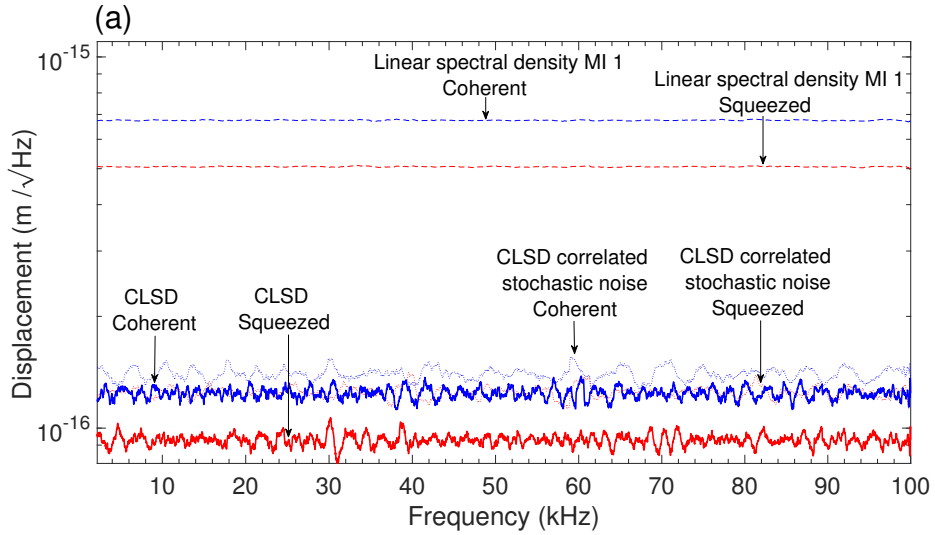

(ii)

Figure 5.11: (i)The figure above presents the Displacement sensitivity ($\frac{m}{\sqrt{Hz}}$) as function of Number of Spectra. (ii) The figure above corresponds to the Displacement Sensitivity (evaluated at $N_{spectra} = 1000$ and PSDs of the first interferometer.

5.7 Summary

We have discussed in details the results of the double squeezer experiment both in time domain as well as in frequency domain. The injection of squeezing helped us reducing the background of the shot noise in each interferometer as well as in the normalized cross correlation function in time domain for revealing the signal for shorter integration time and increasing the Signal to noise ratio by factor of 2. The concepts such as CLSD have been discussed and evaluated. We have clearly shown the advantage of performing cross correlation. Around 1/20 times reduction was observed in correlated phase detection sensitivity with respect to shot noise of single interferometer and around 3.33 times reduction

in integration time was observed in the CLSD when squeezed light was injected. This experimental results would help us pave path to consider squeezing as a helpful tool in reducing the sensitivity and to consider it as a strategy in applications such as determination of holographic noise, Stochastic Gravitational wave background [23] as discussed in section 1.6.

CHAPTER 6

RESULTS WITH TWIN BEAM STATE

6.1 Introduction

In the experimental scheme as described in Chapter 1 in section 1.5.1, when each mode of the twin beam state is injected in the two interferometer and subtraction between the ouptuts is measured, the nonclassical quadrature correlation is expected to provide a noise reduction. Any phase difference between the two MIs produces a change in the relative photo-currents, which can be detected with sub shot-noise sensitivity. However,as far as only correlation in one of the quadrature is used, instead of an actual twin beam, we used a twin beam like state as mentioned in section 1.3.3, which was produced by a single mode squeezed state split on a beam splitter. The experimental setup and details of the locking scheme are already described in chapter 3 in section 3.4. As we have discussed, this experimental scheme is useful for detection of uncorrelated noise or small phase signal difference between the interferometers. In this chapter we present the effect of reduction in shot noise of the interferometers photocurrent subtraction due to the bipartite non-classical state with the consequence of a better sensitivity in identifying uncorrelated noise. We present this analysis in both time domain as well as the frequency domain .

6.2 Results in Time Domain

As mentioned in chapter 1 in section 1.5.3, the task is to measure the variance of difference between the two outputs of interferometers. Let X_1 and X_2 represent the output photocurrents of interferometer 1 and interferometer 2. The variance of difference between the outputs is given by:

$$\mathrm{var}(X_1(t) - X_2(t+\tau)) = \mathrm{var}(X_1(t)) + \mathrm{var}(X_2(t)) - 2\mathrm{cov}(X_1(t), X_2(t+\tau)) \qquad (6.2.0.1)$$

Since the single mode squeezer output is split on a balanced beam splitter as shown in fig. 1.6, the first two terms, which are variances of individual interferometers, are squeezed

although the individual squeezing level is reduced by 50% losses of the input squeezed light. However we have a non-zero covariance as discussed in properties of twin beam state in section 1.3.3 of chapter 1 as opposed to the classical case or to the two independent squeezers case. Hence the entire input squeezing should be recovered in the var$(X_1 - X_2)$ We have performed the twin beam injection in the double interferometer system in three conditions: (i)No noise injected in two interferometers (just dealing with the photon noise) (ii)uncorrelated noise injected in two interferometers (iii) Correlated noise injected in two interferometers

6.2.1 Photon noise

Let us consider the case when no artificial noise is injected in interferometers. When TWB state is injected in the interferometer, as we know from section 1.3.3, there is a non zero covariance between the outputs of two interferometer outputs. This cross correlation between the two interferometers is maximized by adjusting the phase between the two down mixed outputs (AC outputs of interferometers) as shown in fig. 5.5.

The cross correlation between the two outputs is evaluated both in coherent case and in twin beam case as shown in fig. 6.1. It can be seen that for the twin beam case there is a non-zero correlation at delay $\tau = 0$ while it vanishes in the classical case.

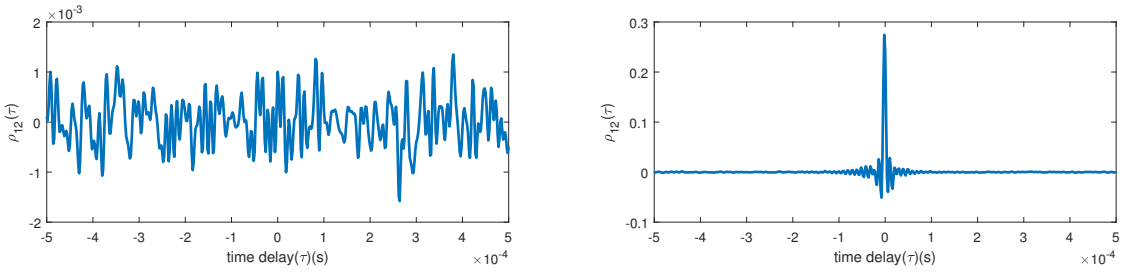

Figure 6.1: The figure above plots the cross-correlation coefficient as a function of time delay τ. The figure on the left corresponds to cross correlation coefficient in the classical case and the figure on the right corresponds to the TWB state injection. It can be seen there is a non-zero covariance at $\tau = 0$ in the TWB case while the noise is uncorrelated in the classical case.

We have also evaluated, more specifically, the variance as function of time delay. The variance evaluated as a function of delay τ is given by,

$$\mathrm{var}(X_{1PN}(t) - X_{2PN}(t+\tau)) = \mathrm{var}(X_{1PN}(t)) + \mathrm{var}(X_{2PN}(t)) - 2\,\mathrm{cov}(X_{1PN}(t), X_{2PN}(t+\tau)) \tag{6.2.1.1}$$

where X_{1PN} and X_{2PN} represent the photon noise in both interferometers.

While evaluating the variance of the difference, we should make appropriate normalizations in the gain of the detector. Let g_1 and g_2 be the gain in detectors of interferometer 1 and interferometer 2 with output time series X_1 and X_2. The gain in detector is then evaluated as,

$$g_1 = \frac{\text{var}(X_1)}{P_1},\ g_2 = \frac{\text{var}(X_2)}{P_2} \tag{6.2.1.2}$$

where P_1 and P_2 are DC optical powers. Ideally these 2 factors g_1 and g_2 should be equal if the interferometers are shot noise limited. However, the difference in gain in electronics prevents them to be same.

Thus, one has to compensate for this electronic gains difference, evaluating the variance of the photocurrent as $\text{var}(X_1(t) - \sqrt{\frac{g_2}{g_1}}X_2(t+\tau))$

The fig. 6.2 evaluates the difference as a function of delay τ. Firstly the shot noise level (SNL) is obtained by blocking the non-classical light and measuring the $\text{var}(X_{1SN}(t) - X_{2SN}(t+\tau))$. When the TWB like state is injected, at delay $\tau = 0$, we have the effect of the the correlation between the two modes due to non zero covariance which leads to a noise reduction of 2.5 dB with respect to the SNL, is that appears as a dip in the variance. While away from $\tau = 0$, the covariance goes to zero and the shot noises reduces to the squeezing registered in each interferometers (which is around 50% of input squeezing).

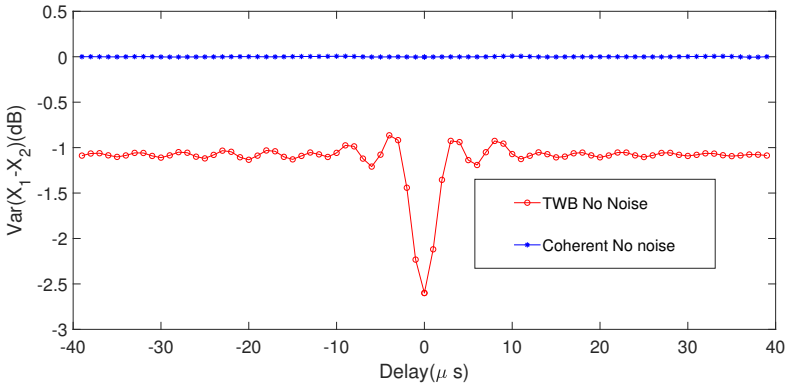

Figure 6.2: The figure above represents the variance of photocurrent difference as in equation (6.2.1.1) as function of delay τ, when no artificial noise is added. The blue trace represents the case in which only coherent light travels in the interferometer, while the red trace concerns the case in which twin beam (TWB) like state is injected. The measured noise reduction is of 2.5 dB with respect to the SNL.

6.2.2 Injection of uncorrelated noise

Let us now consider the case when the uncorrelated phase noise is injected. Let X_{1WN} and X_{2WN} be the uncorrelated noise injected in the interferometers and X_{1PN} and X_{2PN} be the photon noise. Then the variance of the difference is given by

$$\begin{aligned}\text{var}(X_1 - X_2) &= \text{var}((X_{1PN} + X_{1WN}) - (X_{2PN} + X_{2WN})) \\ &= \text{var}(X_{1PN} - X_{2PN}) + \text{var}(X_{1WN} - X_{2WN}) \\ &= \text{var}(X_{1PN} - X_{2PN}) + \text{var}(X_{1WN}) + \text{var}(X_{2WN}) - 2\text{cov}(X_{1WN}, X_{2WN})\end{aligned} \tag{6.2.2.1}$$

Since they are uncorrelated, $\text{cov}(X_{1WN}, X_{2WN}) = 0$. Hence the above equation can be written as

$$\text{var}(X_1 - X_2) = \text{var}(X_{1PN} - X_{2PN}) + \text{var}(X_{1WN}) + \text{var}(X_{2WN}) \tag{6.2.2.2}$$

The above equation (6.2.2.2) shows that the dip at $\tau = 0$ decreases by the amount $\text{var}(X_{1WN}) + \text{var}(X_{2WN})$.

When two uncorrelated stochastic signals are injected in the two interferometers, the dip reduces by ≈ 1 dB, as shown by the red faint line as shown in fig. 6.3. This must be compared with the change between classical coherent trace levels with and without noise injection (blue thick and faint line respectively), which is only ≈ 0.3 dB

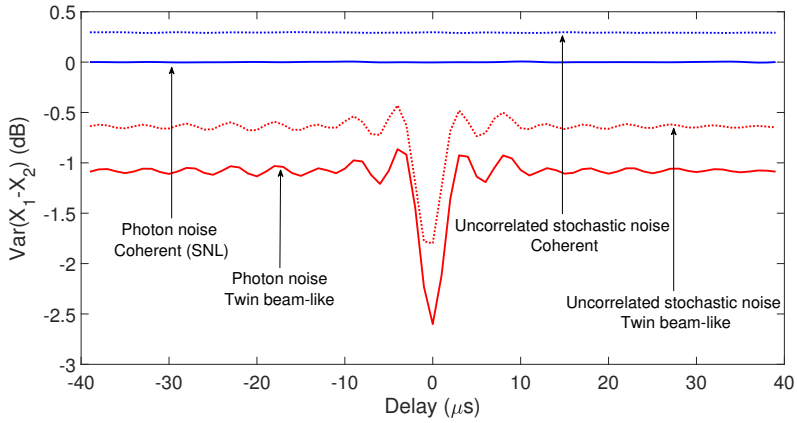

Figure 6.3: Variance on the read-out signal subtraction with varying relative time delay. Red curves refer to the twin beam - like case and blue curves to the classical coherent one. Faint lines refer to the addition of an uncorrelated stochastic noise in the two MIs.

6.2.3 Injection of Correlated noise

When we inject correlated noise, the signals get cancelled by the subtraction, and the variance is not changed. Let X_{1WN} and X_{2WN} be the correlated noises injected in two interferometers and X_{1PN} and X_{2PN} be the photon noise. Then variance of difference is given by

$$\begin{aligned}\text{var}(X_1 - X_2) &= \text{var}((X_{1PN} + X_{1WN}) - (X_{2PN} + X_{2WN})) \\ &= \text{var}(X_{1PN} - X_{2PN}) + \text{var}(X_{1WN} - X_{2WN}) \\ &= \text{var}(X_{1PN} - X_{2PN}) + \text{var}(X_{1WN}) + \text{var}(X_{2WN}) - 2\text{cov}(X_{1WN}, X_{2WN})\end{aligned} \tag{6.2.3.1}$$

If $X_{1WN} = X_{2WN} = X_{WN}$ and since they are correlated, $\text{cov}(X_{1WN}, X_{2WN}) = \text{var}(X_{WN})$. Hence $\text{var}(X_{1WN}) + \text{var}(X_{2WN}) - 2\text{cov}(X_{1WN}, X_{2WN}) = 0$. Thus we can write,

$$\text{var}(X_1 - X_2)|_{\text{correlated noise}} = \text{var}(X_{1PN} - X_{2PN}) \tag{6.2.3.2}$$

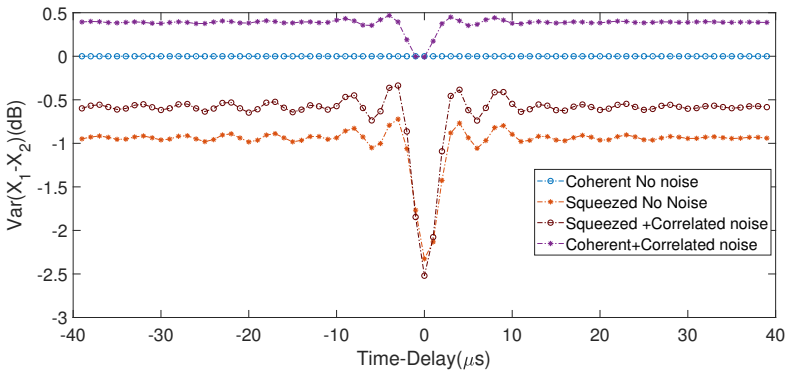

Figure 6.4: Variance on the read-out signal subtraction with varying relative time delay. Red curves refer to the twin beam - like case and blue curves to the classical coherent one. It can be seen that at delay $\tau = 0$ unlike in the uncorrelated case, the variance of difference of the photon currents when the correlated noise is injected is equal to the variance of difference of the photon noise case.

The fig. 6.4 plots the variance of difference of the outputs of the interferometers as a function of τ. It can be seen that the depth of the dip is unchanged as opposed to the uncorrelated case.

However,the case of correlated noise is much more useful in application for search of holographic noise. As discussed in section 1.6, the experiment has to be performed in two configurations (i) $\|^{el}$ (ii) $\perp^{r}$. The covariance between two interferometer according to equation (1.6.0.4) can then be evaluated.

6.3 Results in Frequency domain

The power spectral density of the difference of the photocurrent outputs of the interferometers are evaluated. The photocurrents outputs are compensated for the electronic gains and power spectral density of PSD($X_1 - \sqrt{(\frac{g_2}{g_1})}X_2$) is evaluated as discussed in section 6.2.1. The same amount of quantum enhancement as in fig. 6.3 has been demonstrated in the frequency domain as shown in fig. 6.5.

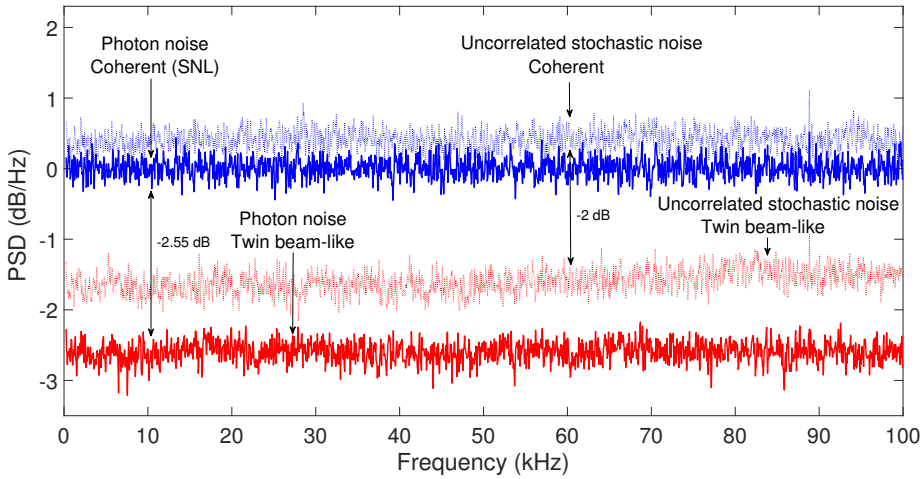

Figure 6.5: Power Spectral Density (PSD) of the read-out signals subtraction calculated from the read-out signals down-mixed at 13.5 MHz. Red curves refer to the twin beam - like case and blue curves to the classical coherent one. Faint lines refer to the addition of an uncorrelated stochastic noise in the two MIs.

As a further example, a single tone frequency was also injected in one of the interferometers. The fig. 6.6 shows the power spectral density of $X_1(t) - \sqrt{(\frac{g_2}{g_1})}X_2(t)$ for a single frequency tone applied to one of the MIs. Also in this case the quantum-enhancement is clearly visible. The quantum enhancements of the individual interferometers are 1.1 and 0.8 dB respectively, resulting in a collective enhancement of 2 dB in the output subtraction, due to the non-classical correlation among the modes. This enhancement might be applied to identify uncorrelated noise sources, such as scattering or unwanted resonances [19].

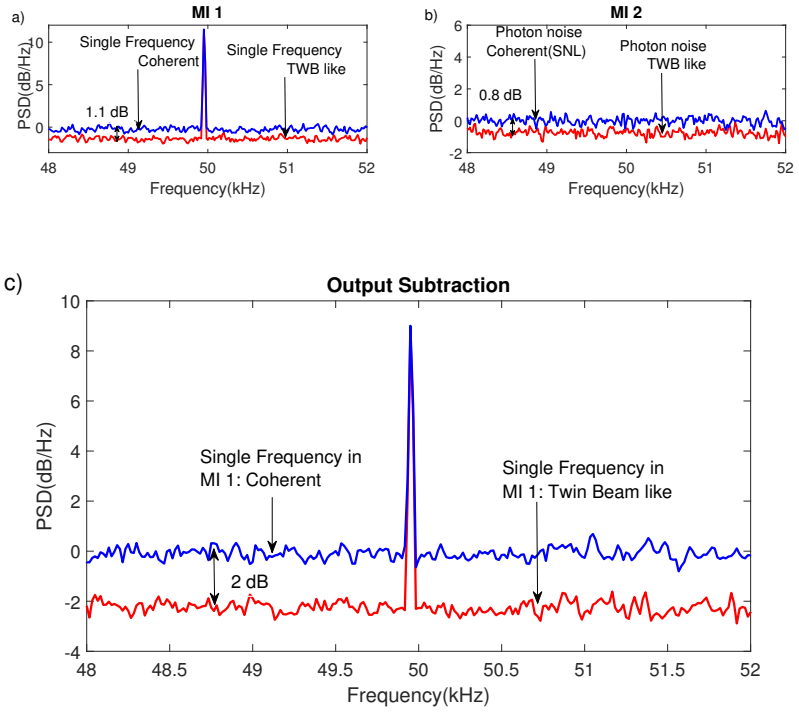

Figure 6.6: Single-frequency tone injected in the first interferometer at 13.55 MHz. (a), (b): PSDs of the read-out signal in each interferometer show 1.1 dB and 0.8 dB quantum-enhancement in MI 1 and MI 2 respectively. (c): PSD of the read-out signals subtraction. The correlation between the two modes leads to 2 dB of squeezing. The frequency axis of all plots correspond to the recorded data after down-mixing at 13.5 MHz.

6.4 Summary

We have demonstrated an approach that uses the non-classical correlation between two modes of an evenly split squeezed state. This approach, as discussed above could be used to detect uncorrelated noise sources such as scattering or resonances. This also opens the perspectives of an extremely high advantage in case of two-mode squeezing (true twin beam entanglement) injection and large detection efficiencies as discussed in chapter 1 in section 1.5.3 where the uncertainty would reduce dramatically when we lock very close to the dark fringe.

CONCLUSION

Quantum metrology is a field that studies the application of quantum states of light for surpassing the classical limit. One of the tool that could be used in performing sensing experiments devoted to fundamental research are optical interferometers. The recent detection of gravitational waves [20] being a prime example, where power recycled Michelson interferometers are used. In 1981, Caves [37] proved theoretically that injection of quantum states of light in these type of interferometers, would provide further enhancement in the sensitivity of the system. The application of injection of squeezed states of light into a single interferometer has already been demonstrated in many gravitational wave detector prototypes[38],[39] as well as in LIGO[21] and GEO 600[40] gravitational wave detectors.

One of the current trends in modern physics for application of the optical interferometers is the search and study of omnipresent stochastic sources of noise such as exotic sources due to conjectured Planck scale effects[27],[42] or gravitational wave background[26]. In particular, these sources of noise can produce correlated phase fluctuations in two separated interferometers increasing the chance of distinguishing them with respect to other noise sources. Hence, the idea is to use a double interferometric system to detect these stochastic sources of noise. A double interferometer configuration is for instance the basis of the Fermilab holometer [26],[27], a device consisting of two co-located 40 m Michelson interferometers. The purpose of the holometer is to search for a particular type of correlated background noise, conjectured in some heuristic Planck scale theories and dubbed holographic noise. If confirmed, it would provide empirical support to theories attempting to unify quantum mechanics and gravitation. The first measurements of the Fermilab were reported in [27] and they have reached a strain sensitivity of $10^{-21}/\sqrt{Hz}$. At the moment the holometer is operated with classical light only.

However, it has been demonstrated theoretically in [28],[29] that when quantum states of light such as squeezed states and Twin beam state are injected into this double interferometric system, it would further enhance the correlated phase detection sensitivity. When two independent squeezed states are injected the uncertainty in the correlated phase detection sensitivity would be reduced by a factor of $\sqrt{(e^{-2r_1}+\frac{1-\eta_{loss,1}}{\eta_{loss,1}})(e^{-2r_2}+\frac{1-\eta_{loss,2}}{\eta_{loss,2}})}$ where r_1 and r_2 are the squeezing factors. While in the latter case, it has been demonstrated that, when the twin beam state is injected, while the Michelson interferometers

are operated near to the dark fringe and have high efficiencies, the uncertainty reduction is divided into two regimes: a) when the classical component of light is almost zero and photon number entanglement dominates and for high detection efficiencies ($T\lambda >> (1-T)\mu$), a dramatic enhancement in the correlated phase detection sensitivity can be obtained. However, when the classical field component dominates ($T\lambda << (1-T)\mu$), the uncertainty reduction in correlated phase detection sensitivity is contributed by the quadrature correlations and the system behaves the same as for the independent squeezed states.

In the present thesis, I have reported a first feasibilty test for realization of quantum enhanced correlated phase interferometery. Based on previous theoretical investigation described in [28],[29], we proved experimentally the advantage of using quantum light (squeezing and bipartite correlations) in the measurement of correlation among phase signals in two interferometers whose outputs are jointly measured. Each interferometer was operated in a power recycling Michelson configuration, thus emulating the configuration used in large scale experiments such as the gravitational wave detectors [36] [21] or the Fermilab "Holometer" [27], dedicated to the investigation of possible Planck scale exotic effects. We have given a complete overview of the locking techniques involved for stabilizing the Power recycling Michelson interferometers. A detail description of the experimental setup of both, double interferometer system and squeezed light sources was provided.

When two independent squeezed states were injected, we have demonstrated an enhancement in the correlated phase detection sensitivity. For the test, a faint correlated white noise was injected with amplitude 1/5 of the shot noise of the individual interferometer. Firstly, we have observed around, 2.5dB and 3dB enhanced sensitivity in each interferometer. Then, exploiting a joint measurement, we have shown that Signal to Noise ratio was enhanced by a factor of 2 (which corresponds to around 3dB of quantum enhancement) compared to the classical case. This allows us to identify this correlated signal for smaller number of samples, in particular reducing the measurement time of 4 times with respect to the classical case . At the same time, we had evaluated a quantity called Cross Linear Spectral Density (CLSD), representing the actual sensitivity to the correlated component of the noise in the two inferferometer in the frequency domain. The absolute sensitivity obtained after only 20 s of measurement time was $(3.21 \pm 0.16) \times 10^{-17} m/\sqrt{Hz}$ which corresponds to around 1/20 times the sensitivity of a single, shot noise limited interferometer. This work has a possible applications in the research about fundamental quests, such as detection of holographic noise, gravitational wave background or to finding traces of primordial blackholes [63],[42]. The second experiment was performed, by considering a twin-beam like state injection in the double interferometer system. A twin beam-like state was produced by splitting a single mode squeezer on a beam splitter and each mode was sent to each interferometer. Firstly, the squeezing observed in individual interferometers were reported to be 1.1dB and 0.9dB (around 50% loss of the initial amount of squeezing is due to splitting ratio of the beam splitter). However, due to non zero covariance property of the twin beam like state, there was around 2.6 dB of noise reduction observed below the shot noise level in the subtraction of the two output photocurrents of the interferometers. This approach is quite useful in detection of un-

correlated noise sources such as scattering, resonances. For testing this, an uncorrelated white noise was injected in both the interferometers slightly above the shot noise (as well as a single frequency signal in one of the interferometers) and a quantum enhancement of around 1dB in detection of this uncorrelated noise was observed. This experiment also represents the first step towards perspectives of reaching an unprecedented sensitivity exploiting entanglement in two mode squeezed state . However, it would require very high detection efficiency and a strict control of the dark fringe point, still challenging for the present possibility [28],[29] .

Thus, with these two interesting approaches we have shown a quantum enhancement in the correlated phase detection sensitivity paving a route for practical applications. The future outlook of the experiment is two-fold. Firstly, the results shown in this thesis demonstrate the advantages in terms of correlated phase sensitivity provided by the described technique, which can be directly applied to improve precision in present experiments, e. g. by injecting the quantum states of light in the current fermilab holometer which consists of 40m interferometers. Secondly, the same results in principle would allow to compact the large scale interferometers onto a table-top setup, by virtue of the enhancement due to quantum light injection, reproducing the performance of current large scale interferometers.

APPENDIX A

MODE MATCHING CONDITIONS FOR THE CAVITIES

A.1 Gaussian Beam

The gaussian beam is a Transverse Electro magnetic field mode (TEM_{00}) and is given by,

$$E(\mathbf{r},t) = E_0 \exp(i(\omega t - kz) - \frac{r^2}{w^2(z)} - ik\frac{r^2}{2R(z)} - i\phi(z)) \tag{A.1.0.1}$$

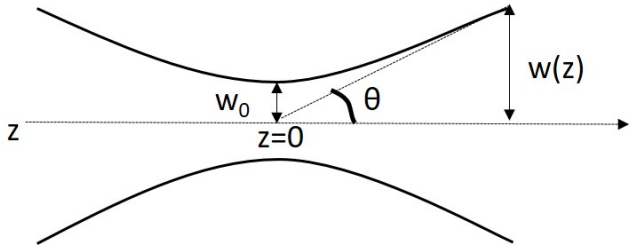

Figure A.1: The pictorial representation of gaussian beam.

where r is the radial distance ($\sqrt{x^2+y^2}$) and z is the axial distance. Let w_0 be the minimum waist of the gaussian beam as shown in fig. A.1. The gaussian beam can be completely described by its beam waist w (z), the radius of curvature R (z). They are given by

$$w(z) = w_0\sqrt{1+\frac{z^2}{z_0^2}} \tag{A.1.0.2}$$

where $z_0 = \frac{kw_0^2}{2}$ is known as the Rayleigh length. and R (z) the radius of curvature of the gaussian beam given by,

$$R(z) = z + \frac{z_0^2}{z} \tag{A.1.0.3}$$

The angle θ represents the divergence of the gaussian beam given by,

$$\theta \approx \frac{w(z)}{z} \approx \frac{\lambda}{\pi w_0} \tag{A.1.0.4}$$

The beam propagation along the optical axis is described by the complex variable $q(z)$

$$\frac{1}{q(z)} = \frac{1}{R(z)} - i\frac{2}{kw^2(z)} \tag{A.1.0.5}$$

The complex parameter q usually describes the properties of the gaussian beam at particular point z.

When this gaussian beam which had an initial complex parameter q_i, propagates through an optical system whose Transfer Matrix given by $O = \begin{bmatrix} A & B \\ C & D \end{bmatrix}$, the resulting complex parameter q_f of the gaussian beam can be written as,

$$q_f = \frac{Aq_i + B}{Cq_i + D} \tag{A.1.0.6}$$

A.2 Mode matching

For mode matching the inital gaussian beam to the Fabry Pérot cavity of length l, we use a set of lenses f_1 and f_2 Fabry Pérot cavity as shown in the fig. A.2

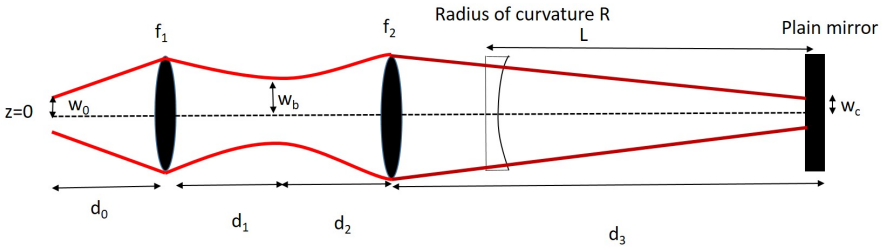

Figure A.2: Optical modematching for Fabry Pérot cavity

The Ray matrix M_1 of a beam traveling a distance d through free space, is given by [46]:

$$M_1 = \begin{bmatrix} 1 & d \\ 0 & 1 \end{bmatrix} \tag{A.2.0.1}$$

The Ray matrix M_2 of a beam travelling through a thin lens of focal length f, is given by [46]:

$$M_2 = \begin{bmatrix} 1 & 0 \\ -\frac{1}{f} & 1 \end{bmatrix} \tag{A.2.0.2}$$

The complex parameter q can be defined as [46]:

$$\frac{1}{q} = \frac{1}{R(z)} - \frac{i\lambda_0}{\pi w^2(z)} \tag{A.2.0.3}$$

In this section we develop the calculations for the modematching of the intial gaussian beam to the fabry Pérot cavity, using equations (A.2.0.1) and (A.2.0.2)

Let A, B and C be the transfer matrices of the Gaussian beam after passing through lens f_1 in fig. A.2 and till the waist w_b are given by

$$A = \begin{bmatrix} 1 & d_0 \\ 0 & 1 \end{bmatrix}$$
$$B = \begin{bmatrix} 1 & 0 \\ -\frac{1}{f_1} & 1 \end{bmatrix}$$
$$C = \begin{bmatrix} 1 & d_1 \\ 0 & 1 \end{bmatrix}$$

The net transfer matrix is hence $O_1 = ABC$ given by,

$$O_1 = \begin{bmatrix} 1 - \frac{d_1}{f_1} & d_1 + d_0(1 - \frac{d_1}{f_1}) \\ -\frac{1}{f_1} & 1 - \frac{d_0}{f_1} \end{bmatrix} \tag{A.2.0.4}$$

While at the initial waist w_0, $R(z) = \infty$. Hence we can write ,

$$\begin{aligned} \frac{1}{q_0} &= \frac{1}{R(z)} - \frac{\lambda i}{\pi w_0^2} \\ q_0 &= \frac{i\pi w_0^2}{\lambda} \end{aligned} \tag{A.2.0.5}$$

The subsequent parameter q_1 after passing through the lens f_1 and distance d_1 until the waist w_b, using equation (A.1.0.6) can be written as,

$$q_1 = \frac{a_1 q_0 + b_1}{c_1 q_0 + d_1} \tag{A.2.0.6}$$

a_1, b_1, c_1, d_1 being the elements of matrix O_1.

Also according to equation (A.2.0.5), q_1 can be written as $q_1 = \frac{i\pi w_b^2}{\lambda}$, since after the lens the gaussian beam has a waist w_b.

Similarly the transfer matrices after passing through lens f_2 and through distance d_2 and d_3 are given by,

$$A_2 = \begin{bmatrix} 1 & d_3 \\ 0 & 1 \end{bmatrix}$$
$$B = \begin{bmatrix} 1 & 0 \\ -\frac{1}{f_2} & 1 \end{bmatrix}$$
$$C = \begin{bmatrix} 1 & d_2 \\ 0 & 1 \end{bmatrix}$$

The equivalent transfer matrix $O_2 = A_2 B_2 C_2$ is given by:

$$O_2 = \begin{bmatrix} 1 - \frac{d_3}{f_2} & d_3 + d_2(1 - \frac{d_3}{f_2}) \\ -\frac{1}{f_2} & 1 - \frac{d_2}{f_2} \end{bmatrix} \tag{A.2.0.7}$$

Similarly, the complex parameter q_2 after passing through the lens f_2 using equation (A.1.0.6) is given by,

$$q_2 = \frac{a_2 q_1 + b_2}{c_2 q_1 + d_2} \tag{A.2.0.8}$$

where a_2, b_2 , c_2 and d_2 are the elements of matrix O_2.

Similarly, with reference to equation (A.2.0.5), $q_2 = \frac{i\pi w_c^2}{\lambda}$,since the waist of the cavity w_c at the end mirror .

Hence using all the above equations, we can solve for the parameters d_1, d_2, d_3, w_b and w_c as:

$$d_1 = \frac{f_1\pi^2 w_0^4 + d_0^2\lambda^2 - d_0 f_1\lambda^2}{(f_1\pi^2 w_0^4 + d_0^2\lambda^2 - 2d_0 f_1\lambda^2 + f_1^2\lambda^2)^{1/2}} \tag{A.2.0.9}$$

$$w_b = \frac{f_1 w_0\lambda}{(f_1\pi^2 w_0^4 + d_0^2\lambda^2 - 2d_0 f_1\lambda^2 + f_1^2\lambda^2)^{1/2}} \tag{A.2.0.10}$$

$$d_2 = f_2 + (\frac{f_2^2 w_b^2\lambda^2}{w_c^2} - \pi^2 w_b^4)^{1/2}\lambda \tag{A.2.0.11}$$

$$d_3 = \frac{f_2\pi^2 w_b^4 + d_2^2\lambda^2 - d_2 f_2\lambda^2}{(f_2\pi^2 w_b^4 + d_2^2\lambda^2 - 2d_2 f_2\lambda^2 + f_2^2\lambda^2)^{1/2}} \tag{A.2.0.12}$$

$$w_c = \frac{f_2 w_b\lambda}{(f_2\pi^2 w_b^4 + d_2^2\lambda^2 - 2d_2 f_2\lambda^2 + f_2^2\lambda^2)^{1/2}} \tag{A.2.0.13}$$

APPENDIX B

TRANSFER FUNCIONS AND OPEN LOOP

B.1 Introduction

For designing the PI lockboxes and to characterize the feedback loop of the lock, it is necessary to measure the closed loop transfer function and open loop transfer function of the system. In this Appendix, I will give a complete description of how the lockboxes are designed based on measurement of closed loop transfer function. We will also evaluate the unity gain frequency from the measured open loop transfer function.

B.1.1 Transfer function and Open loop

In a control system, the ratio of its output to input in the Laplace domain is called Transfer function [64]. If we have an input property $x_{in}(s)$ and an output property $x_{out}(s)$ as in fig. B.1, then the transfer function T is given as,

Figure B.1: Transfer Function with $x_{in}(s)$ as input $x_{out}(s)$ as output. T is considered as Transfer function.

$$T(s) = x_{out}(s)/x_{in}(s) \tag{B.1.1.1}$$

Let us consider a closed loop control system in fig. B.2

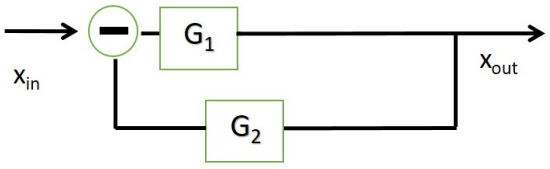

Figure B.2: Closed loop system with x_{in} as input x_{out} as output.

Then we can write x_{out} as,

$$x_{out} = x_{in}G_1 - G_1G_2x_{out} \tag{B.1.1.2}$$

Then the effective transfer function H_{eff},

$$H_{eff} = \frac{x_{out}}{x_{in}} = \frac{G_1}{1 + G_1G_2} \tag{B.1.1.3}$$

The term G_1G_2 is called open loop transfer function. The system becomes unstable if the open loop transfer function $G_0(s) = G_1(s)G_2(s) = -1$. In general,Bode plots are used to assess the stability of a control system.

Measurement in our system

To estimate the unity gain frequency of the system, it is necessary to perform an open loop measurement and perform the gain-phase analysis. The unity gain frequency is defined as the frequency at which magnitude of gain, $|H_{eff}(j\omega)| = 1(0dB)$. Since the unity gain frequency is related to the bandwidth of the lock, it is better to have a higher unity gain frequency, for compensation of the fluctuations. However, the system becomes unstable if there is a resonance at the unity gain frequency. Hence the design of the lockboxes should be done such that there is enough gain towards the lower frequencies for compensating weak disturbances whilst keeping the resonances at higher frequencies at low gain.

The open loop measurement can in theory be just be performed by removing the feedback loop in fig. B.2. However in practice we can obtain it by probing the system through a Network analyzer at all frequencies and measuring transmission and reflection (T/R) response.

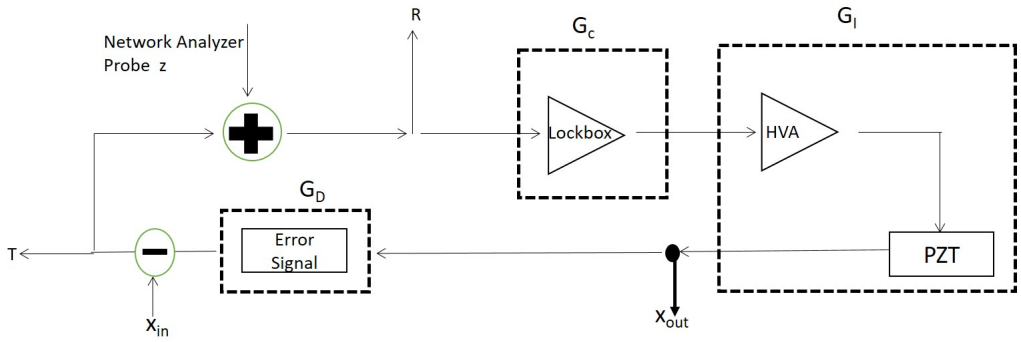

Figure B.3: Open loop measurement scheme for our interferometer system.

Let G_L represents transfer function of lock-box (PI controller), G_I represents transfer function of interferometer (including High voltage Amplifier (HVA) and PZTs of the end mirrors), and G_D represent the transfer function of photodetector. The open loop transfer function of the system is $G_0 = G_LG_IG_D$. The parameters x_t and x_r at probes T and R can be written as

$$x_t = x_{in} - zG_0 - x_{out}G_D \tag{B.1.1.4}$$

$$x_r = x_{in} - x_{out}G_D + z \tag{B.1.1.5}$$

If we remove the probes T and R of the Network analyzer and solve for x_{out} and x_{in},

$$x_{out} = (x_{in} + z)\frac{G_L G_I}{1 + G_0} \tag{B.1.1.6}$$

Subtracting equation B.1.1.4 from equation B.1.1.5 we get the information about the open loop funtion G_0.

$$X = x_t - x_r = z(1 + G_0) \tag{B.1.1.7}$$

It is to be noted that the space of our algebra is in Laplace space. However the network analyzer only has the function of providing the ratio T/R and it performs Gain-Phase analysis on a Bode plot which is in frequency domain. This is not a problem as the multiplicative amplitudes are additive in log scale [64],[65] and would yield the same result of singling out G_0.

The fig. B.4 shows us how to evaluate the transfer function. This kind of circuit helps in singling out the transfer function of $G_I G_D$. The system needs to be locked while the network analyzer probes the system at all frequencies.

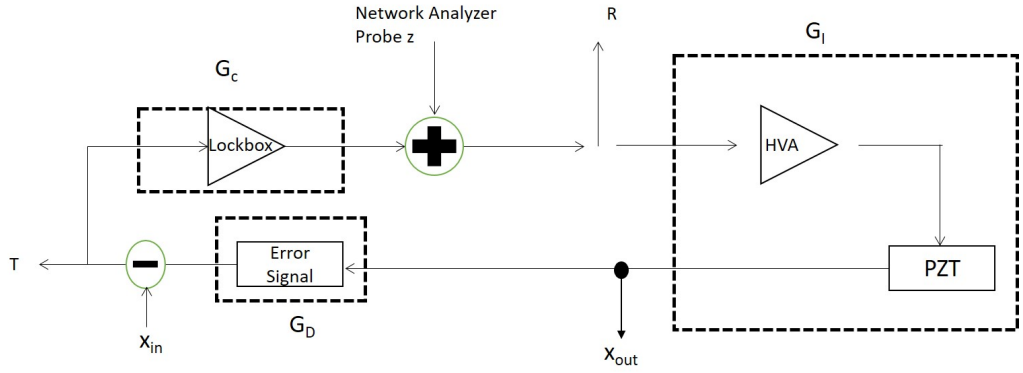

Figure B.4: The figure represents open loop measurement scheme for our interferometer system.

Let us analyze the full circuit without the probes of T and R. Hence we can write:

$$x_{out} = \frac{(x_{in}G_L + z)G_I G_D}{1 + G_I G_D} \tag{B.1.1.8}$$

The equation (B.1.1.8) shows that we can single out the closed loop transfer function of $G_I G_D$. Hence when we probe the system at T and R ,the parameters x_t and x_r can be written as:

$$\begin{aligned} x_t &= x_{in} - zG_I G_D - x_{out}G_D \\ x_r &= x_{in}G_L + z - x_{out}G_D G_L \end{aligned} \tag{B.1.1.9}$$

Since the probing only works for a system which is already locked system at fixed bias point, the terms involving x_{in} and x_{out} can be neglected[52]. Thus using equations (B.1.1.8) and

(B.1.1.9) , we can evaluate the $x_t - x_r$ as

$$x_t - x_r = x_{in} - zG_IG_D - x_{out}G_D - (x_{in}G_L + z - x_{out}G_DG_L) \approx z(1+(G_IG_D)) \quad \text{(B.1.1.10)}$$

In the bode plot for gain-phase analysis of the T/R ratio, we expect to yield the same result as in equation (B.1.1.10) where we single out the term G_IG_D.

Characterization of Transfer functions and open loop transfer functions

Bode plots in general are used to assess the stability of a control system in general. Firstly, the frequency response of the closed loop transfer function for both DARM and CARM degree of freedom are evaluated as shown in fig. B.5 with a help of newtwork analyzer. The network analyzer probes the system at all frequencies while the system is locked. The DARM closed loop transfer function is measured by misaligning the power recycling cavity to the michelson interferometer configuration and locking it to a point on the fringe while the network anlyzer probes the PZT actuators of the end mirrors differentially (i.e by a phase of π) at all frequencies. On the other hand, the CARM closed loop transfer function is measured in the power recycling configuration by locking both degrees of freedom (DARM and CARM) while the network anlyzer probes the PZT actuators of the end mirrors with no relative phase lag at all frequencies.

For evaluating the unity gain frequency from the measured transfer function, a simulation was done by placing approximate values of the integrators, and low pass filters of the PI controller on the measured transfer function. The values of the proportionality, integrators are put in the simulation such that there is enough gain towards the lower frequencies for compensating weak disturbances whilst keeping the resonances at higher frequencies at low gain (since an instability occurs when resonance exceeds 0dB) as discussed in section B.1.1. The fig. B.6 shows the simulation on the evaluated transfer function. Also in the phase measurement, the phase should not be less than -135^0 as some op-amps used in the PI controller can get unstable.

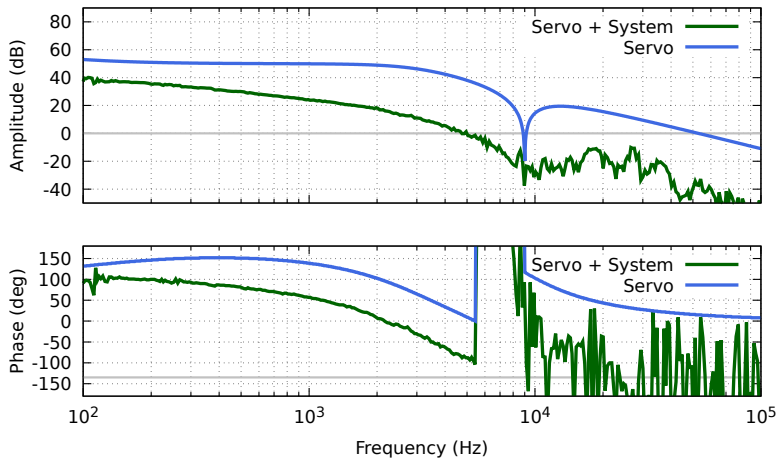

Figure B.6: Simulation on the measured transfer function. The servo was designed with intergrator frequency 1.6 KHz and propotionality factor of 60dB. The expected unity gain frequency was about 3kHz.

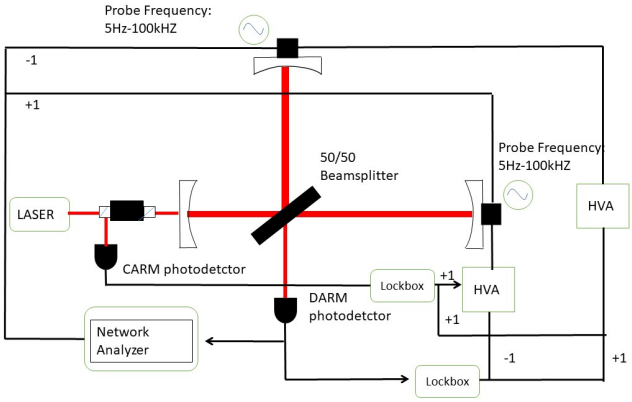

(i) Transfer function for Differential Arm

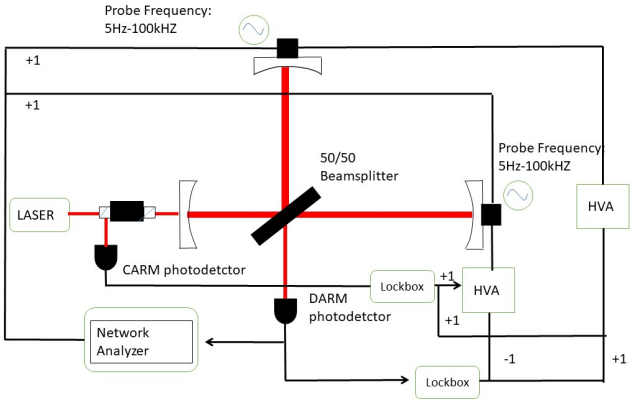

(ii) Transfer function for Common Arm

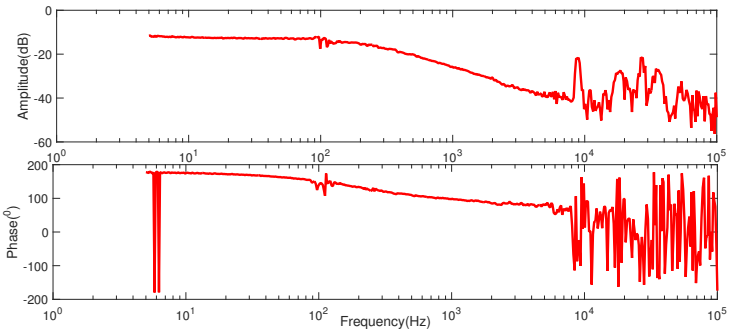

(iii) Transfer function for Differential Arm

Figure B.5: The network analyzer probes the PZTs at different frequencies from 5 Hz-100 kHz and T/R ratio is evaluated while the system is locked. (i) When charecterizing the DARM response, the Network analyzer is probed differentially. (ii) When Characterizing the CARM response, the newtwork analyzer is probde equally. (iii) The evaluated transfer function for Differential arm of the interferometer

It is to be noted however that, the unity gain frequency obtained from the simulation gives only an approximate estimation. The real estimation of the unity gain frequency is obtained by measuring the open loop function of the system with the newly designed servo for both DARM and CARM as depicted in fig. B.3. There is a discrepancy of the value in

the unity gain frequency, between the one estimated from the simulation and the obtained value. This is because for eliminating or shifting the resonances to higher frequencies, the mechanics was further improved after the measurement of transfer function. This was done by clamping the end mirrors with a metallic base and adjusting the torque on the screws of the metallic base, and this might have changed the measured transfer function. The fig. B.7 plots the open loop transfer function as a function of frequency. The unity gain frequency obtained for our system is around 1.3 kHz.

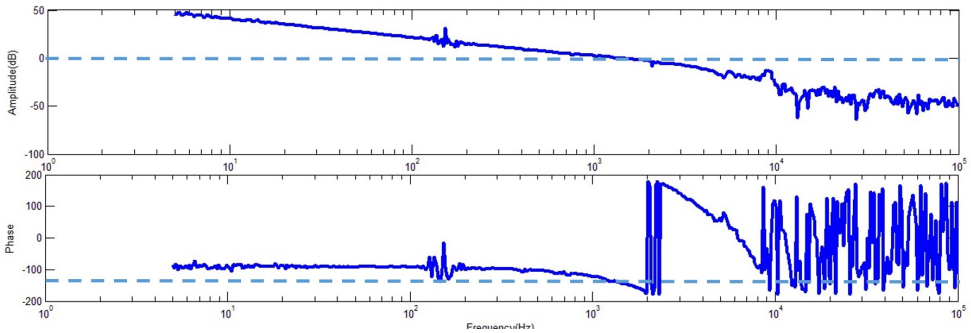

(i) Open loop DARM

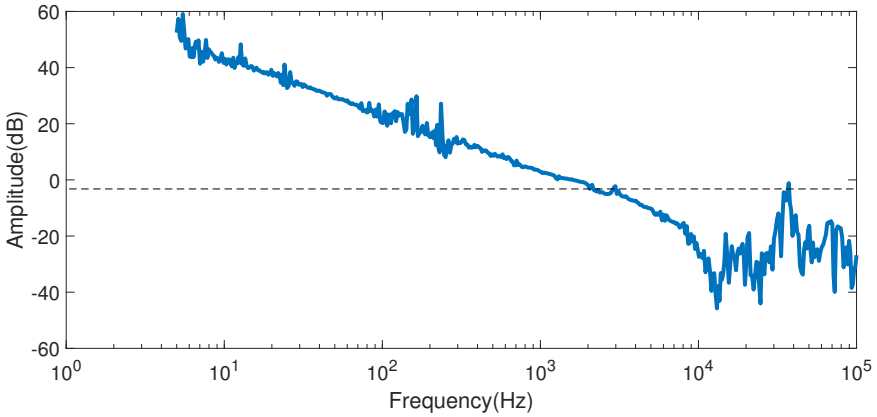

(ii) Open loop CARM

Figure B.7: (i) Open loop measurement for the DARM, (ii)Open loop measuremenmt fopr CARM. The unity gain frequency obtained was around 1.3 kHz

APPENDIX C

ELECTRONICS

C.1 Electronics schematic of the PI controller

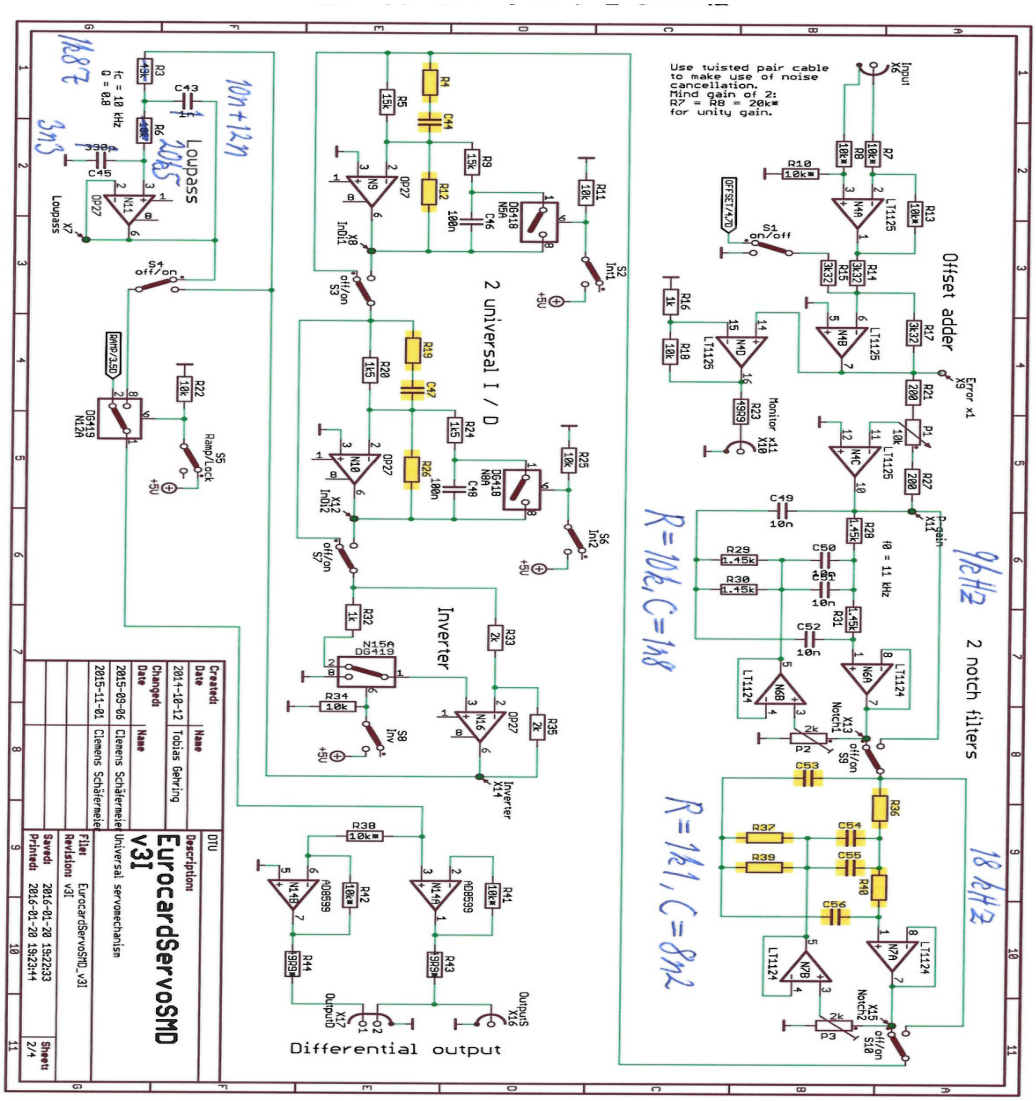

C.2 Electronic schematic of photodetector

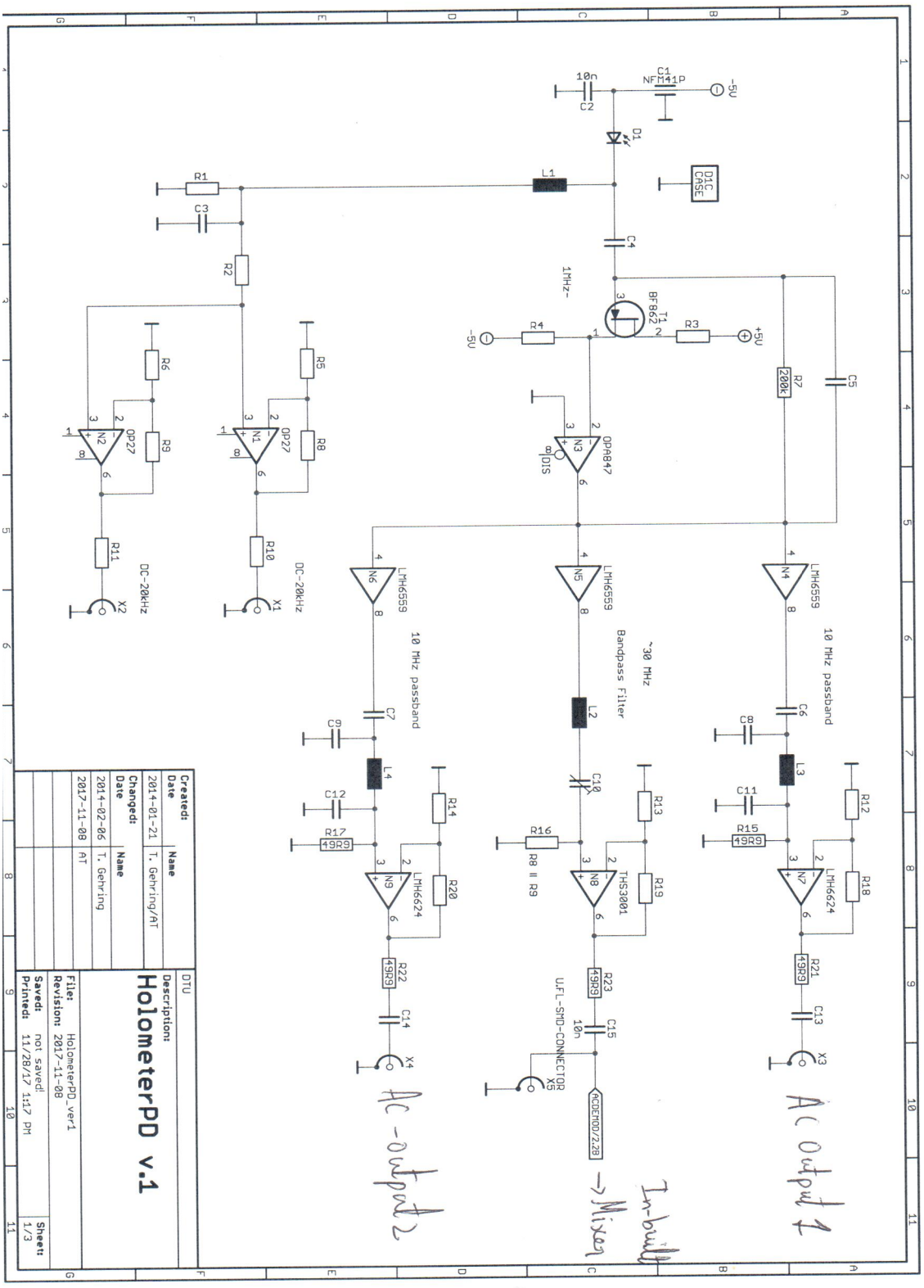

Figure 1: *Project schematics (sheet 1)*

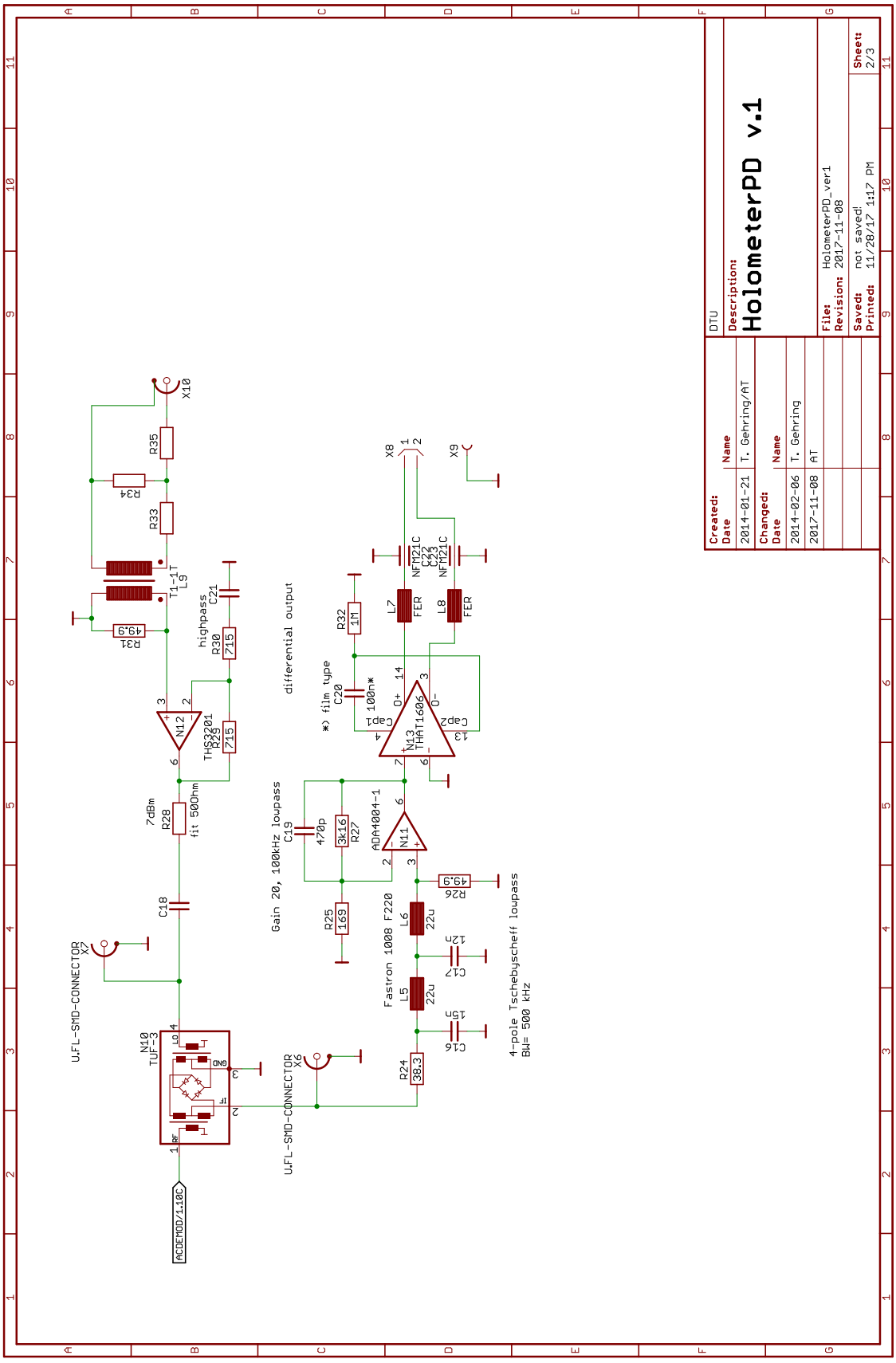

Figure 2: *Project schematics (sheet 2)*

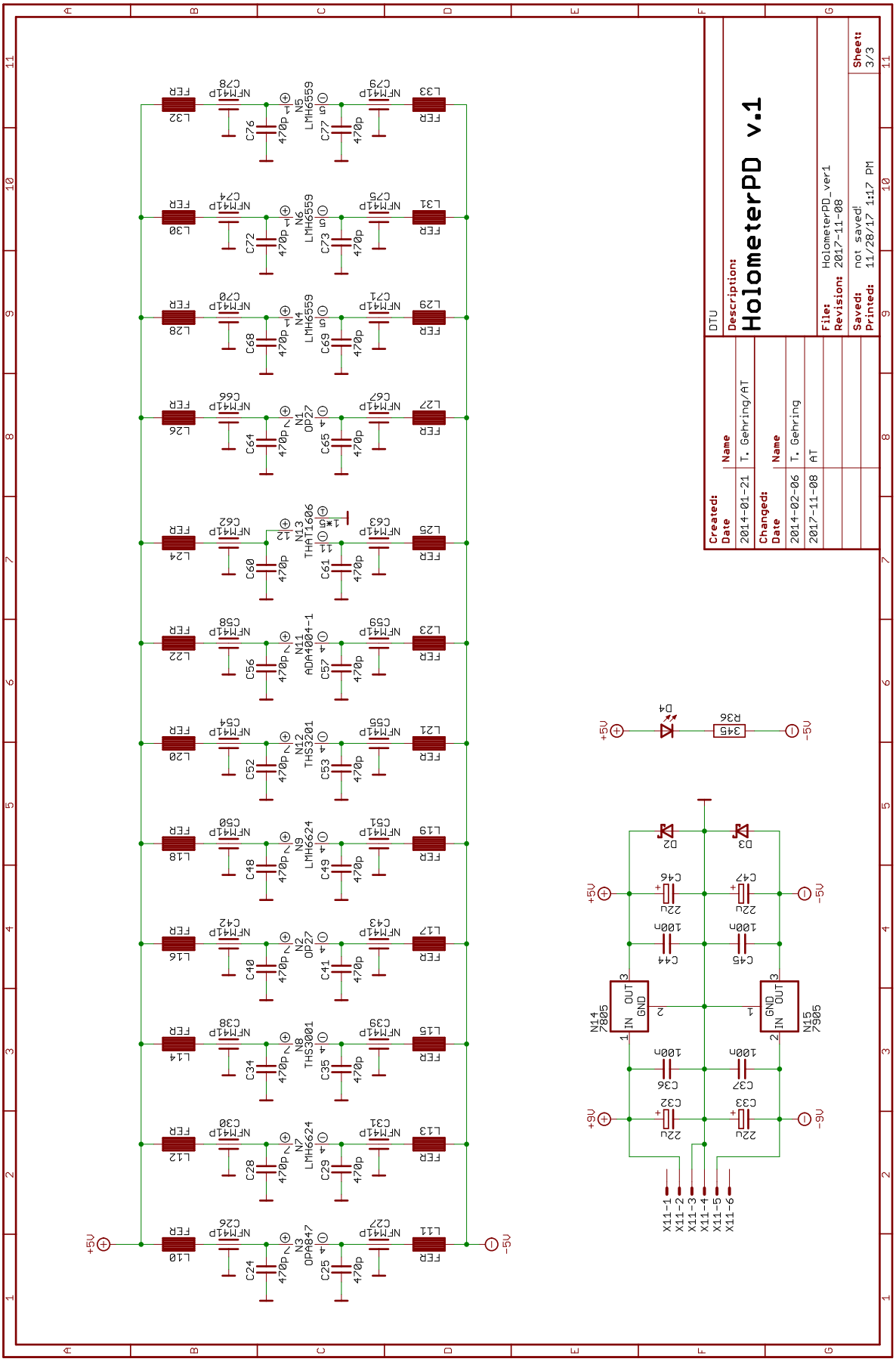

Figure 3: *Project schematics (sheet 3)*

APPENDIX D

PSD EVALUATION

D.1 Evaluation of PSD

Most of this section describing the evaluation of the power spectral density is taken from [62]. The power spectral density is obtained by using Welch's method. Let us consider f_S to be the sampling frequency and N as the length of the sample. The frequency resolution is given by $f_{res} = \frac{f_S}{N}$. Before evaluating, the PSD we need to apply the basics of the discrete Fourier transform (DFT). For N discrete time variables x_n the discrete Fourier transform gives vector of length N of y_m where $m = 0, 1, ...N-1$. Hence the DFT of each y_m is given by,

$$y_m = \frac{\sum_{n=0}^{N-1} x_n e^{(-2\pi i \frac{mn}{N})}}{N}, \;\; m = 0, ...N-1 \tag{D.1.0.1}$$

The frequencies f_m corresponding to y_m is given by $f_m = m\frac{f_s}{2}$. However if we use the equation (D.1.0.1) in case of finite length data, leads to the presence of artifacts in the frequency spectrum, which is not a faithful representation of the physical signal [66]. A window function in general is used to reduce this effects that occurs in an DFT of data. There are many window functions such as Hanning, Hamming, Flat top etc. that are used for evaluating the DFT. For most of the cases, Hanning window $w_j = \frac{1}{2}[1 - \cos(\frac{2\pi j}{N})]$ is applied while for more accurate measurements we need to use specialized window functions.

$$y_m = \frac{\sum_{n=0}^{N-1} w_n x_n e^{(-2\pi i \frac{mn}{N})}}{S_1}, \;\; m = 0, ...N-1 \tag{D.1.0.2}$$

where $S_1 = \sum_{n=0}^{N-1} w_n$ The power spectrum is given by[54]

$$PS_{rms} = \frac{2|y_m|^2}{S_1^2} \tag{D.1.0.3}$$

and the power spectral density is then defined as the ratio of power spectrum to effective noise band width (ENBW)[52]. The ENBW is given by $ENBW = \frac{f_s S_2}{S_1^2}$. Hence the PSD is given by,

$$PSD = \frac{2|y_m|^2}{S_2 f_S} \tag{D.1.0.4}$$

where $S_2 = sum_{n=0}^{N-1} w_n^2$ Sometimes the above expression in equation (D.1.0.4) is called a periodogram which correponds to computation of only one estimate. If we compute only for one estimate, practically the spectra obtained will be noisy. Hence we need to average upon $N_{spectra}$ estimates to reduce the standard deviation of the spectra by $\frac{1}{\sqrt{N_{spectra}}}$. Hence it requires to split the time series into several parts and slightly overlap the segments. Then we evaluate the power spectral density for each segment as in equation (D.1.0.4) and perform the average of the obtained power spectral density over all the $N_{spectra}$ parts. Usually the overlap percentage depends on the type of window we would like to use. For example, Hanning window the optimal overlap percentage is taken to be 50%.

More detailed information for computing the PSD of a time-series using Matlab function "pwelch" is given in [62],[67].

D.2 Cross Power Spectral Density

As discussed in section 5.5, the cross power spectral density is evaluated as in equation (5.5.0.1) using Welch's method. Initially the DC offset is removed for each timeseries by subtracting the timeseries with its mean value. In analogy with the DFT estimation, CPSD periodogram with window functions w_j is

$$S_{12}(m) = \frac{1}{S_2 f_S} \sum_j w_j R_{12}(j) e^{-2\pi i \frac{mj}{N}} \tag{D.2.0.1}$$

where $R_{12}(j) = \langle x_1(j) x_2^*(j+m) \rangle$. with respective frequencies $f_m = \frac{m f_s}{2}$ As discussed in analogy with the evaluation of PSD, window functions such as hanning, Flat top windows are applied. However the equation (D.2.0.1) evaluates only for one estimate. which will have a noisy spectra. Hence Welch's method is used to scale down this noisy spectra. In the Welch's method, similar to the evaluation of the PSD, each of the time series are divided into $N_{spectra}$ bins, the CPSD is evaluated for each bin and average of $N_{spectra}$ bins are evaluated so that the uncorrelated noise scales as $1/\sqrt{N_{spectra}}$. However unlike in the power spectral density evaluation there is no overlap taken between the several segments, additional correlations would be added due to overlapping, which would give us an error in the estimate of the CPSD. The estimation of CPSD was implemented by using a labview program.

LIST OF FIGURES

LIST OF TABLES

REFERENCES

[1] J.P.Dowling and G.J.Milburn. Quantum Technology: The Second Quantum Revolution. *Phil. Trans. R. Soc. A*, 361, 3655, 2003.

[2] Schleich, W.P., Ranade, K.S., Anton, C. et al. . Quantum technology: from research to application. *Appl. Phys. B.*, 122: 130., 2016.

[3] Nicolas Gisin Rob Thew. Quantum communication. *Nature Photonics*, 1:165171, 2007.

[4] Mohsen Razavi, Anthony Leverrier, Xiongfeng Ma, Bing Qi, and Zhiliang Yuan. Quantum key distribution and beyond: introduction. *J. Opt. Soc. Am. B*, 36,, 2019.

[5] Taylor Micheal A. and Bowen Warwick P. Quantum Metrology and its application in biology. *Physical Reports*, 615:1–59, 2016.

[6] Vittorio Giovannetti, Seth Lloyd, and Lorenzo Maccone. Advances in quantum metrology. *Nature Photonics*, 5(4):222–229, 2011.

[7] Jonathan P. Dowling and Kaushik P. Seshadreesan. Quantum Optical Technologies for Metrology, Sensing, and Imaging. *J. Lightwave Technol.*, 33, 2359-2370, 2015.

[8] T. D. Ladd, F. Jelezko, R. Laflamme, Y. Nakamura, C. Monroe J. L. OBrien. Quantum computers. *Nature*, 464:4553, 2003.

[9] Andrew Steane. Quantum computing. *Rep. Prog. Phys.*, 61,pp:117, 1998.

[10] G.Brida, Marco Genovese, and I.Ruo-Berchera. Experimental realization of subshot noise quantum imaging. *Nature Photonics*, 44(4):227–230, 2010.

[11] Marco Genovese. Real applications of quantum imaging. *Journal of Optics*, 18(7):073002, 2016.

[12] Vittorio Giovannetti, Seth Lloyd and Lorenzo Maccone. Quantum enhanced measurement: Beating the Standard Quantum Limit. *Science*, 306:1330–1336, 2004.

[13] Craig J. Hogan, O. Kwon. Statistical models of exotic rotioanal correlations in emergent space-time. *Class and Q.Grav*, 34(13):135006, 2017.

[14] Florian Wolfgramm, Alessandro Cer, Federica A. Beduini, Ana Predojevi, Marco Koschorreck, and Morgan W. Mitchell. Squeezed-Light Optical Magnetometry. *PRL*, 105, 053601, 2010.

[15] Michael A. Taylor, Jiri Janousek, Vincent Daria, Joachim Knittel, Boris Hage, Hans-A. Bachor Warwick P. Bowen. Biological measurement beyond the quantum limit. *Nature Photonics*, 7, pages 229233, 2013.

[16] Bahaa E. A. Saleh, Bradley M. Jost, Hong-Bing Fei, and Malvin C. Teich. Entangled-Photon Virtual-State Spectroscopy. *Phys. Rev. Lett.* , 80, 3483, 1998.

[17] Agedi N. Boto, Pieter Kok, Daniel S. Abrams, Samuel L. Braunstein, Colin P. Williams, and Jonathan P. Dowling. Quantum Interferometric Optical Lithography: Exploiting Entanglement to Beat the Diffraction Limit. *PRL*, 85, 2733, 2000.

[18] G. M. DAriano, M. G. A. Paris and P. Perinotti. Improving quantum interferometry by using entanglement. *PRA*, 65 062106, 2002.

[19] Melanie Meinders Helge Müller-Ebhardt Karsten Danzmann Sebastian Steinlechner, Jöran Bauchrowitz and Roman Schnabel. Quantum-dense metrology. *Nature Photonics*, 7(8):626–629, 2013.

[20] B. P. Abbott et al. Observation of gravitational waves from a binary black hole merger. *Physical Review Letters*, 116(6):061102, 2016.

[21] J. Aasi et al. Enhanced sensitivity of the LIGO gravitational wave detector by using squeezed states of light. *Nature Photonics*, 7(8):613–619, 2013.

[22] Craig J Hogan. Interferometers as probes of Planck in a quantum geometry. *Physical Review D*, 85(6):064007, 2012.

[23] Tomotada Akutsu, Seiji Kawamura, Atsushi Nishizawa, Koji Arai, Kazuhiro Yamamoto, Daisuke Tatsumi, Shigeo Nagano, Erina Nishida, Takeshi Chiba, Ryuichi Takahashi, Naoshi Sugiyama, Mitsuhiro Fukushima, Toshitaka Yamazaki, and Masa Katsu Fujimoto. Search for a stochastic background of 100-MHz gravitational waves with laser interferometers. *Physical Review Letters*, 101(10):101101, 2008.

[24] Joseph D. Romano and Neil J. Cornish. Detection methods for stochastic gravitational-wave backgrounds: A unified treatment. *Living Reviews in Relativity*, 20(2):1–223, 2017.

[25] Craig J. Hogan, O. Kwon. Models of exotic interferometer cross-correlations in emergent space-time. *Class and Q.Grav*, 35(20):204001, 2018.

[26] Aaron S.Chou, Henry Glass, H. Richard Gustafson, Craig J.Hogan, Brittany L.Kamai, Ohkyung Kwon, Robert Lanza, Lee McCuller, Stephan S. Meyer, Johnathan

W.Richardson, Chris Stoughton, Ray Tomlin and Rainer Weiss. MHz gravitational wave constraints with Decameter Michelson interferometers. *Physical Review D*, 95(6):063002, 2017.

[27] Aaron S.Chou, Henry Glass, H. Richard Gustafson, Craig J.Hogan, Brittany L.Kamai, Ohkyung Kwon, Robert Lanza, Lee McCuller, Stephan S. Meyer, Johnathan W.Richardson, Chris Stoughton, Ray Tomlin and Rainer Weiss. First Measurements of High Frequency Cross Spectra from a pair of Large Michelson Interferometers. *Physical Review letters*, 117(11):1111102, 2016.

[28] Ivano Ruo berchera, I.P. Degiovanni, Stefano Olivares, N. Samantaray, P.Traina and Marco Genovese. One and two mode squeezed light in correlated interferometery. *Physical Review A*, 92(5):053821, 2015.

[29] Ivano Ruo-Berchera, I.P. Degiovanni, Stefano Olivares and Marco Genovese. Quantum light in coupled interferometers for quantum gravity tests. *Physical Review letters*, 110(21):213601, 2013.

[30] Girish S. Agarwal. *Quantum Optics, An Introduction.* Cambridge University Press, 2012.

[31] J.J.Sakurai. *Modern Quantum Mechanics.* Pearson, 1994.

[32] Mark S. Fox. *Quantum Optics.* Oxford University Press, 2006.

[33] S. Goldstein, Arthur Fine, James T. Cushing. *Bohmian Mechanics and Quantum Theory: An Appraisal.* ISBN:978-90-481-4698-7, 1996.

[34] G. Breitenbach, S. Schiller & J. Mlynek. Measurement of the quantum states of squeezed light. *Nature.*, 387, pages471475, 1997.

[35] A.Lvovsky. *Photonics Volume 1: Fundamentals of Photonics and Physics.* Wiley, 2015.

[36] J. Abadie et al. A gravitational wave observatory operating beyond the quantum shot-noise limit. *Nature Physics*, 7(12):962–965, 2011.

[37] Carlton Caves. Quantum-mechanical noise in an interferometer. *Physical Review D*, 523(8):1693–1708, 1981.

[38] Kirk Mckenzie, Daniel A. Shaddock, David E. McCleland, Ben C Bucher and Ping Koy Lam. Experimental Demonstration of a Squeezing Enhanced Power Recycled Interferometer. *Physical Review letters*, 88(23):231102, 2002.

[39] K. Goda, O. Miyakawa, E. E. Mikhailov, S. Saraf, R. Adhikari, K. McKenzie, R. Ward, S. Vass, A. J. Weinstein & N. Mavalvala. A quantum-enhanced prototype gravitational-wave detector. *Nature Physics*, 4:472476, 2008.

[40] H. Grote, K. Danzmann, K.L. Dooley, R. Schnabel, J. Slutsky, H. Vahlbruch. First Long-Term Application of Squeezed States of Light in a Gravitational-Wave Observatory. *PRL*, 110, 181101, 2013.

[41] Aasi, J. et al. Advanced LIGO. *Class.Quant.Grav*, 32:074001, 2015.

[42] Aaron S. Chou, Henry Glass, H. Richard Gustafson, Craig J. Hogan, Brittany L. Kamai, Ohkyung Kwon, Robert Lanza, Lee McCuller, Stephan S. Meyer, Jonathan W. Richardson, Chris Stoughton, Ray Tomlin, and Rainer Weiss. Interferometric constraints on quantum geometrical shear noise correlations. *Classical and Quantum Gravity*, 34:165005, 2017.

[43] B. P. Abbott et al. Interferometer techniques for gravitational-wave detection. *Living Rev Relativ.*, 19: 3, 2016.

[44] Frank L. Pedrotti, Leno M. Pedrotti, Leno S. Pedrotti. *Introduction to Optics*. Addison-Wesley, 2006.

[45] Eric D. Black. Notes on the Pound-Drever-Hall technique. 1998.

[46] A. E. Siegman. *Lasers*. Univ Science Books, 1986.

[47] Tobin Thomas Fricke. *Homodyne Detection for Laser-Interferometers*. PhD thesis, Louisiana State University and Agricultural and Mechanical College, 1993.

[48] Bond, C., Brown, D., Freise, A. et al. . Interferometer techniques for gravitational-wave detection. *Living Rev Relativ.*, 19:3, 2016.

[49] L. Schnupp. Presentation at European Collaboration Meeting on Interferometric Detection of Gravitational Waves. *Sorrent*, 1988.

[50] Buonanno A et al. Quantum noise in laser-interferometer gravitational-wave detectors with a heterodyne readout scheme. *Physical Review D* , 67, 2003.

[51] Freise, A. & Strain, K. Interferometer techniques for gravitational-wave detection. *Living Rev Relativ.*, 19: 3, 2016.

[52] Freise A. FINESSE-Frequency Domain Interferometer Simulation Software. *arxiv:1306.02973*, 2013.

[53] G. Heinzel, A. Rudiger, R. Schilling, K. Strain, W. Winkler, J. Mizuno, K. Danzmann. Automatic beam alignment in the Garching 30-m prototype of a laser-interferometric gravitational wave detector. *Opt. Comm. 1999*, 109, 1999.

[54] Ulrik L Andersen et al. 30 years of squeezed light generation. *Phys. Scr.*, 91 053001, 2016.

[55] Roman Schnabel. Squeezed states of light and their applications in Laser interferometers. *Phys. Scr.*, 684:2–51, 2017.

[56] Karsten Rottwitt & Peter Tidemand-Lichtenberg. *Non Linear Optics.* CRC Press, 2015.

[57] C.Gardiner and C.Savage. A multimode quantum theory of degenerate parameteric amplifier in a cavity. *Optics Communication*, 50.3, 1984.

[58] Eiichi Hanamura, Yutaka Kawabe, Akio Yamanaka . *Quantum Nonlinear Optics.* Springer, 2007.

[59] Julius O.Smith III. *Mathematics of Discrete Fourier Transform.* W3K, 2007.

[60] R.P.Khare. *Fiber Optics and Optoelectronics.* Oxford university Press, 2004.

[61] A.Hamel and M.R. Mathieu. Demonstration of a 140-Mbit/s Transmission by Coherence Modulation at $1.3\mu m$ with a $LiNbO_3$ Integrated Optic Modulator. *Coherent Fiber optics System*, 1994.

[62] G. Heinzel, A. Rudiger and R. Schilling. Spectrum and spectral density estimation by the Discrete Fourier transform (DFT), including a comprehensive list of window functions and some new at-top windows. 2002.

[63] B. J. Carr and S. W. Hawking. Black Holes in the early universe. *Mon. Not. R. astr. Soc.*, 168:399–415, 1974.

[64] I.J Nagrath. *Control Systems Engineering.* New age international(P) limited, 2005.

[65] Schfermeier, C., Andersen, U. L., & Huck, A. Department of Physics. *Quantum enhanced optical sensing.* PhD thesis, Technical University of Denmark., 2016.

[66] Emmanuel C. Ifeachor, Barrie W. Jervis . *Digital Signal Processing: A Practical Approach.* Addison-Wesley, 1993.

[67] Kwonhue Choi and HuaPing Liu. *Problem-Based Learning in Communication systems Using MATLAB and Simulink* . IEEE Press, 2016.